Università degli Studi di Parma
Facoltà di Ingegneria

Dottorato di Ricerca in Ingegneria Civile
(XX Ciclo)

Chiara Ziveri

2D Finite Volume Numerical Modeling of Free Surface Flows with Topography

Dissertazione per il conseguimento del titolo di Dottore di Ricerca

Tutore: Prof. Paolo Mignosa
Coordinatore del Dottorato: Prof. Paolo Mignosa

Parma, Febbraio 2008

Il viaggio non finisce mai [...]. Quando il viaggiatore si è seduto sulla sabbia della spiaggia e ha detto: "Non c'è altro da vedere", sapeva che non era vero. Bisogna vedere quel che non si è visto, vedere di nuovo quel che si è già visto [...]. Bisogna tornare sui passi già dati, per riperterli, e per tracciarvi a fianco nuovi cammini. Bisogna ricominciare il viaggio. Sempre.

J. Saramago

Contents

List of Figures

List of Tables

Acknowledgments

Desidero ringraziare innanzitutto il Prof. Mignosa che con la conoscenza, l'impegno e la serietà è stato per me una vera guida in questi anni. Grazie ad Andrea per essermi stato sempre vicino con la sua preparazione e le sue sagge parole e a Francesca per la viva partecipazione, la complicità e l'aiuto mai negato. Grazie alla Prof.ssa Tanda e al Prof. Longo per la disponibilità e la gentilezza; grazie ad Andrea, Luca, Marco e Renato per i preziosi aiuti e le risate altrettanto indispensabili. Un ringraziamento grande va alla mia famiglia che mi ha sempre sostenuto e dato fiducia. E infine grazie a Michele che come non mai mi è stato vicino in questi anni e che crede in me nonostante tutto.

Chapter 1

Introduction

Nowadays numerical methods are a widespread tool for studying physical problems that can be mathematically modeled by a set of partial differential equations. When no analytical solutions are available and the experimental approach is too expansive or simply not able to reproduce real conditions, numerical methods are the alternative.
Among several multi-disciplinary applications, in hydraulic engineering numerical modeling is frequently adopted by river basin management for the hazard risk assessment and the development of emergency plans in the case of catastrophic events, like river inundations, levee failures or dam-breaks. Due to the huge impact that these events can have on the environment and, above all, on human lives, planning ahead is an activity of great importance.
Many unsteady free surface flows under gravity, such as those mentioned above, can be described by the shallow water model. Shallow water equations (SWE) are a time-dependent two-dimensional system of partial differential equation of hyperbolic type, which derive from the conservation laws of mass and momentum with the assumption of a vertical scale much smaller that the horizontal one. Because the non-linearity of SWEs, their solution admits discontinuities (shocks), even though the initial data are smooth. In order to propagate a shock at the correct speed, conservative methods must be used. Conservative methods cannot be developed if the governing equations are not written in conservative form, which derives directly from the integral form of conservation laws without any assumption of smoothness of the solution. In their fundamental work, Lax and Wendroff [42] mathematically proved that conservative numerical methods, if convergent, do converge to the weak solution of the conservation laws.

We are interested in studying shock-capturing methods, which must capture the discontinuities automatically, without explicitly tracking them. In other words, the scheme needs to implicitly incorporate the correct jump condition, reduce smearing to a minimum and not to introduce spurious oscillations near discontinuities.
In order to circumvent the limitation imposed by Godunov's theorem [27], according to which spurious oscillations near shocks are unavoidable if linear methods are adopted, non-linear schemes can be implemented. A successful class of non-linear second-order shock-capturing schemes is represented by TVD high-resolution methods [29], which are a modern version of the original Godunov method. These models are oscillations free near shock waves and retain high-order of accuracy in smooth part of the flow. Based on TVD reconstruction, the Monotone Upstream Scheme for Conservation Laws (MUSCL) proposed by Van Leer [75] achieves second-order of accuracy performing a piece-wise interpolation. Following this idea different MUSCL-type schemes were proposed, for example the MUSCL-Hancock method [79] or the SLIC scheme [68].
Schemes of higher order of accuracy are beginning to see their way through applications to shallow water flow. The Essentially Non-Oscillatory (ENO) and Weighted Essentially Non-Oscillatory (WENO) [32, 59, 46] allows the construction of numerical schemes for hyperbolic equations of accuracy greater than two. The ADER approach [70], which is based on the solution of the Derivative Riemann Problem [72], also allows the construction of methods of arbitrary order of accuracy.
The solution of the Riemann problem can be utilized also by other schemes, as for example Discontinuos Galerkin Finite Element methods [21] and SPH (Smooth Particle Hydrodynamics) methods [51].
There has been much research into the efficient solution of homogeneous system of conservation laws and the main focus has been put on the accurate representation of discontinuities. However, the implementation of numerical methods when source terms are relevant is not straightforward and the applications of these schemes to river flow and complex geometries is not so common in the literature. The presence of extreme slopes, high roughness and strong changes in the irregular geometry represents a great difficulty which can lead to appreciable numerical errors, presumably arising from source terms of the equations. Bed slope and friction source terms are of special relevance in hydraulic applications based on shallow water model; one of the fundamental aspect in the source term discretization is the correct balance between fluxes and source terms near steady state solution.
Another challenge connected with the application of Godunov-type methods to

field-scale problems is the occurrence of dry regions somewhere in the domain. One of the main numerical difficulty is connected with the computation of particle velocity from the ratio of updated values for the momentum and the water depth, with this one very small near fronts. The typical behavior of the computed wet/dry fronts is characterized by unphysical oscillations, more visible in the velocities results, and positional error of the front that grows as a function of time, potentially leading to erroneous predictions for arrival times in dam-break simulations.

With these goals in mind, a finite-volume MUSCL-type scheme for the numerical solution of inhomogeneous SWE is here presented.
The novel aspect is data reconstruction: the scheme, named WSDGM (*Weighted Surface-Depth Gradient Method*), computes intercell water depths performing a weighted average of DGM and SGM reconstructions [82], in which the weight function depends on the local Froude number. This combination makes WSDGM capable of performing a robust tracking of wet/dry fronts and, together with an unsplit centered discretization of the bed slope source term, of exactly maintaining the static condition on non-flat topographies (*C-property*) [14]. Moreover, a numerical procedure performing a correction of the numerical fluxes in the computational cells with water depth smaller than a fixed tolerance enables a drastic reduction of the mass error in the presence of wetting and drying fronts.
The effectiveness and robustness of the proposed scheme were assessed by comparing numerical results with the analytical and reference solutions of a set of test cases. Finally, to check the numerical model to field-scale applications, the results of two hypothetical dam-break events are reported.
This thesis is organized as follows.
In Chapter 2 the hyperbolic system of shallow water equations is introduced, outlining the main mathematical properties. The theoretical solution of the Riemann problem, which is at the basis of Godunov-type methods, is developed.
In Chapter 3, after a brief review about finite-volume methods, all the numerical aspects featuring the proposed WSDGM are described in depth.
In Chapter 4 several analytical and reference solutions are compared to those obtained by WSDGM. These problems, not frequently reported in the literature, were chosen to test the scheme on critical situations due to high-slopes, wet/dry fronts and the arising of complex structures in the flow field.
In Chapter 5 the numerical results concerning dam-break events are reported. For one of them a sensitivity analysis with respect to some parameters influencing the dynamics is carried out.

Chapter 2

The Shallow Water Equations

2D Shallow Water Equations (SWE) are widely accepted to mathematically model a great variety of rapidly varying free surface flows, as, for example, dam break waves, flood waves in rivers, tides in oceans, etc. Such equations derive from the conservation principles of mass and momentum that govern the dynamics of this kind of phenomena; under the key assumption of a hydrostatic pressure distribution, the resulting SWE are a time-dependent, two-dimensional system of non-linear partial differential equations of hyperbolic type. Due to their hyperbolic character, these equations admit discontinuous solutions that can develop spontaneously even from smooth initial data. For this reason a particular attention has to be devoted to the integral (*weak*) form of conservation laws, since, unlike the differential form, it continues to hold also in the presence of discontinuities, such as shocks, contact discontinuities, shear waves, wet/dry fronts, etc.

In the following sections SWE will be derived starting from the conservation principles; moreover the basic mathematical properties and the characteristic structure of such equations will be outlined. These elements are fundamental in the development of the solution of the so called *Riemann problem*, that is an initial value problem (IVP) in which the SWE are coupled with special initial data, that are piecewise constant with a single jump discontinuity at some point.

This simple problem allows to understand the structure of more general solutions and it is also a fundamental tool in the development of finite-volume numerical methods.

The waves we are going to modeling are usually called *gravity* waves, since they

are driven by the hydrostatic pressure. For a hyperbolic system of m non-linear equations, in the solution of the Riemann problem m different waves will arise from the initial discontinuity. Differently from the linear situation (corresponding to waves of small amplitude with respect to water depth) in which the waves propagate unchanged, the non-linearity of the SWE leads to a wave distortion, since the wave speed depends on the water depth h; however, the simplicity of the non-linear structure allows to explicitly solve the Riemann problem.

2.1 Conservation Principles

Given a vector $q : \mathbb{R} \times \mathbb{R} \rightarrow \mathbb{R}^m$, whose m-components represent the density of some conserved quantity depending on time t and on the space dimension x, conservation laws arise most naturally from physical laws expressed in integral form analogous to the following:

$$\frac{d}{dt}\int_{x_1}^{x_2} q\,(x,t)\,dx = f\,(q\,(x_1,t)) - f\,(q\,(x_2,t)) + \int_{x_1}^{x_2} s\,(q\,(x,t))\,. \tag{2.1}$$

Eq.(2.1) simply states that the 'total mass' connected with q between two points x_1 and x_2 can change only due to the passage of fluid represented by the flux function $f \in \mathbb{R}^m$ past the endpoints and to the action of external forces accounted in $s \in \mathbb{R}^m$ [8, 44].

The motion of a fluid is governed by the physical principles of conservation of mass (*continuity equation*) and momentum (*Navier-Stokes equation*). In practical applications when a free surface is present the fluid is assumed as incompressible, thus the equation of state is reduced to the simple condition of density ρ constant.
In a Cartesian frame of reference (x, y, z), given V as an arbitrary control volume of a fluid element and Ω its boundary, the conservation laws written in integral form have the expression [8, 20]:

$$\int_{\Omega} \mathbf{n} \cdot \mathbf{u}\; d\Omega = 0, \tag{2.2}$$

$$\int_V \frac{\partial}{\partial t}(\mathbf{u})\, dV = \int_V \mathbf{g}\, dV - \frac{1}{\rho}\int_\Omega p\mathbf{n}\, d\Omega + \frac{\mu}{\rho}\int_\Omega \frac{\partial \mathbf{u}}{\partial n}\, d\Omega, \tag{2.3}$$

where $\mathbf{n}$ is the unit vector outwarding Ω; $\mathbf{u} = [u, v, w]$ is the vector of the velocity components in x, y, z directions respectevely, $\mathbf{g} = [g_x, g_y, g_z]$ represents the vector of the components of external forces per unit mass, p is the pressure and μ is the dynamic viscosity.
From (2.2) and (2.3) the differential form of the *continuity equation* and the *Navier-Stokes equation* can be derived and are given respectively by [8]:

$$\nabla \mathbf{u} = 0, \tag{2.4}$$

$$\frac{D\mathbf{u}}{Dt} = \mathbf{g} - \frac{1}{\rho}\nabla p + \frac{\mu}{\rho}\nabla^2 \mathbf{u}. \tag{2.5}$$

2.2 The 2D Shallow Water Equations

Let's consider the motion of water with a free surface under gravity. The body force vector $\mathbf{g}$ is assumed $[0, 0, -g]$, where g is the acceleration due to gravity considered as constant and equal to $9.806\ \mathrm{m/s^2}$. $x - y$ determines a horizontal plane, while z defines the vertical direction, to which the free surface elevation is associated. As sketched in Fig.2.1, the domain on which the equations have to be solved is bounded by the bottom b and the free surface η, which are defined respectively by the functions:

$$\begin{aligned} &\text{bottom:} && z = b(x, y), \\ &\text{free surface:} && z = \eta(x, y, t) \equiv b(x, y) + h(x, y, t), \end{aligned} \tag{2.6}$$

where $h(x, y, t)$ is the depth of water.
The free surface is a boundary and, as such, the boundary conditions have to be satisfied. However, the free surface position is unknown, so the domain on which the equations have to be solved is not known *a priori*. Approximate theories allow to simplify this problem. In the particular case of shallow water theory the approximation of *small water depth* with respect to wave length or free surface curvature is introduced; this assumption leads to a *non-linear* initial value problem [67].

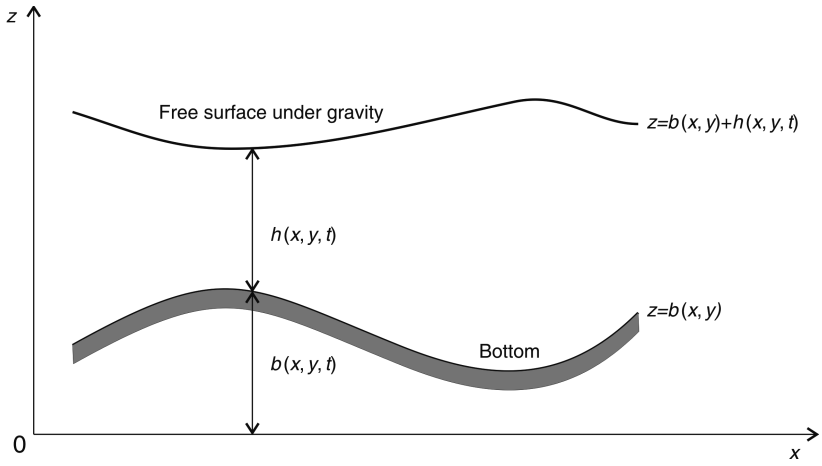

Figure 2.1. Flow with a free surface under the effect of gravity for a fixed section y.

Below the boundary conditions for the full problem will be derived. If a boundary is represented by the surface $\psi(x, y, z, t) = 0$, the free surface becomes:

$$\psi(x, y, z, t) \equiv z - \eta(x, y, t) = 0, \tag{2.7}$$

and the bottom:

$$\psi(x, y, z, t) \equiv z - b(x, y) = 0. \tag{2.8}$$

A *kinematic* condition

$$\frac{\mathrm{d}}{\mathrm{d}t}\psi(x, y, z, t) = \psi_t + u\psi_x + v\psi_y + w\psi_z = 0 \tag{2.9}$$

is imposed both on the free surface (with ψ given by (2.7)) and on the bottom (with ψ given by (2.8)), while on the free surface holds also the *dynamical*

condition:

$$p(x,y,z,t)|_{z=\eta(x,y)} = p_{atm} = 0, \tag{2.10}$$

where p_{atm} is the atmospheric pressure, taken to be identically zero.
SWE can be derived from the integration of (2.4) and (2.5) on the vertical coordinate, between the bottom $z = b(x,y)$ and the free surface $z = \eta(x,y,t)$, together with the imposition of the boundary conditions and further mathematical manipulations [67].
Under the hypothesis of horizontal scales much larger than the vertical ones, the vertical component of acceleration can be neglected. This assumption, together with the dynamical condition (2.10) of $p_{atm} = 0$ on the free surface, is equivalent to assuming the pressure distribution as *hydrostatic*.
In differential conservation law form and written as a single vector equation, two-dimensional SWE result [67]:

$$\frac{\partial \mathbf{U}}{\partial t} + \frac{\partial}{\partial x}\mathbf{F}(\mathbf{U}) + \frac{\partial}{\partial y}\mathbf{G}(\mathbf{U}) = \mathbf{S}(\mathbf{U}), \tag{2.11}$$

with

$$\begin{aligned} \mathbf{U} &= \begin{bmatrix} h \\ hu \\ hv \end{bmatrix}, & \mathbf{F}(\mathbf{U}) &= \begin{bmatrix} hu \\ hu^2 + \frac{1}{2}gh^2 \\ huv \end{bmatrix}, \\ \mathbf{G}(\mathbf{U}) &= \begin{bmatrix} hv \\ huv \\ hv^2 + \frac{1}{2}gh^2 \end{bmatrix}, & \mathbf{S}(\mathbf{U}) &= \begin{bmatrix} 0 \\ gh\left(S_{0x} - S_{fx}\right) \\ gh\left(S_{0y} - S_{fy}\right) \end{bmatrix}. \end{aligned} \tag{2.12}$$

In (2.11) $\mathbf{U}$ is the vector of the conserved variables (water depth and specific discharge in x and y directions), $\mathbf{F}(\mathbf{U})$ and $\mathbf{G}(\mathbf{U})$ are the flux vectors in x and y direction respectively and $\mathbf{S}(\mathbf{U})$ represents the vector of the source terms in which, neglecting the forcing effects due to wind and Coriolis forces, only the terms induced by the gravity field in the presence of a non-flat bottom and by the bottom friction are considered.
In particular, bottom slopes S_{0x} and S_{0y} in x and y directions have the expres-

sion:

$$S_{0x}(x,y,t) = -\frac{\partial b(x,y,t)}{\partial x}, \quad S_{0y}(x,y,t) = -\frac{\partial b(x,y,t)}{\partial y}. \tag{2.13}$$

The bed resistance is the only form of momentum dissipation incorporated into shallow water model; in Eq.(2.3) the viscous term $\int_\Omega \frac{\partial \mathbf{u}}{\partial n}\, d\Omega$ can be replaced by $\int_{\Omega_0} \frac{\partial \mathbf{u}}{\partial n}\, d\Omega$, where Ω_0 is the bottom boundary and such contribution is generally computed through empirical equations containing some roughness coefficient. In the one dimensional system of equations the average bed stress can be expressed as gRS_f, where S_f denotes the energy slope and R the hydraulic radius. Assuming that the frictional force in a two dimensional unsteady flow can be estimated by referring to empirical formulas, e.g. the Manning formula, and considering a unit-width channel in which $R = h$, the final expression of the friction slopes in x and y direction becomes:

$$S_{fx}(x,y,t) = \frac{n^2 u\sqrt{u^2+v^2}}{h^{4/3}}, \quad S_{fy}(x,y,t) = \frac{n^2 v\sqrt{u^2+v^2}}{h^{4/3}}, \tag{2.14}$$

where n is the Manning coefficient.
The integral (*weak*) form of the shallow water equations may be expressed as [67]:

$$\frac{\partial}{\partial t}\int_V \mathbf{U} dV + \int_\Omega \mathbf{n}\cdot\mathbf{H}(\mathbf{U})\, d\Omega = \int_V \mathbf{S}(\mathbf{U})\, dV, \tag{2.15}$$

where $\mathbf{n}\cdot\mathbf{H}(\mathbf{U})$ is the normal flux component through Ω and $\mathbf{H}(\mathbf{U}) = (\mathbf{F}, \mathbf{G})$ is the flux tensor. As specified before, this integral form admits discontinuous solutions, unlike the differential form which derives from Eq.(2.15) assuming the solution is sufficiently smooth [44].

2.3 Properties of the Equations

2.3.1 Eigenstructure and hyperbolicity of the equations

The eigenstructure of SWE plays a fundamental role in understanding the mathematical character of the governing equations as well as in studying the physical character of shallow water free-surface waves.
Eq.(2.11) may be written in *quasi-linear* form as [67]:

$$\frac{\partial \mathbf{U}}{\partial t} + \mathbf{A}(\mathbf{U}) \frac{\partial}{\partial x}\mathbf{U} + \mathbf{B}(\mathbf{U}) \frac{\partial}{\partial y}\mathbf{U} = 0, \tag{2.16}$$

where $\mathbf{A}(\mathbf{U})$ and $\mathbf{B}(\mathbf{U})$ are the *Jacobian matrices* corresponding to the fluxes $\mathbf{F}(\mathbf{U})$ and $\mathbf{G}(\mathbf{U})$ respectively. The expression of $\mathbf{A}(\mathbf{U})$ and $\mathbf{B}(\mathbf{U})$ is given by:

$$\mathbf{A}(\mathbf{U}) = \begin{bmatrix} 0 & 1 & 0 \\ a^2 - u^2 & 2u & 0 \\ -uv & v & u \end{bmatrix}, \ \mathbf{B}(\mathbf{U}) = \begin{bmatrix} 0 & 0 & 1 \\ -uv & v & u \\ a^2 - v^2 & 0 & 2v \end{bmatrix}, \tag{2.17}$$

where $a = \sqrt{gh}$ is the relative propagation speed of the small-amplitude waves (*celerity*).
Although Eq.(2.16) is written in term of the conserved variables, such formulation is not *conservative*, because it is equivalent to Eq.(2.11) only in the case of smooth solutions.
The eigenvalues related to the matrix $\mathbf{A}(\mathbf{U})$ are:

$$\lambda_{A1} = u - a, \ \ \lambda_{A2} = u, \ \ \lambda_{A3} = u + a \tag{2.18}$$

and the corresponding eigenvectors:

$$r_{A1} = \begin{bmatrix} 1 \\ u - a \\ v \end{bmatrix}, \ r_{A2} = \begin{bmatrix} 0 \\ 0 \\ 1 \end{bmatrix}, \ r_{A1} = \begin{bmatrix} 1 \\ u + a \\ v \end{bmatrix}. \tag{2.19}$$

Similarly for $\mathbf{B}(\mathbf{U})$:

$$\lambda_{B1} = v - a, \;\; \lambda_{B2} = u, \;\; \lambda_{B3} = v + a, \tag{2.20}$$

$$r_{B1} = \begin{bmatrix} 1 \\ u \\ v - a \end{bmatrix}, \; r_{B2} = \begin{bmatrix} 0 \\ 1 \\ 0 \end{bmatrix}, \; r_{B1} = \begin{bmatrix} 1 \\ u \\ v + a \end{bmatrix}. \tag{2.21}$$

A system of m conservation laws with *Jacobian* matrices $\mathbf{A}(\mathbf{U})$ and $\mathbf{B}(\mathbf{U})$ is said to be *hyperbolic* if the matrix $\mathbf{C} = \omega_1 \mathbf{A}(\mathbf{U}) + \omega_2 \mathbf{B}(\mathbf{U})$, that is the linear combination between $\mathbf{A}(\mathbf{U})$ and $\mathbf{B}(\mathbf{U})$, has m real eigenvalues for any vector $\mathbf{U}$ of conserved variables and any vector $\omega = [\omega_1, \omega_2]$, such that $|\omega| \neq 0$. The system is *strictly hyperbolic* if the eigenvalues are all distinct.
If $\mathbf{A}(\mathbf{U})$ and $\mathbf{B}(\mathbf{U})$ are defined as in (2.17), the eigenvalues for the matrix $\mathbf{C}$ are given by:

$$\lambda_{C1} = u\omega_1 + v\omega_2 - a\,|\omega|\,, \;\; \lambda_{C2} = u\omega_1 + v\omega_2, \;\; \lambda_{C3} = u\omega_1 + v\omega_2 + a\,|\omega|\,, \tag{2.22}$$

hence it is demonstrated that the time-dependent, two-dimensional *shallow water equations* are *hyperbolic* and, in case of a wet bed, they are *strictly hyperbolic* [67].

2.3.2 Nature of Characteristic Fields

Given a hyperbolic system of m conservation laws of the form:

$$\frac{\partial \mathbf{U}}{\partial t} + \frac{\partial}{\partial x}\mathbf{F}(\mathbf{U}) = 0, \tag{2.23}$$

with real eigenvalues $\lambda_i(\mathbf{U})$ and corresponding right eigenvectors $r_i(\mathbf{U})$, the *characteristic speed* λ_i defines a *characteristic field*, the λ_i-field.
A λ_i-characteristic field is said to be *linearly degenerate* if:

$$\nabla \lambda_i(\mathbf{U}) \cdot r_i(\mathbf{U}) = 0, \;\; \forall \mathbf{U} \in \mathbb{R}^m \tag{2.24}$$

and it is said to be *genuinely non-linear* if:

$$\nabla\lambda_i(\mathbf{U}) \cdot r_i(\mathbf{U}) \neq 0, \quad \forall \mathbf{U} \in \mathbb{R}^m. \tag{2.25}$$

If (2.23) represents the 2D x-split SWE, $\mathbf{U}$ and $\mathbf{F}(\mathbf{U})$ are defined as in (2.12), while λ_i and r_i as in (2.18) and (2.19) respectively.
It can be proved [67] that λ_1 and λ_3 characteristic fields satisfy the (2.25), hence they are *genuinely non-linear*. From a physical point of view it means that a smooth simple wave in one of these fields will always distort via a compression or an expansion as characteristics converge or diverge [44]. The characteristic field associated with $\lambda_2 = u$, satisfying (2.24), is *linear degenerate* [67]: since λ_2 is constant throughout the wave, it simply translates with this constant velocity without distorting [44].

2.4 The Riemann Problem

The Riemann problem is an initial value problem, in which the governing equations are coupled with piecewise constant data imposed at the left-side and at the right-side of $x = 0$, where the discontinuity is placed.
Formally the IVP is given by:

$$\left.\begin{array}{l} \dfrac{\partial \mathbf{U}}{\partial t} + \dfrac{\partial}{\partial x}\mathbf{F}(\mathbf{U}) = 0 \\ \mathbf{U}(x,0) = \begin{cases} \mathbf{U}_L & \text{if } x < 0 \\ \mathbf{U}_R & \text{if } x > 0 \end{cases} \end{array}\right\}. \tag{2.26}$$

In (2.26) the x-split 2D SWE define a one-dimensional augmented problem where $\mathbf{U}$ and $\mathbf{F}(\mathbf{U})$ are defined as in (2.12), while the vectors of conserved variables constituting the initial jump, are given by:

$$\mathbf{U}_L = \begin{bmatrix} h_L \\ h_L u_L \\ h_L v_L \end{bmatrix}, \mathbf{U}_R = \begin{bmatrix} h_R \\ h_R u_R \\ h_R v_R \end{bmatrix}. \tag{2.27}$$

Being the SWE a hyperbolic system of three equations, in the solution of the Riemann problem the initial jump will be always splitted in three separate waves, which give rise to four possible wave patterns, as depicted in Fig. 2.2. The left and the right waves, corresponding to purely 1D SWE, are *shocks* or *rarefactions*, characterized respectively by a *discontinuous* and a *smooth* variation in the solution. The middle wave, drawn in dashed line, arises from the presence of the y momentum equation in (2.26); it is a *shear wave*, across which the tangential velocity component v changes discontinuously.

The three waves, associated with the eigenvalues λ_1, λ_2, λ_3, separate four

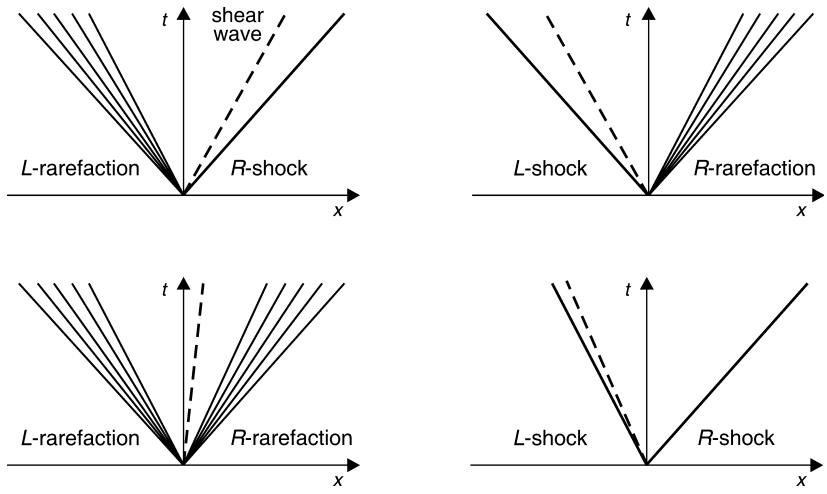

Figure 2.2. Possible wave patterns in the solution of the Riemann problem for the x-split SWE.

constant state denoted from left to right by $\mathbf{U}_L$, $\mathbf{U}_{*L}$, $\mathbf{U}_{*R}$ and $\mathbf{U}_R$; the symbol $*$ refers to the unknown intermediate state usually called *star region*. The complete solution is a *similarity* solution $\mathbf{U}(x/t)$, that is $\mathbf{U}$ depends on the ratio x/t.

To compute the exact solution of the Riemann problem it necessary to determine:

- whether each of the left and right waves is a shock or a rarefaction;
- the intermediate state $\mathbf{U}_*$;

- the state inside the *fan-like* structure of rarefaction waves.

In next sections special situations in which a single wave from one of the characteristic families can be studied in isolation are presented: such results are the basis for the solution of any Riemann problem in which different waves arise.

2.4.1 Shock Waves

The shock wave is a *jump discontinuity* in a *genuinely non-linear field* that connects a fixed constant state $\mathbf{U}$ ($\mathbf{U}_L$ or $\mathbf{U}_R$) to an unknown constant state $\mathbf{U}_*$. Given S as the shock speed, across any shock the *Rankine-Hugoniot* condition [67, 44]

$$S\left(\mathbf{U}-\mathbf{U}_*\right)=\mathbf{F}\left(\mathbf{U}\right)-\mathbf{F}\left(\mathbf{U}_*\right) \tag{2.28}$$

must be satisfied. For the system of x-split 2D SWE, the wave relation (2.28) becomes:

$$\begin{cases} S\left(h-h_*\right)=hu-h_*u_* \\ S\left(hu-h_*u_*\right)=hu^2-h_*u_*^2+\dfrac{1}{2}g\left(h^2-h_*^2\right) \\ S\left(hv-h_*v_*\right)=huv-h_*u_*v_*. \end{cases} \tag{2.29}$$

Since (2.29) is a system of three equations with four unknowns h_*, u_*, v_*, S, the solution has to be provided in a parametric form; choosing h_* as the parameter, after some mathematical passages, the solution is given by:

$$\begin{cases} S=\dfrac{hu-h_*u_*}{h-h_*} \\ u_*=u\pm\sqrt{\dfrac{g}{2}\left(\dfrac{h}{h_*}-\dfrac{h_*}{h}\right)\left(h-h_*\right)} \\ v_*=v \end{cases} \tag{2.30}$$

The result for v_* implies that the tangential velocity component maintains constant across the shock.

The two solutions of u_* correspond to two different families of shock, named *left* and *right* shocks. Each parameter-family represents all the possible states $\mathbf{U}_*$ that can be connected with the fixed state $\mathbf{U}$ through a discontinuity. The set of states is called *Hugoniot locus* and it can be represented as a curve in the $h - hu$ plane (*phase plane*) [44].
Choosing a single sign in Eq.(2.28), one obtains part of one locus and part of the other as h varies. To distinguish which curve corresponds to the left-shock and which to the right-shock, it is necessary to multiply u by h in (2.28) and reparametrize by a value α, with $h_* = h + \alpha$; then the case of a weak shock ($\mathbf{U} \approx \mathbf{U}_* \to \alpha$ very small) for which the linearized theory holds has to be considered [44].
Finally, the curve of states $\mathbf{U}_*$ that can be connected to $\mathbf{U}_L$ by a left-shock has the expression:

$$u_* = u_L - (h_* - h_L)\sqrt{\frac{g}{2}\left(\frac{1}{h_*} + \frac{1}{h_L}\right)}. \tag{2.31}$$

Similarly, the family of $\mathbf{U}_*$ states connected to $\mathbf{U}_R$ by a right-shock is:

$$u_* = u_R + (h_* - h_R)\sqrt{\frac{g}{2}\left(\frac{1}{h_*} + \frac{1}{h_R}\right)}. \tag{2.32}$$

Since not all the states lying on the *Hugoniot locus* are meaningful from the physical point of view, it is necessary to adopt a further criterion to establish which are the correct states connected to $\mathbf{U}_L$ or $\mathbf{U}_R$ through a shock.
A discontinuity of speed S connecting two states $\mathbf{U}_L$ and $\mathbf{U}_R$ has to satisfy also the *Lax entropy condition* [67, 44], i.e. it has to exists an index i such that:

$$\lambda_i(\mathbf{U}_L) > S > \lambda_i(\mathbf{U}_R), \tag{2.33}$$

so that the i-characteristic are impinging on the discontinuity, while the other characteristics are crossing the discontinuity, as specified by the following rela-

tions:

$$\begin{aligned} &\lambda_j(\mathbf{U}_L) < s \ \text{ and } \ \lambda_j(\mathbf{U}_R) < s \quad \text{for } j < i, \\ &\lambda_j(\mathbf{U}_L) > s \ \text{ and } \ \lambda_j(\mathbf{U}_R) > s \quad \text{for } j > i. \end{aligned} \tag{2.34}$$

This condition can be shown to be correct for strictly hyperbolic conservation laws in which each field is *genuinely non-linear* as defined by Eq.(2.25).
The entropy condition states that across a *left* shock connecting the states $\mathbf{U}_L$ and $\mathbf{U}_*$, the characteristic velocity $\lambda_1 = u - a$ must decrease; such condition, together with the Rankine-Hugoniot relation, implies that, in order to obtain a physical acceptable solution, the water depth must increase, so $h_* > h_L$. Similarly, for a right shock connecting $\mathbf{U}_R$ to $\mathbf{U}_*$ and related to the characteristic velocity $\lambda_3 = u + a$, $h_* > h_R$ must hold.
Fig.2.3 shows the elementary shock solution in the $x - t$ plane.

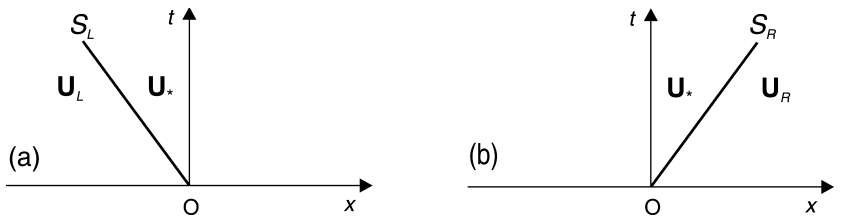

Figure 2.3. Elementary wave solution of the Riemann problem: isolated (a) left and (b) right shock wave.

2.4.2 Rarefaction Waves

Rarefaction waves represent *smooth varying solutions* of SWE connecting two data states and they are associated with only one characteristic family (λ_1 or λ_3) of the system. Besides these properties typical of the so-called *simple* waves, centered rarefaction waves are also a *similarity solution* of the equations, that is $\mathbf{U}(x,t) = \widetilde{\mathbf{U}}(x/t)$ and are constant along every ray x/t =constant. Such waves show a *fan-like* structure centered at the origin with all quantities varying continuously across the wave at any fixed time. However, across the bounding characteristic corresponding to the *head* and the *tail*, the flow variables have a

discontinuity in the x-derivative.
In the following part, a brief widening about the theoretical background [44] of rarefaction waves is presented, in order to clarify the origin of some mathematical relations fundamental in analytically solving such structures.
Given $\widetilde{\mathbf{U}}(\xi)$ as a smooth curve through the phase plane parametrized by a scalar quantity ξ, it is said to be an *integral curve* of the vector field r_i if, at each point $\widetilde{\mathbf{U}}(\xi)$, the tangent vector to the curve, $\widetilde{\mathbf{U}}'(\xi)$, is an eigenvector of the Jacobian matrix $\mathbf{A}\big(\widetilde{\mathbf{U}}(\xi)\big)$ corresponding to the eigenvalue $\lambda_i\big(\widetilde{\mathbf{U}}(\xi)\big)$. If $r_i(\mathbf{U})$ is a particular set of eigenvector, the following relation must hold:

$$\widetilde{\mathbf{U}}'(\xi) = \alpha(\xi)\; r_i\big(\widetilde{\mathbf{U}}(\xi)\big), \tag{2.35}$$

where $\alpha(\xi)$ is a scalar quantity. Eq.(2.35) states that the tangent to the curve has to be in the direction of the eigenvector r_i evaluated at the point on the curve.
For x-split 2D SWE and for a fixed point $\big(\overline{h}, \overline{u}, \overline{v}\big)$, choosing $\alpha(\xi) = 1$ and setting $\widetilde{\mathbf{U}}^1 = \xi$ (that is parameterizing the curve through h), the functional form of the integral curves of r_1 can be expressed as:

$$u = \overline{u} + 2h\left(\sqrt{g\overline{h}} - \sqrt{gh}\right). \tag{2.36}$$

The result for the tangential velocity component is:

$$v = \overline{v}, \tag{2.37}$$

which means that v remains constant across the wave associated with the 1-field.
Similarly, the integral curves for r_3 passing through the point $\big(\overline{h}, \overline{u}, \overline{v}\big)$ have the expression:

$$u = \overline{u} + 2h\left(\sqrt{g\overline{h}} + \sqrt{gh}\right), \tag{2.38}$$

$$v = \overline{v}. \tag{2.39}$$

If $\left(\overline{h}, \overline{u}, \overline{v}\right)$ and (h, u, v) are two different points on the same curve, it can be observed that the quantity $w_1(\mathbf{U}) = u + 2\sqrt{gh}$, called *Riemann invariant* for the 1-family, remains constant along the curve of r_1.
Similarly, from (2.38) the function $w_3(\mathbf{U}) = u - 2\sqrt{gh}$, which remains constant along the curve of r_3, represents the *Riemann invariant* for the 3-family. Generally, the integral curves can be considered as the contour lines of w_i and it can be demonstrated [44] that the gradient of w_i is orthogonal to the contour lines.
A *simple wave* is a special solution of the conservation laws in which:

$$\mathbf{U}(x,t) = \widetilde{\mathbf{U}}(\xi(x,t)), \tag{2.40}$$

where $\widetilde{\mathbf{U}}(\xi)$ traces out an integral curve of some family of eigenvectors r_i and $\xi(x,t)$ is a smooth mapping from (x,t) to ξ. Thus, all states $\mathbf{U}(x,t)$ lie on the same integral curve and the Riemann invariant w_i maintains constant along such curve.
In order to find a solution for the conservation laws that is physically meaningful, the further condition of characteristic speed $\lambda_i\big(\widetilde{\mathbf{U}}(\xi(x,0))\big)$ monotonically increasing in x has to be satisfied. In this way, the characteristics will always be spreading out and the smooth solution will exist all the time without breaking. If $\lambda_i\big(\widetilde{\mathbf{U}}(\xi)\big)$ varies monotonically with ξ along every integral curve, the i-field is *genuinely non-linear*. In fact, the variation of λ_i along the curve can be computed as:

$$\frac{d}{d\xi}\lambda_i\big(\widetilde{\mathbf{U}}(\xi)\big) = \nabla\lambda_i\big(\widetilde{\mathbf{U}}(\xi)\big) \cdot \widetilde{\mathbf{U}}'(\xi) \tag{2.41}$$

and adding (2.35) it leads to:

$$\nabla\lambda_i(\mathbf{U}) \cdot r_i(\mathbf{U}) \neq 0, \tag{2.42}$$

that is exactly the condition of *genuinely non-linearity* for the r_i-field expressed by Eq.(2.25).
A *centered rarefaction wave* is a *simple wave* in a *genuinely non-linear* field, in which $\xi(x,t) = x/t$, so the solution is constant along rays through the origin. Thanks to the particular parametrization and given that ξ must be equal to the

characteristic speed $\lambda_i\big(\widetilde{\mathbf{U}}(\xi)\big)$ at each point, a centered rarefaction wave has the following form:

$$\mathbf{U}(x,t) = \begin{cases} \mathbf{U}_L & \text{if } x/t \leq \lambda_i(\mathbf{U}_L) \\ \widetilde{\mathbf{U}}(x/t) & \text{if } \lambda_i(\mathbf{U}_L) \leq x/t \leq \lambda_i(\mathbf{U}_R) \\ \mathbf{U}_R & \text{if } x/t \geq \lambda_i(\mathbf{U}_R), \end{cases} \tag{2.43}$$

where $\mathbf{U}_L$ and $\mathbf{U}_R$ are two points on a single integral curve with $\lambda_i(\mathbf{U}_L) < \lambda_i(\mathbf{U}_R)$ (condition that makes the rarefaction physically acceptable).
For SWE the complete solution for a rarefaction wave smoothly connecting a fixed state $\mathbf{U}$ ($\mathbf{U}_L$ or $\mathbf{U}_R$) to an intermediate state $\mathbf{U}_*$ can be derived [67].
If $h_* \leq h_L$ then a *left* rarefaction will occur; the speeds of the *head* and the *tail* are respectively:

$$\begin{aligned} &\text{head:} \quad \lambda_1(\mathbf{U}_L) = u_L - a_L, \\ &\text{tail:} \quad \lambda_1(\mathbf{U}_*) = u_* - a_*. \end{aligned} \tag{2.44}$$

The solution for any point $\mathrm{P} = (x,t)$ inside the fan-like structure of the rarefaction can be find considering that P is connected to the origin $(0,0)$ through a characteristic of speed $x/t = u - a$ (u and a are respectively the speed and the celerity of P) and to the left data state through the w_1 Riemann invariant. The final solution becomes:

$$\begin{aligned} a_{L\,fan} &= \frac{1}{3}\left(u_L + 2a_L - \frac{x}{t}\right), \\ u_{L\,fan} &= \frac{1}{3}\left(u_L + 2a_L + \frac{2x}{t}\right). \end{aligned} \tag{2.45}$$

Given a fixed state $\mathbf{U}_R$ and an intermediate state $\mathbf{U}_*$, if $h_* \leq h_R$, a *right* rarefaction will occur and, similarly to the previous case, the speed of the *head* and the *tail* for the right wave are respectively:

$$\begin{aligned} &\text{head:} \quad \lambda_3(\mathbf{U}_R) = u_R + a_R, \\ &\text{tail:} \quad \lambda_3(\mathbf{U}_*) = u_* + a_*. \end{aligned} \tag{2.46}$$

The solution for u and a inside the rarefaction fan is:

$$\begin{aligned} a_{R\,fan} &= \frac{1}{3}\left(-u_R + 2a_R - \frac{x}{t}\right), \\ u_{R\,fan} &= \frac{1}{3}\left(u_R - 2a_R + \frac{2x}{t}\right). \end{aligned} \tag{2.47}$$

Fig.2.4 summarizes the wave configuration for a left and a right isolated rarefaction.

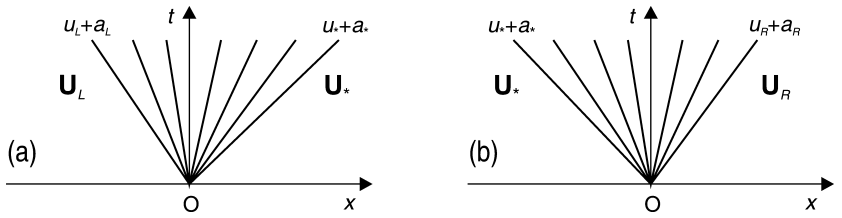

Figure 2.4. Elementary wave solution of the Riemann problem: isolated (a) left and (b) right rarefaction wave.

2.4.3 Shear waves

Shear waves are *discontinuous solutions* across which the tangential velocity component v presents a jump. $\mathbf{U}_{*L}$ and $\mathbf{U}_{*R}$, that represent the states on the left and the right side of the wave, are connected through a single jump discontinuity of speed S in the *characteristic field* $i = 2$. Such field is said to be *linearly degenerate*, since it satisfies (2.24), that means $\lambda_2(\mathbf{U}) = \text{constant}$ along each integral curve of r_2. Given that λ_2 is not varying throughout the wave, it simply translates with this constant speed without distorting. If the initial data represent a jump discontinuity with $\mathbf{U}_{*L}$ and $\mathbf{U}_{*R}$ both lying on a single integral curve of this field, the solution will consist of this discontinuity propagating at the constant speed λ_2 associated with this integral curve. Hence, the Hugoniot locus for this field agrees with the integral curve. Such a discontinuity is not a shock, because the characteristic speed $\lambda_2(\mathbf{U}_{*L}) = \lambda_2(\mathbf{U}_{*R})$ (parallel characteristics) on each side coincides with the speed S of the shear wave. From

the constancy of the Riemann invariants ($\widetilde{\mathbf{U}}' = r_2\left(\widetilde{\mathbf{U}}\right)$) across the 2-wave the following relations can be derived:

$$h = \text{constant}, \quad u = \text{constant}, \quad v \neq \text{constant}. \tag{2.48}$$

In terms of initial data the solution becomes:

$$h_{*L} = h_{*R}, \quad u_{*L} = u_{*R}, \quad v_{*L} \neq v_{*R}, \tag{2.49}$$

The water depth h and the normal component of the velocity u are both constant across the shear wave; the only quantity that changes discontinuously is the tangential velocity component v.
Contact waves or *contact discontinuities* arising from pollutant transport models behaves identically to shear waves. In Fig.2.5 the shear wave solution in the $x-t$ plane is sketched.

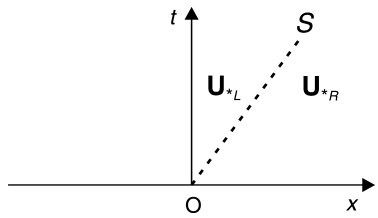

Figure 2.5. Elementary wave solution of the Riemann problem: isolated shear wave.

2.5 Solving the Dam-Break Problem

The dam-break problem is a special case of the Riemann problem (2.26), in which the discontinuity placed at $x = 0$ separates two constant states $\mathbf{U}_L$ and $\mathbf{U}_R$ of water at rest ($u_L = u_R = 0$) (Fig.2.6). Such problem is of great physical interest, since it models the flow dynamics consequent to the hypothetical collapse of an idealized dam; in order that SWE correctly describe the phenomenon under investigation, the failure has is assumed as instantaneous. After the col-

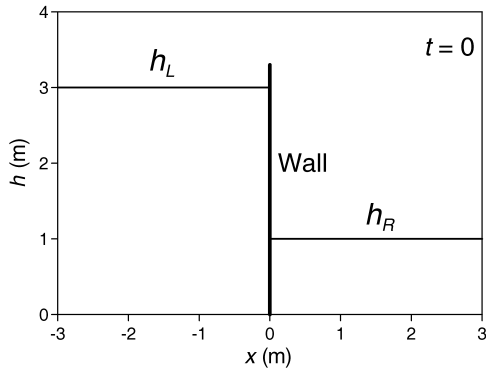

Figure 2.6. Initial condition for the dam-break problem ($h_R = 3\,\mathrm{m}$ and $h_L = 1\,\mathrm{m}$).

lapse a *right*-shock travels into the stationary water with $h = h_R$, raising the depth abruptly at a value h_* and accelerating the fluid instantaneously. A *left*-rarefaction wave travels into the deep water region with the effect of reducing the water surface level with a smooth transition between $\mathbf{U}_*$ and $\mathbf{U}_L$.
The intermediate state $\mathbf{U}_*$ must lie on the integral curve of r_1 passing through $\mathbf{U}_L$, that is:

$$u_* = u_L + 2\left(\sqrt{gh_L} - \sqrt{gh_*}\right), \tag{2.50}$$

and, simultaneously, it must lie also on the Hugoniot locus of *left*-shocks passing through $\mathbf{U}_R$, as expressed by:

$$u_* = u_R + (h_* - h_R)\sqrt{\frac{g}{2}\left(\frac{1}{h_*} + \frac{1}{h_R}\right)}. \tag{2.51}$$

The intersection between these two curves gives the solution for the intermediate state, as shown in Fig.2.7. It can be proved [44] that constructing the solution for the dam-break problem consisting of two shocks, one of them does not satisfies the Lax entropy condition; similarly, the all rarefaction solution is not physically realizable.

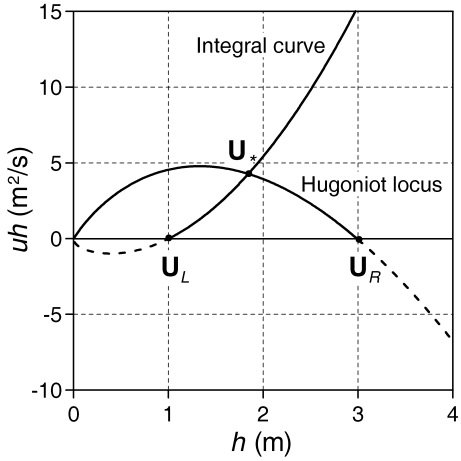

Figure 2.7. Intersection between the Hugoniot locus and the integral curve to find $\mathbf{U}_*$. In dashed line the unphysical states are represented.

Considering the dam-break problem for the augmented shallow water system (2.26), together with the rarefaction and the shock, a shear wave moves with velocity $\lambda_2 = u_*$. Across the 2-wave $h = h_*$ and $u = u_*$, while v jumps from v_L to v_R.
In Fig.2.8a,b water depth and velocity profiles at $t = 0.5$ s are shown, while Fig.2.8c summarizes the wave process as a function of space and time.
In Fig.2.9 the characteristic structure of the dam-break problem with initial data $h_L > h_R$ is reported.
The 1-characteristics (Fig.2.9a), related to the speed $dx/dt = \lambda_1 = u - a$, cross the right shock, while spread out through the left rarefaction and its edges move with the characteristic velocity in each constant region bounded by the rarefaction. The 2-characteristics (Fig.2.9b), related to $\lambda_2 = u$, cross the right-shock and the left-rarefaction and are parallel to the shear wave. The 3-characteristics (Fig.2.9c) cross the left rarefaction with a smooth change in velocity and impinge on the right shock.

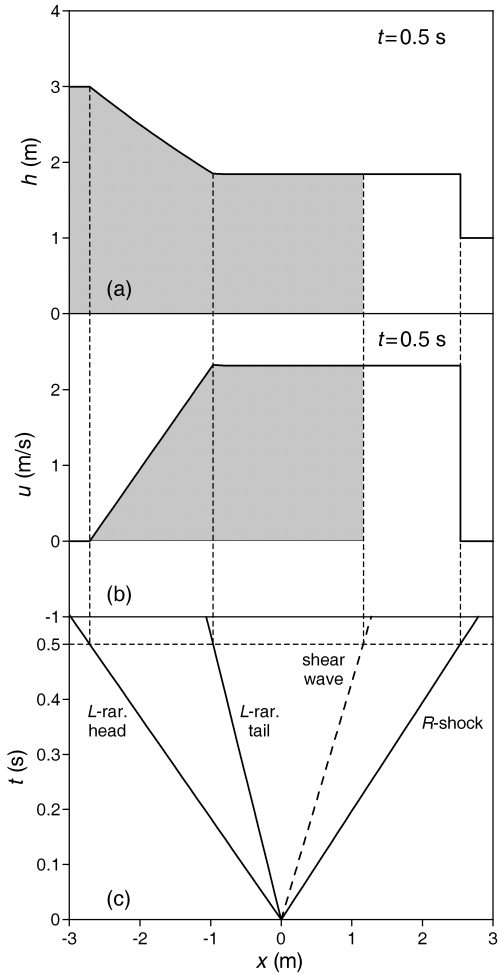

Figure 2.8. (a) Water depth profile at $t = 0.5$ s; (b) normal velocity profile at $t = 0.5$ s; (c) wave diagram of the full process in the $x - t$ plane. In the colored region $v = v_L$.

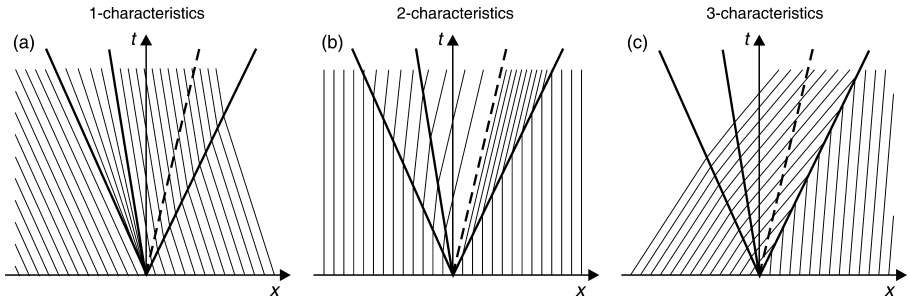

Figure 2.9. Solution of the dam-break problem in the $x-t$ plane. Thick lines represent the shock, the rarefaction and the shear wave; thin lines represent the 1,2,3-characteristics.

2.6 The general Riemann Solver for SWE

The solution h_* for the general Riemann problem (2.26) is given by the root of the algebraic equation [67]:

$$f(h) \equiv f_L(h, h_L) + f_R(h, h_R) + \Delta u = 0, \quad \Delta u = u_R - u_L, \tag{2.52}$$

where the functions f_L and f_R are:

$$f_L = \begin{cases} 2\left(\sqrt{gh} - \sqrt{gh_L}\right) & \text{if } h \le h_L \text{ (rarefaction)} \\ (h - h_L)\sqrt{\dfrac{g}{2}\left(\dfrac{h + h_L}{hh_L}\right)} & \text{if } h > h_L \text{ (shock)}, \end{cases} \tag{2.53}$$

$$f_R = \begin{cases} 2\left(\sqrt{gh} - \sqrt{gh_R}\right) & \text{if } h \le h_R \text{ (rarefaction)} \\ (h - h_R)\sqrt{\dfrac{g}{2}\left(\dfrac{h + h_R}{hh_R}\right)} & \text{if } h > h_R \text{ (shock)}. \end{cases} \tag{2.54}$$

It can be proved [67] that the solution for the particle velocity u_* in the star region is given by:

$$u_* = \frac{1}{2}\left(u_L + u_R\right) + \frac{1}{2}\left[f_R\left(h_*, h_R\right) - f_L\left(h_*, h_L\right)\right]. \tag{2.55}$$

The solution of (2.52) has to be computed applying a non-linear root finder, since there is no general closed-form solution of such equation [67, 44]. Studying the particular behavior of the function $f(h)$ it is possible to state *a priori*, for given data h_L, h_R, u_L, u_R, if the 1-wave and the 3-wave are shocks or rarefactions [67]. Given $h_m = \min\left(h_L, h_R\right)$ and $h_M = \max\left(h_L, h_R\right)$, the possible situations are:

$$\left.\begin{array}{lll} \text{if } f\left(h_M\right) < 0 & \text{then} & h_* \in (0, h_m] : \text{two rarefactions} \\ \text{if } f\left(h_m\right) \leq 0 \leq f\left(h_M\right) & \text{then} & h_* \in (h_m, h_M) : \text{one rar., one shock} \\ \text{if } f\left(h_m\right) \geq 0 & \text{then} & h_* \in [h_M, \infty) : \text{two shocks} \end{array}\right\}. \tag{2.56}$$

Since the limit case $h_* = 0$ corresponds to:

$$f(0) = -2\left(a_L + a_R\right) + u_R - u_L = 0, \tag{2.57}$$

in order to avoid unphysical negative water depths, the following *depth positivity condition* must be satisfied:

$$\left(\Delta u\right)_{crit} \equiv 2\left(a_L + a_R\right) > u_R - u_L. \tag{2.58}$$

Chapter 3

The Numerical Model

In this Chapter an explicit, finite-volume, MUSCL-type scheme for the numerical integration of 2D SWE is presented.
In the first paragraph the fundamentals of the finite volume methods for the discretization of the governing equations will be summarized. Then, a brief overview about the literature concerning the numerical techniques developed in recent years will introduce the challenges connected with the solution of SWE. The proposed *Weighted Surface Depth Gradient Method* scheme evaluates the averaged solution at the updated time step through a time-split algorithm, which separates the full integral problem into two parts; the first solves SWE including the bed slope source term and the second introduces the effects of friction. The discretization techniques adopted in the numerical model for the solution of the mentioned problems will be accurately described, underlining the novel elements introduced and the improvements brought to the code.

3.1 The Finite Volume Method

Recalling Chapter 2, the motion of a free surface flow under the effect of gravity is mathematically modeled by the hyperbolic system of SWE, that expresses the conservation laws of mass and momentum in a volume enclosed by a surface. The differential form of SWE (2.11) holds only under the assumption of a sufficiently smooth solution. In many cases the regularity of the solution cannot be guaranteed and the occurrence of discontinuities requires that conservation laws are expressed in the integral form (2.15).

The Finite Volume Method (FVM) [50, 47] is based on the direct discretization of the integral form of the conservation laws in the physical space. The computational domain is divided into non-overlapping *cells* and the conservation laws are applied on each of them in order to determine the flow variables at some discrete points of the cells, called *nodes*. Following a *cell-centered* [34] approach, the approximation of the integral of the conserved variable vector $\mathbf{U}$ is assigned to the barycenter of the grid element. At each time step the flow variables will be updated using an approximation of the fluxes through the cell-edges.
One of the great advantages of this technique is the flexibility given by the freedom in the choice of the mesh (*structured* or *unstructured*), of the cell-shape (quadrilateral, triangular, etc.) and of the rules and accuracy for the evaluation of the fluxes through the surfaces [34].
Referring to a 2D *structured* mesh, the two families of intersecting grid-lines are considered as curvilinear coordinate lines, so each control volume can be identified by a set of integers (i, j) [34]. For a *Cartesian* mesh composed by *quadrilateral* cells, the computational domain is divided into a set of elements $I_{i,j} = \left[x_{i-\frac{1}{2}}, x_{i+\frac{1}{2}}\right] \times \left[y_{j-\frac{1}{2}}, y_{j+\frac{1}{2}}\right]$, having area $|I_{i,j}| = \Delta x \times \Delta y$, where $\Delta x = x_{i+\frac{1}{2}} - x_{i-\frac{1}{2}}$ and $\Delta y = y_{i+\frac{1}{2}} - y_{i-\frac{1}{2}}$ represent the grid size in the two coordinate directions (Fig.3.1).
Let's recall the integral form of the homogeneous SWE [67]:

$$\frac{\partial}{\partial t}\int_V \mathbf{U} dV + \int_\Omega \mathbf{n}\cdot\mathbf{H}\left(\mathbf{U}\right) d\Omega = 0, \tag{3.1}$$

where V is a control volume in a 2D space and Ω is its boundary. Adopting the Cartesian computational cell $I_{i,j}$ as the control volume, the following expression:

$$\mathbf{U}^n_{i,j} \approx \frac{1}{|I_{i,j}|}\int_{y_{j-\frac{1}{2}}}^{y_{j+\frac{1}{2}}}\int_{x_{i-\frac{1}{2}}}^{x_{i+\frac{1}{2}}} \mathbf{U}\left(x, y, t^n\right) dx\, dy \tag{3.2}$$

represents the average value of $\mathbf{U}$ over the (i, j)-cell at time level t^n.
For the grid element $I_{i,j}$ Eq.(3.1) may be rewritten as:

$$\frac{d}{dt}\mathbf{U}_{i,j} = -\frac{1}{|I_{i,j}|}\sum_{s=1}^{4}\mathcal{F}_s, \tag{3.3}$$

with fluxes:

$$\mathcal{F}_s = \int_{l_s} \left[n_1 \mathbf{F}\left(\mathbf{U}\right) + n_2 \mathbf{G}\left(\mathbf{U}\right) \right] dl, \tag{3.4}$$

where l_s is the s-side of the cell and n_1 and n_2 are the components in x and y direction of the outwarding unit vector $\mathbf{n}$.
Integrating (3.3) in a time step $\Delta t = t^{n+1} - t^n$, one obtains:

$$\mathbf{U}_{i,j}^{n+1} = \mathbf{U}_{i,j}^{n} - \frac{1}{|I_{i,j}|} \sum_{s=1}^{4} \int_{t^n}^{t^{n+1}} \mathcal{F}_s \, dt \tag{3.5}$$

With reference to the Cartesian control volume $I_{i,j}$ sketched in Fig.3.1, the time integrals of fluxes $\mathcal{F}_s$ are:

$$\begin{aligned}
\int_{t^n}^{t^{n+1}} \mathcal{F}_1 \, dt &= \int_{t^n}^{t^{n+1}} \int_{x_{i+\frac{1}{2}}}^{x_{i-\frac{1}{2}}} -\mathbf{G}\Big(\mathbf{U}\big(x, y_{j-\frac{1}{2}}, t\big)\Big) dx \, dt \approx -\mathbf{G}_{i,j-\frac{1}{2}} \Delta x \Delta t, \\
\int_{t^n}^{t^{n+1}} \mathcal{F}_2 \, dt &= \int_{t^n}^{t^{n+1}} \int_{y_{i+\frac{1}{2}}}^{y_{i-\frac{1}{2}}} \mathbf{F}\Big(\mathbf{U}\big(x_{i+\frac{1}{2}}, y_j, t\big)\Big) dy \, dt \approx \mathbf{F}_{i+\frac{1}{2},j} \Delta y \Delta t, \\
\int_{t^n}^{t^{n+1}} \mathcal{F}_3 \, dt &= \int_{t^n}^{t^{n+1}} \int_{x_{i+\frac{1}{2}}}^{x_{i-\frac{1}{2}}} \mathbf{G}\Big(\mathbf{U}\big(x, y_{j+\frac{1}{2}}, t\big)\Big) \, dx \, dt \approx \mathbf{G}_{i,j+\frac{1}{2}} \Delta x \Delta t, \\
\int_{t^n}^{t^{n+1}} \mathcal{F}_4 \, dt &= \int_{t^n}^{t^{n+1}} \int_{y_{i+\frac{1}{2}}}^{y_{i-\frac{1}{2}}} -\mathbf{F}\Big(\mathbf{U}\big(x_{i-\frac{1}{2}}, y, t\big)\Big) \, dy \, dt \approx -\mathbf{F}_{i-\frac{1}{2},j} \Delta y \Delta t,
\end{aligned} \tag{3.6}$$

where $\mathbf{F}_{i\pm\frac{1}{2},j}$ and $\mathbf{G}_{i,j\pm\frac{1}{2}}$ represent the *numerical fluxes*, that are an approximate estimation of the physical flux vectors $\mathbf{F}$ and $\mathbf{G}$ through the cell sides l_s during a time step Δt.
Substituting (3.6) in (3.5), the fully discrete scheme for the updating of the average vector of conserved variables at the new time level t^{n+1} becomes [67]:

$$\mathbf{U}_{i,j}^{n+1} = \mathbf{U}_{i,j}^{n} - \frac{\Delta t}{\Delta x} \left[\mathbf{F}_{i+\frac{1}{2},j} - \mathbf{F}_{i-\frac{1}{2},j} \right] - \frac{\Delta t}{\Delta y} \left[\mathbf{G}_{i,j+\frac{1}{2}} - \mathbf{G}_{i,j-\frac{1}{2}} \right], \tag{3.7}$$

and the value $\mathbf{U}_{i,j}^{n+1}$ is completely determined once $\mathbf{F}_{i+\frac{1}{2},j}$ and $\mathbf{G}_{i,j+\frac{1}{2}}$ are specified.

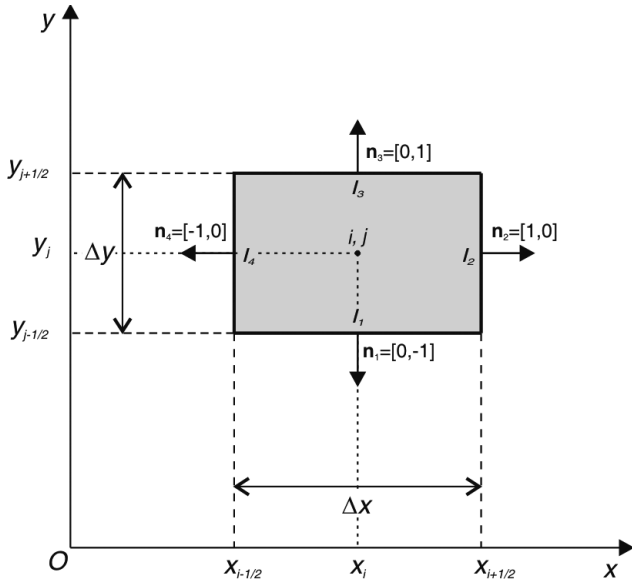

Figure 3.1. Cartesian control volume $I_{i,j}$.

Numerical fluxes have the form:

$$\begin{aligned}\mathbf{F}_{i+\frac{1}{2},j} &= \mathbf{F}_{i+\frac{1}{2},j}\left(\mathbf{U}_{i-k_L,j}^{n},\ldots,\mathbf{U}_{i+k_R,j}^{n}\right),\\ \mathbf{G}_{i,j+\frac{1}{2}} &= \mathbf{G}_{i,j+\frac{1}{2}}\left(\mathbf{U}_{i,j-k_L}^{n},\ldots,\mathbf{U}_{i,j+k_R}^{n}\right),\end{aligned} \tag{3.8}$$

with k_L and k_R depending on the algorithm chosen for the flux estimation; if a numerical scheme is *explicit* all the flux arguments are evaluated at the current time level n [67, 44].
Numerical methods based on formula (3.7) are *conservative*, i.e. at the new time level the solution on the cell $I_{i,j}$ varies only due to the fluxes through the cell boundaries. Conservative methods enjoy the so-called *telescopic property* [34, 67], according to which the intercell flux $\mathbf{F}_{i+\frac{1}{2},j}$ for the updating of the

cell average $\mathbf{U}^n_{i,j}$ must be identical to the intercell flux $\mathbf{F}_{i-\frac{1}{2},j}$ for the updating of $\mathbf{U}^n_{i+1,j}$. The telescopic property holds also in the y direction. More in general, the discrete sum of $\mathbf{U}^n_{i,j}$ on the whole domain will vary only due to the fluxes through the end boundaries. The total mass within the computational domain will be preserved, or vary correctly provided that boundaries conditions are properly imposed.
Numerical fluxes must also satisfy the property of *consistency*: if all the arguments of the numerical fluxes (3.8) are equal to a constant value $\widehat{\mathbf{U}}$, then the value of the numerical fluxes at $\widehat{\mathbf{U}}$ must coincide with the value of the exact physical fluxes at $\widehat{\mathbf{U}}$, namely:

$$\begin{aligned}\mathbf{F}_{i+\frac{1}{2},j}\big(\widehat{\mathbf{U}},\dots,\widehat{\mathbf{U}}\big) &= \mathbf{F}\big(\widehat{\mathbf{U}}\big),\\ \mathbf{G}_{i,j+\frac{1}{2}}\big(\widehat{\mathbf{U}},\dots,\widehat{\mathbf{U}}\big) &= \mathbf{G}\big(\widehat{\mathbf{U}}\big).\end{aligned} \tag{3.9}$$

The use of conservative finite-volume methods based on the integral form of the governing equations is essential in computing discontinuous (*weak*) solutions to the conservation laws; this statement is proved by a set of theorems here briefly explained [34, 67, 44].
The fundamental theorem of Lax and Wendroff [42] established that if a consistent and conservative method is convergent, then it will converge to the weak solution of the conservation laws. Nevertheless, this theorem does not guarantee that convergence occurs. Since that weak solutions can be non-unique, an entropy condition must be satisfied. Harten [29] proved that if a conservative scheme is convergent and entropy satisfying, then it will converge to the physically meaningful solution. Hou and LeFloche [36] showed that if a method is not written in conservation form, then in the presence of a shock wave, the scheme, if convergent, will converge to the solution of a new conservation law with a source term.

3.2 WSDGM Scheme

3.2.1 Introduction

Two dimensional shallow water equations (SWE) are currently accepted to mathematically describe a wide variety of free surface flows under the effect

of gravity, such as dam-break waves, propagation of flood waves in rivers, flood plain inundations, etc. Because the analytical solutions available in the literature concern only a few simple situations [56, 61, 64, 58, 49, 39], the SWE needs to be numerically solved in order to deal with more general applications.
The irregular topography of the regions subject to flooding can strongly affect the flow dynamics, giving rise to the formation of hydraulic jumps, shocks and reflections; for this reason, in the numerical simulation of such phenomena an efficient treatment of the bed slope source term is necessary to obtain accurate results both in the case of steady and unsteady flows.
In engineering applications the necessity to handle wetting and drying moving boundaries is a challenge that researchers are also tackling [7, 9, 24, 16, 10, 12]. It is well known that small water depths near wet/dry interfaces can lead to numerical instabilities. In order to avoid these unphysical oscillations the simple procedure of drying cells in which water depth is smaller than a fixed tolerance [67] is not completely satisfying, because it induces a mass error that grows into not acceptable values in field-scale applications [17, 12, 52]. Another numerical difficulty is related to partially wet cells in which pressure and gravity forces are not exactly balanced in static conditions [33, 16].
In recent years a large amount of research has dealt with the application of finite volume Godunov-type methods for the numerical solution of SWE with source terms [66, 14, 25, 13, 81, 37, 43, 82, 74, 60]. In the *fractional step method* [67, 44] the complete equations are split into a homogeneous problem and an ODE system. Although simple, the procedure performs poorly if applied to SWE with geometric source terms, especially near the steady state [67, 44]. A more complex approach, which gives more satisfactory results, concerns the upwinding of the source terms, in a manner similar to that adopted for the construction of numerical fluxes for solving homogeneous conservation laws. Bermúdez & Vázquez-Cendón [14] applied this treatment to first order Roe's scheme and defined the fundamental notion of *C-property*, that is the capability of replicating the exact solution for the stationary flow problem. This upwinding approach was extended to a wide range of problems by Garcia-Navarro & Vázquez-Cendón [25], Bermúdez et al. [13] and Vázquez-Cendón [81]. Later Hubbard & García-Navarro [37] generalized this technique to a finite volume high order TVD version of Roe's scheme and to arbitrary polygonal meshes. In [43] LeVeque proposed the *quasi-steady state wave propagation algorithm* in which, avoiding any splitting, the source term is incorporated into the wave propagation algorithm; a Riemann problem is introduced at the center of each cell whose flux difference exactly cancels the source term. According to the author, this method is effective when the solution is near the steady state, but

it presents difficulties in the case of transcritical steady flows with shocks. In Zhou et al. [82] the *Surface Gradient Method* was introduced. In order to evaluate more accurate numerical fluxes in the presence of non-flat topography, the intercell water depth was computed starting from the MUSCL reconstruction of the water surface level. Together with a centered discretization of the bottom slope source term, the scheme is capable of maintaining the static condition on a Cartesian grid. This approach is very attractive for its simplicity, but, near wet/dry fronts on non-flat topography, the SGM reconstruction can lead to very small water depths (even negative) that need to be modified in order to avoid unphysical results. A more robust behaviour in the front tracking can be obtained with the conventional DGM (*Depth Gradient Method*) approach which evaluates intercell water depths starting from the extrapolation of the same conserved variable; on the other hand, this method does not maintain the static condition if a centered discretization is used for the bed slope source term. In the recent work of Valiani & Begnudelli [74] the bed slope source term is expressed as the divergence of a suitable matrix related to the static force due to the bottom slope; moreover a SGM variable reconstruction is performed to compute water depth at the cell boundaries. This technique is simple and allows the preservation of the condition of quiescent water on a totally wet domain on irregular grids too.
A *Weighted Surface-Depth Gradient Method* (WSDGM) is here proposed with the aim of combining the good capabilities of SGM and DGM approaches and avoiding their drawbacks. In the framework of a MUSCL scheme [67], the proposed algorithm computes water depths at the cell boundaries through a weighted average of the extrapolated values deriving from DGM and SGM reconstructions: in this way the scheme is capable of maintaining the static condition on non-flat topographies and performing a robust tracking of wet/dry fronts.
In cells in which the computed water depth is lower than a small threshold, a flux correction is applied in order to drastically reduce the mass error.

3.2.2 The Updating Algorithm

WSDGM solves the inhomogeneous initial value problem (IVP):

$$\begin{cases} \dfrac{d}{dt}\displaystyle\int_{y_{j-\frac{1}{2}}}^{y_{j+\frac{1}{2}}}\int_{x_{i-\frac{1}{2}}}^{x_{i+\frac{1}{2}}} \mathbf{U}\,dx\,dy + \sum_{s=1}^{4}\mathcal{F}_s = \int_{y_{j-\frac{1}{2}}}^{y_{j+\frac{1}{2}}}\int_{x_{i-\frac{1}{2}}}^{x_{i+\frac{1}{2}}} \mathbf{S}\left(\mathbf{U}\right)\,dx\,dy \\ \text{IC: } \mathbf{U}\left(x,y,t^n\right) = \mathbf{U}^n, \end{cases} \tag{3.10}$$

where 2D SWE in integral form, including the geometric and resistance source terms, are coupled with the initial state $\mathbf{U}^n$, estimated at the generic time level t^n.
In order to obtain the solution at the updated time level t^{n+1}, different schemes can be applied.
The time-splitted *Fractional Step* (also known as *Godunov Splitting*) algorithm separates the full problem (3.10) in a succession of two IVPs [67], the first:

$$\begin{cases} \dfrac{d}{dt}\displaystyle\int_{y_{j-\frac{1}{2}}}^{y_{j+\frac{1}{2}}}\int_{x_{i-\frac{1}{2}}}^{x_{i+\frac{1}{2}}} \mathbf{U}\,dx\,dy + \sum_{s=1}^{4}\mathcal{F}_s = \int_{y_{j-\frac{1}{2}}}^{y_{j+\frac{1}{2}}}\int_{x_{i-\frac{1}{2}}}^{x_{i+\frac{1}{2}}} \mathbf{S}_0\,dx\,dy \\ \text{IC: } \mathbf{U}^n \end{cases} \overset{\Delta t}{\Rightarrow} \mathbf{U}^* \tag{3.11}$$

and the second, that is reduced to an ordinary different equation (ODE) problem:

$$\begin{cases} \dfrac{d}{dt}\displaystyle\int_{y_{j-\frac{1}{2}}}^{y_{j+\frac{1}{2}}}\int_{x_{i-\frac{1}{2}}}^{x_{i+\frac{1}{2}}} \mathbf{U}\,dx\,dy = \int_{y_{j-\frac{1}{2}}}^{y_{j+\frac{1}{2}}}\int_{x_{i-\frac{1}{2}}}^{x_{i+\frac{1}{2}}} \mathbf{S}_f\,dx\,dy \\ \text{IC: } \mathbf{U}^* \end{cases} \overset{\Delta t}{\Rightarrow} \mathbf{U}^{n+1}. \tag{3.12}$$

This method joins the great advantage of simplicity with the possibility to choose the best scheme for the solution of sub-problems (3.11) and (3.12); in particular a high-resolution method will be adopted in the solution of (3.11), since it would be very difficult to derive a similar approach that incorporates also the source terms, while an appropriate ODE solver will be applied to (3.12).
In the classical version of this method [67, 44], the first step solves the homogeneous SWE, while the second one accounts for both forcing effects due to

bottom and friction slopes: it is wellknown [67, 44] that such a scheme presents unsatisfactory results when applied to shallow water flows involving geometric source terms, especially near the steady state. As it will be explained in detail in the following sections, the inclusion of the bottom slope source term conveniently discretized in (3.11) allows the correct modeling of the static condition of water at rest [82].
In the finite-volume framework, the *Fractional Step* method can be rewritten as:

$$\mathbf{U}^{n+1} = \mathcal{S}^{(\Delta t)}\mathcal{A}^{(\Delta t)}\mathbf{U}^{n}, \tag{3.13}$$

where the operators $\mathcal{A}(\mathbf{U})$ and $\mathcal{S}(\mathbf{U})$ have expression:

$$\begin{aligned} \mathcal{A}: \quad & \mathbf{U}^{*}_{i,j} = \mathbf{U}^{n}_{i,j} - \frac{\Delta t}{\Delta x}\left[\mathbf{F}_{i+\frac{1}{2},j} - \mathbf{F}_{i-\frac{1}{2},j}\right] - \frac{\Delta t}{\Delta y}\left[\mathbf{G}_{i,j+\frac{1}{2}} - \mathbf{G}_{i,j-\frac{1}{2}}\right] + \Delta t\overline{\mathbf{S}}_{0\,i,j} \\ \mathcal{S}: \quad & \mathbf{U}^{n+1}_{i,j} = \mathbf{U}^{*}_{i,j} + \Delta t\,\mathbf{S}_{f\,i,j}. \end{aligned} \tag{3.14}$$

In (3.14) the *numerical* source terms

$$\overline{\mathbf{S}}_{0\,i,j} \approx \frac{1}{|I_{i,j}|}\frac{1}{\Delta t}\int_{t^n}^{t^{n+1}}\int_{y_{j-\frac{1}{2}}}^{y_{j+\frac{1}{2}}}\int_{x_{i-\frac{1}{2}}}^{x_{i+\frac{1}{2}}} \mathbf{S}_0\big(\mathbf{U}(x,y,t)\big)\,dx\,dy\,dt, \tag{3.15}$$

$$\mathbf{S}_{f\,i,j} \approx \frac{1}{|I_{i,j}|}\frac{1}{\Delta t}\int_{t^n}^{t^{n+1}}\int_{y_{j-\frac{1}{2}}}^{y_{j+\frac{1}{2}}}\int_{x_{i-\frac{1}{2}}}^{x_{i+\frac{1}{2}}} \mathbf{S}_f\big(\mathbf{U}(x,y,t)\big)\,dx\,dy\,dt \tag{3.16}$$

represent a suitable estimate of $\mathbf{S}_0$ and $\mathbf{S}_f$ on the grid element $I_{i,j}$ over a time step Δt.
Introducing a *splitting error* of order $\mathcal{O}(\Delta t)$ [44], the Fractional Step algorithm is first order accurate in time, even though $\mathcal{S}$ and $\mathcal{A}$ are more than first order accurate.
On the other hand, second order of accuracy in time can be achieved applying

the *Strang Splitting* scheme [62, 67, 44]:

$$\mathbf{U}^{n+1} = \mathcal{S}^{\left(\frac{1}{2}\Delta t\right)}\mathcal{A}^{(\Delta t)}\mathcal{S}^{\left(\frac{1}{2}\Delta t\right)}\mathbf{U}^{n}, \tag{3.17}$$

under the assumption that each subproblem is solved with a method of at least the same order of accuracy.
In WSDGM the possibility to choose between (3.13) and (3.18) is allowed.

Stability condition

Every explicit finite-volume method must satisfy a *necessary* condition which guarantees the stability and the convergence to the exact solution as the grid is refined. In other words, the method must be used in such a way that information has a chance to propagate at the correct physical speed.
Such constraint is represented by the Courant-Friedrichs-Lewy condition [22, 23], which formally states that a numerical method can be convergent only if its numerical domain of dependence contains the true domain of dependence of the PDEs, at least in the limit as Δt, Δx and Δy tend to zero.
Following [66], the 2D CFL stability criterion that controls the time step Δt at each time level, is given by:

$$0 < \mathrm{Cr}_x + \mathrm{Cr}_y \leq 1, \tag{3.18}$$

where Cr_x and Cr_y are the Courant numbers in x and y directions respectively. This assumption leads to:

$$\Delta t = \mathrm{Cr}\left[\max\left(\frac{|u_{i,j}| + \sqrt{gh_{i,j}}}{\Delta x} + \frac{|v_{i,j}| + \sqrt{gh_{i,j}}}{\Delta y}\right)\right]^{-1}, \tag{3.19}$$

where $0 < \mathrm{Cr} \leq 1$.

3.2.3 Treatment of Friction Source Term

Among several ODE solvers suitable for the solution of problem (3.12), the semi-implicit, second order *trapezoidal* method was adopted [44, 18].

Following this approach, the numerical friction source term can be defined as:

$$\mathbf{S}_{f\,i,j} = \beta \mathbf{S}_f \left(\mathbf{U}_{i,j}^{n+1}\right) + (1-\beta)\,\mathbf{S}_f \left(\mathbf{U}_{i,j}^{n}\right), \tag{3.20}$$

with β representing the rate of implicity.
Assuming $\beta = 1/2$, the discretized form of problem (3.12) becomes:

$$\mathbf{U}_{i,j}^{n+1} = \mathbf{U}_{i,j}^{*} + \frac{\Delta t}{2}\left[\mathbf{S}_f \left(\mathbf{U}_{i,j}^{*}\right) + \mathbf{S}_f \left(\mathbf{U}_{i,j}^{n+1}\right)\right], \tag{3.21}$$

from which, after some algebraic manipulations:

$$\mathbf{U}_{i,j}^{n+1} = \mathbf{U}_{i,j}^{*} + \Delta t \left[\mathbf{I} - \frac{\Delta t}{2}\mathbf{Q}_f \left(\mathbf{U}_{i,j}^{*}\right)\right]^{-1} \mathbf{S}_f \left(\mathbf{U}_{i,j}^{*}\right), \tag{3.22}$$

where $\mathbf{I}$ is the identity matrix of order 3 and $\mathbf{Q}_f$ is the Jacobian matrix of $\mathbf{S}_f(\mathbf{U})$, having form:

$$\mathbf{S}_f(\mathbf{U}) = \begin{bmatrix} 0 & 0 & 0 \\ \frac{7}{3}gS_{fx} & -gS_{fx}\left(\frac{1}{u} + \frac{u}{u^2+v^2}\right) & -gS_{fx}\frac{v}{u^2+v^2} \\ \frac{7}{3}gS_{fy} & -gS_{fy}\frac{u}{u^2+v^2} & -gS_{fy}\left(\frac{1}{v} + \frac{v}{u^2+v^2}\right) \end{bmatrix}. \tag{3.23}$$

Despite this is an implicit method, the equations obtained in the $I_{i,j}$ cell are decoupled from the equations in every other cell, so they can be solved quite easily. This technique couples the simplicity of implementation typical of explicit schemes with the stability typical of implicit ones.

3.2.4 The High-Resolution Method

Theoretical background

The importance of dealing with numerical methods of accuracy grater than one is wellknown [35, 66, 44], because first-order methods are sometimes too inaccurate to be of physical interest. On the other hand, second-order accurate schemes, which give much accuracy on smooth solution than first-order ones, fail in the vicinity of high gradients of the solution where spurious oscillations are generated, due to the dispersive nature of these methods [44].
In 1959 Godunov [27] showed that all monotone linear schemes can be at most of first-order accuracy, hence any linear procedure to limit gradients in second order schemes will be unsatisfactory. To around this difficulty non-linear correction factors, called *limiters* [77, 15], must be introduced .
Applying some form of limiters, *high resolution* methods combine the best features of first-order monotone and second-order schemes, maintaining second-order of accuracy in the smooth part of the solution and producing solutions less accurate but free of spurious oscillations near high gradients. Moreover such schemes perform a high resolution of the discontinuity, that is the number of mesh points in the transition zone containing the numerical wave is narrow if compared with that of first-order of accuracy.
Since monotonicity can be fulfilled only by first-order schemes, high-resolution ones have to satisfy a weaker condition that guarantees a non-oscillatory behavior of the solution. This property is provided by the concept of *Total Variation Diminishing* (TVD), introduced by Harten [29, 30].
The *Total Variation* of a grid function $\mathbf{U}$ defined as

$$TV\left(\mathbf{U}\right) = \sum_{i=-\infty}^{\infty} \left|\mathbf{U}_i - \mathbf{U}_{i+1}\right| \tag{3.24}$$

measures the oscillations in the solution. If a method is oscillatory, the total variation of $\mathbf{U}^n$ will increase with time. When the total variation does *not increase* in time a numerical scheme is said to be TVD, i.e. for any set of data $\mathbf{U}^n$ the computed values $\mathbf{U}^{n+1}$ satisfy

$$TV\left(\mathbf{U}^{n+1}\right) \leq TV\left(\mathbf{U}^n\right). \tag{3.25}$$

TVD methods are monotonicity preserving, namely monotone profiles are preserved during the time evolution of the discrete solution and overshoots will not be created. However, unlike monotonicity, TVD property does not ensure the satisfaction of the entropy condition [35]. A detailed analysis on the additional constraints to be imposed on a TVD scheme to be also entropy satisfying can be found in [53, 54].

WSDGM

In the following paragraphs the explicit, high-resolution, MUSCL-type numerical algorithm applied by WSDGM for the solution of problem (3.11) will be described.
In order to obtain second-order of accuracy in space and time, the conserved variables are first reconstructed at the cell interfaces according to WSDGM-MUSCL technique (Step I), which makes a blending between SGM and DGM reconstructions of water depth, and then evolved over $\Delta t/2$ (Step II). Numerical fluxes can be estimated as a function of the evolved extrapolated values, applying the centered FORCE method (Step IIIa) or the upwind approximate HLLC Riemann solver (Step IIIb).

Step I. The WSDGM-MUSCL reconstruction. According to the MUSCL (Monotone Upstream-Centered Scheme for Conservation Laws) approach [75, 79, 80, 35, 66, 67], the second order of accuracy in space is obtained reconstructing the solution at cell boundaries through a piecewise linear approximation. In order to avoid spurious overshoots in the solution and to ensure monotonicity, linear variations have to be limited with the introduction of a TVD constraint. Given $\mathbf{U}_i^n$ as the vector of the averaged conserved variables over the grid element $I_{i,j}$ at the current time level n, the extrapolated values in x and y directions

are given by:

$$
\begin{aligned}
\mathbf{U}^{L}_{i+\frac{1}{2},j} &= \mathbf{U}^{n}_{i,j} + \frac{1}{4}\Big[(1-k)\,\mathbf{\Phi}^{+}_{i-\frac{1}{2},j}\left(\mathbf{U}^{n}_{i,j} - \mathbf{U}^{n}_{i-1,j}\right) + \\
&\qquad (1+k)\,\mathbf{\Phi}^{-}_{i+\frac{1}{2},j}\left(\mathbf{U}^{n}_{i+1,j} - \mathbf{U}^{n}_{i,j}\right)\Big], \\
\mathbf{U}^{R}_{i-\frac{1}{2},j} &= \mathbf{U}^{n}_{i,j} - \frac{1}{4}\Big[(1+k)\,\mathbf{\Phi}^{+}_{i-\frac{1}{2},j}\left(\mathbf{U}^{n}_{i,j} - \mathbf{U}^{n}_{i-1,j}\right) + \\
&\qquad (1-k)\,\mathbf{\Phi}^{-}_{i+\frac{1}{2},j}\left(\mathbf{U}^{n}_{i+1,j} - \mathbf{U}^{n}_{i,j}\right)\Big], \\
\mathbf{U}^{L}_{i,j+\frac{1}{2}} &= \mathbf{U}^{n}_{i,j} + \frac{1}{4}\Big[(1-k)\,\mathbf{\Phi}^{+}_{i,j-\frac{1}{2}}\left(\mathbf{U}^{n}_{i,j} - \mathbf{U}^{n}_{i,j-1}\right) + \\
&\qquad (1+k)\,\mathbf{\Phi}^{-}_{i,j+\frac{1}{2}}\left(\mathbf{U}^{n}_{i,j+1} - \mathbf{U}^{n}_{i,j}\right)\Big], \\
\mathbf{U}^{R}_{i,j-\frac{1}{2}} &= \mathbf{U}^{n}_{i,j} - \frac{1}{4}\Big[(1+k)\,\mathbf{\Phi}^{+}_{i,j-\frac{1}{2}}\left(\mathbf{U}^{n}_{i,j} - \mathbf{U}^{n}_{i,j-1}\right) + \\
&\qquad (1-k)\,\mathbf{\Phi}^{-}_{i,j+\frac{1}{2}}\left(\mathbf{U}^{n}_{i,j+1} - \mathbf{U}^{n}_{i,j}\right)\Big],
\end{aligned}
\tag{3.26}
$$

where the superscripts L and R refer to the left and right sides at the considered boundary. The interface values computed in Eq.(3.26) result from a combination of backward and forward extrapolations. If the parameter k is set equal to ± 1, a one-sided extrapolation is performed; in Fig.3.2 an example of a linear one-sided reconstruction of the generic variable U along the space direction x is shown.

In Eq.(3.26) the diagonal matrices $\mathbf{\Phi}^{\pm}$ represent the *slope limiters* [63, 35, 66, 44] which assure the TVD property; these matrices are a function of the ratios $\mathbf{r}^{\pm}$ of the consecutive variations:

$$
\begin{aligned}
\mathbf{\Phi}^{+}_{i-\frac{1}{2},j} &= \mathbf{\Phi}\left(\mathbf{r}^{+}_{i-\frac{1}{2},j}\right), \quad \mathbf{\Phi}^{-}_{i+\frac{1}{2},j} = \mathbf{\Phi}\left(\mathbf{r}^{-}_{i+\frac{1}{2},j}\right), \\
\mathbf{\Phi}^{+}_{i,j-\frac{1}{2}} &= \mathbf{\Phi}\left(\mathbf{r}^{+}_{i,j-\frac{1}{2}}\right), \quad \mathbf{\Phi}^{-}_{i,j+\frac{1}{2}} = \mathbf{\Phi}\left(\mathbf{r}^{-}_{i,j+\frac{1}{2}}\right),
\end{aligned}
\tag{3.27}
$$

with vectors $\mathbf{r}^{\pm}$ defined as:

$$
\begin{aligned}
\mathbf{r}^{+}_{i-\frac{1}{2},j} &= \frac{\mathbf{U}^{n}_{i+1,j} - \mathbf{U}^{n}_{i,j}}{\mathbf{U}^{n}_{i,j} - \mathbf{U}^{n}_{i-1,j}}, \quad \mathbf{r}^{-}_{i+\frac{1}{2},j} = \frac{\mathbf{U}^{n}_{i,j} - \mathbf{U}^{n}_{i-1,j}}{\mathbf{U}^{n}_{i+1,j} - \mathbf{U}^{n}_{i,j}}, \\
\mathbf{r}^{+}_{i,j-\frac{1}{2}} &= \frac{\mathbf{U}^{n}_{i,j+1} - \mathbf{U}^{n}_{i,j}}{\mathbf{U}^{n}_{i,j} - \mathbf{U}^{n}_{i,j-1}}, \quad \mathbf{r}^{-}_{i,j+\frac{1}{2}} = \frac{\mathbf{U}^{n}_{i,j} - \mathbf{U}^{n}_{i,j-1}}{\mathbf{U}^{n}_{i,j+1} - \mathbf{U}^{n}_{i,j}}.
\end{aligned}
\tag{3.28}
$$

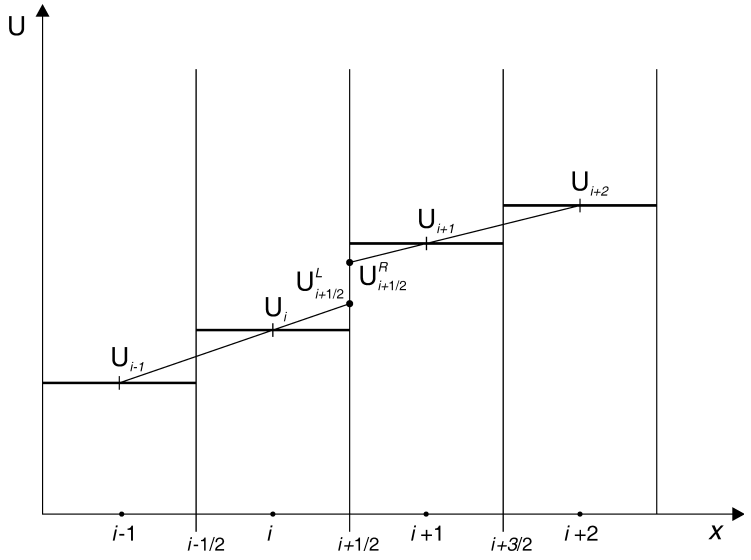

Figure 3.2. Linear one-sided MUSCL extrapolation along x-axis.

Among several forms of limiter functions reported in the literature [35, 66, 67, 44], in WSDGM the possibility of choosing between the VanLeer [78] or VanAlbada [76] limiter is allowed.
Such functions, given in scalar form, have expression:

$$\begin{aligned}
&\text{VanLeer Limiter:} \quad \Phi(r) = \begin{cases} \dfrac{r+|r|}{1+r} & \text{if} \quad r > 0 \\ 0 & \text{if} \quad r \leq 0; \end{cases} \\
&\text{VanAlbada Limiter:} \quad \Phi(r) = \begin{cases} \dfrac{r^2+r}{1+r^2} & \text{if} \quad r > 0 \\ 0 & \text{if} \quad r \leq 0. \end{cases}
\end{aligned} \tag{3.29}$$

Referring to the MUSCL approximation (3.26), the reconstruction of water depth at the cell boundary is performed starting from the extrapolation of the same conserved variable. Following the nomenclature proposed in the paper by Zhou et al. [82], this approach can be named with the acronym DGM (*Depth Gradient Method*).
Setting $k = -1$ in (3.26), DGM boundary water depths result:

$$\begin{aligned}
h^{L,\,DGM}_{i+\frac{1}{2},j} &= h^n_{i,j} + \frac{1}{2}\Phi^+_{i-\frac{1}{2},j}\left(h^n_{i,j} - h^n_{i-1,j}\right) \\
h^{R,\,DGM}_{i-\frac{1}{2},j} &= h^n_{i,j} - \frac{1}{2}\Phi^-_{i+\frac{1}{2},j}\left(h^n_{i+1,j} - h^n_{i,j}\right) \\
h^{L,\,DGM}_{i,j+\frac{1}{2}} &= h^n_{i,j} + \frac{1}{2}\Phi^+_{i,j-\frac{1}{2}}\left(h^n_{i,j} - h^n_{i,j-1}\right) \\
h^{R,\,DGM}_{i,j-\frac{1}{2}} &= h^n_{i,j} - \frac{1}{2}\Phi^-_{i,j+\frac{1}{2}}\left(h^n_{i,j+1} - h^n_{i,j}\right).
\end{aligned} \tag{3.30}$$

However, water depth at cell interfaces is influenced by the bed topography together with the variation in time of the free surface level. According to Zhou et al. [82], this is the reason why a DGM can fail to reproduce the real variation in water depth when the bed slope source terms are included. In particular, if a centered discretization is used for the bed slope term, this approach can not replicate the exact solution of the static flow problem $\eta(x,y,t) = h(x,y,t) + z(x,y) = \overline{\eta},\ u(x,y,t) = 0,\ v(x,y,t) = 0$, i.e. it does not satisfy the exact *C-property* [14].
In their work Zhou et al. [82] proposed the *Surface Gradient Method* (SGM),

which can be incorporated into any Godunov-type method requiring data reconstruction. In order to provide accurate values of the conservative variables at cell inrefaces, the water depth reconstruction is performed extrapolating the free surface level and then subtracting the intercell bed elevation:

$$\begin{aligned}
\eta^L_{i+\frac{1}{2},j} &= \eta^n_{i,j} + \frac{1}{2}\Phi^+_{i-\frac{1}{2},j}\left(\eta^n_{i,j} - \eta^n_{i-1,j}\right), \quad h^{L,SGM}_{i+\frac{1}{2},j} = \eta^L_{i+\frac{1}{2},j} - b_{i+\frac{1}{2},j} \\
\eta^R_{i-\frac{1}{2},j} &= \eta^n_{i,j} - \frac{1}{2}\Phi^-_{i+\frac{1}{2},j}\left(\eta^n_{i+1,j} - \eta^n_{i,j}\right), \quad h^{R,SGM}_{i-\frac{1}{2},j} = \eta^R_{i-\frac{1}{2},j} - b_{i-\frac{1}{2},j} \\
\eta^L_{i,j+\frac{1}{2}} &= \eta^n_{i,j} + \frac{1}{2}\Phi^+_{i,j-\frac{1}{2}}\left(\eta^n_{i,j} - \eta^n_{i,j-1}\right), \quad h^{L,SGM}_{i,j+\frac{1}{2}} = \eta^L_{i,j+\frac{1}{2}} - b_{i,j+\frac{1}{2}} \\
\eta^R_{i,j-\frac{1}{2}} &= \eta^n_{i,j} - \frac{1}{2}\Phi^-_{i,j+\frac{1}{2}}\left(\eta^n_{i,j+1} - \eta^n_{i,j}\right), \quad h^{R,SGM}_{i,j-\frac{1}{2}} = \eta^R_{i,j-\frac{1}{2}} - b_{i,j-\frac{1}{2}}.
\end{aligned} \tag{3.31}$$

According to a linear variation in the bed profile, the bottom elevation at the cell interface is evaluated as:

$$\begin{aligned}
b_{i+\frac{1}{2},j} &= \frac{b_{i,j} + b_{i+1,j}}{2}, \quad b_{i-\frac{1}{2},j} = \frac{b_{i-1,j} + b_{i,j}}{2} \\
b_{i,j+\frac{1}{2}} &= \frac{b_{i,j} + b_{i,j+1}}{2}, \quad b_{i,j-\frac{1}{2}} = \frac{b_{i,j-1} + b_{i,j}}{2}.
\end{aligned} \tag{3.32}$$

If an unsplit centered discretization of the bottom slope source term is performed, the SGM reconstruction allows the satisfaction of the exact *C-property* on a Cartesian grid [82]. In the case of a flat bottom SGM and DGM approaches are equivalent.
In the last years the research group of Parma University developed two different MUSCL schemes: the first performs a DGM variable reconstruction and a splitting of the source terms [3, 4], while the second adopts the SGM data reconstruction [3, 5]. Testing the codes on a set of reference problems [64, 38, 49, 45, 1] and case studies, it was verified that SGM reconstructions are preferable for those applications in which small water level gradients occur in the presence of high water depth gradients, as, for example, in the case of a subcritical steady flow over a bump, as it will be shown in Section 4.1. The application of SGM to field-scale cases often leads to unsatisfactory results in the treatment of the wetting and drying fronts, especially on highly irregular topographies. In fact, at wet/dry interfaces on a non-flat bottom, SGM reconstructions can give rise to very small water depths (even negative) and, as a consequence, to unphysical

results.
On the contrary, the DGM code is robust and stable when high water level gradients occur together with small water depth gradients, as, for example, in the case of a supercritical steady flow over a bump (Section 4.1). Introducing a threshold value h_ϵ to avoid instabilities in the presence of very small depths [67], the scheme is also capable of tracking the motion of wetting and drying fronts.
In order to overcome the limitations of SGM and DGM and to retain the best of both, the proposed WSDGM estimates the numerical water depth at cell interfaces through a weighted average of the boundary extrapolated values derived from DGM and SGM reconstructions:

$$\begin{aligned}
h^L_{i+\frac{1}{2},j} &= \vartheta_{i,j} h^{L,\,DGM}_{i+\frac{1}{2},j} + (1-\vartheta_{i,j})\, h^{L,\,SGM}_{i+\frac{1}{2},j} \\
h^R_{i-\frac{1}{2},j} &= \vartheta_{i,j} h^{R,\,DGM}_{i-\frac{1}{2},j} + (1-\vartheta_{i,j})\, h^{R,\,SGM}_{i-\frac{1}{2},j} \\
h^L_{i,j+\frac{1}{2}} &= \vartheta_{i,j} h^{L,\,DGM}_{i,j+\frac{1}{2}} + (1-\vartheta_{i,j})\, h^{L,\,SGM}_{i,j+\frac{1}{2}} \\
h^R_{i,j-\frac{1}{2}} &= \vartheta_{i,j} h^{R,\,DGM}_{i,j-\frac{1}{2}} + (1-\vartheta_{i,j})\, h^{R,\,SGM}_{i,j-\frac{1}{2}},
\end{aligned} \tag{3.33}$$

in which $\vartheta_{i,\,j}$ is a weighting parameter.
The form of $\vartheta_{i,\,j}$ should allow a smooth transition between a fully SGM extrapolation where water is at rest (Fr = 0) and an essentially DGM extrapolation at wet/dry moving fronts. Both previous requirements can be satisfied by adopting the Froude number as the control parameter.
Although any function with the features mentioned above can be used, WSDGM adopts a simple trigonometric expression for the weighting function (Fig.3.3):

$$\vartheta_{i,\,j} = \begin{cases} \dfrac{1}{2}\left[1 - \cos\left(\dfrac{\pi \mathrm{Fr}_{i,\,j}}{\mathrm{Fr}_{\mathrm{lim}}}\right)\right] & 0 \le \mathrm{Fr}_{i,\,j} \le \mathrm{Fr}_{\mathrm{lim}} \\ 1 & \mathrm{Fr}_{i,\,j} > \mathrm{Fr}_{\mathrm{lim}} \end{cases} \tag{3.34}$$

where $\mathrm{Fr}_{\mathrm{lim}}$ is an upper limit beyond which a pure DGM reconstruction is performed.
Since a shock wave cannot be adjacent to a region of dry bed [67], water depths must tend gradually to zero and Fr to infinite at wet/dry interfaces. However, in a finite volume framework, Fr numbers remain finite also at the shoreline: the choice of $\mathrm{Fr}_{\mathrm{lim}}$ needs to guarantee an essentially DGM-type behavior near

wet/dry moving fronts.

In order to rigorously satisfy the *C-property* and to prevent the well-known in-

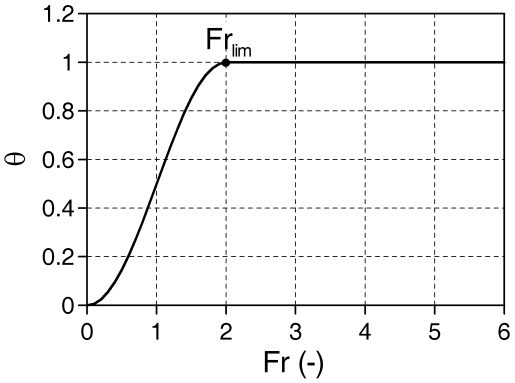

Figure 3.3. Behaviour of the function $\vartheta\,(\mathrm{Fr})$ in the particular case of $\mathrm{Fr}_{\mathrm{lim}} = 2$.

stabilities [7, 9, 24, 10] that arise at the shoreline when a fixed mesh is adopted, a special treatment is performed at wet-dry interfaces. If the water surface in the $(i,\, j)$-cell is lower than the bed elevation of the adjacent dry cell, the intercell bed elevation is set at the level of the extrapolated water surface and, as a consequence, the reconstructed water depth is zero [33, 6]. The centered estimate of the intercell bed elevation is restored when the shoreline no longer involves the cell.

Step II. Evolution of the extrapolated values. The boundary-extrapolated variables are evolved over $\Delta t/2$ to achieve second-order of accuracy in time:

$$
\begin{aligned}
\overline{\mathbf{U}}^{L}_{i+\frac{1}{2},j} &= \mathbf{U}^{L}_{i+\frac{1}{2},j} - \frac{\Delta t}{2\Delta x}\left[\mathbf{F}\left(\mathbf{U}^{L}_{i+\frac{1}{2},j}\right) - \mathbf{F}\left(\mathbf{U}^{R}_{i-\frac{1}{2},j}\right)\right] + \\
&\quad - \frac{\Delta t}{2\Delta y}\left[\mathbf{G}\left(\mathbf{U}^{L}_{i,j+\frac{1}{2}}\right) - \mathbf{G}\left(\mathbf{U}^{R}_{i,j-\frac{1}{2}}\right)\right] + \frac{\Delta t}{2}\mathbf{S}_{0\,i,j} \\
\overline{\mathbf{U}}^{R}_{i-\frac{1}{2},j} &= \mathbf{U}^{R}_{i-\frac{1}{2},j} - \frac{\Delta t}{2\Delta x}\left[\mathbf{F}\left(\mathbf{U}^{L}_{i+\frac{1}{2},j}\right) - \mathbf{F}\left(\mathbf{U}^{R}_{i-\frac{1}{2},j}\right)\right] + \\
&\quad - \frac{\Delta t}{2\Delta y}\left[\mathbf{G}\left(\mathbf{U}^{L}_{i,j+\frac{1}{2}}\right) - \mathbf{G}\left(\mathbf{U}^{R}_{i,j-\frac{1}{2}}\right)\right] + \frac{\Delta t}{2}\mathbf{S}_{0\,i,j},
\end{aligned}
\tag{3.35}
$$

$$
\begin{aligned}
\overline{\mathbf{U}}^{L}_{i,j+\frac{1}{2}} &= \mathbf{U}^{L}_{i,j+\frac{1}{2}} - \frac{\Delta t}{2\Delta x}\left[\mathbf{F}\left(\mathbf{U}^{L}_{i+\frac{1}{2},j}\right) - \mathbf{F}\left(\mathbf{U}^{R}_{i-\frac{1}{2},j}\right)\right] + \\
&\quad - \frac{\Delta t}{2\Delta y}\left[\mathbf{G}\left(\mathbf{U}^{L}_{i,j+\frac{1}{2}}\right) - \mathbf{G}\left(\mathbf{U}^{R}_{i,j-\frac{1}{2}}\right)\right] + \frac{\Delta t}{2}\mathbf{S}_{0\,i,j} \\
\overline{\mathbf{U}}^{R}_{i,j-\frac{1}{2}} &= \mathbf{U}^{R}_{i,\,j-\frac{1}{2}} - \frac{\Delta t}{2\Delta x}\left[\mathbf{F}\left(\mathbf{U}^{L}_{i+\frac{1}{2},j}\right) - \mathbf{F}\left(\mathbf{U}^{R}_{i-\frac{1}{2},j}\right)\right] + \\
&\quad - \frac{\Delta t}{2\Delta y}\left[\mathbf{G}\left(\mathbf{U}^{L}_{i,j+\frac{1}{2}}\right) - \mathbf{G}\left(\mathbf{U}^{R}_{i,j-\frac{1}{2}}\right)\right] + \frac{\Delta t}{2}\mathbf{S}_{0\,i,j}.
\end{aligned}
$$

In order to satisfy the *C-property*, the contribution of bed slope source term should be included in this step and a centered discretization needs to be applied:

$$
\mathbf{S}_{0\,i,j} = \begin{bmatrix} 0 \\ -g\,\dfrac{h^{L}_{i+\frac{1}{2},j} + h^{R}_{i-\frac{1}{2},j}}{2}\,\dfrac{b_{i+\frac{1}{2},j} - b_{i-\frac{1}{2},j}}{\Delta x} \\ -g\,\dfrac{h^{L}_{i,j+\frac{1}{2}} + h^{R}_{i,j-\frac{1}{2}}}{2}\,\dfrac{b_{i,j+\frac{1}{2}} - b_{i,j-\frac{1}{2}}}{\Delta x} \end{bmatrix}. \tag{3.36}
$$

Step IIIa. Intercell numerical fluxes: the FORCE scheme. According to the second-order Slope LImiter Centered (SLIC) schemes proposed by Toro and Billet [68], in a MUSCL-type method numerical fluxes can be computed applying low-order techniques, as the Godunov first-order centered, the Lax Friederichs and the FORCE schemes [66, 67]. The TVD property is assured

from limiting the slopes in the data reconstruction step.
Instead of solving the Riemann problem with data $\left(\overline{\mathbf{U}}^L_{i+\frac{1}{2},j}, \overline{\mathbf{U}}^R_{i+\frac{1}{2},j}\right)$, low-order schemes compute fluxes with data arguments $\left(\overline{\mathbf{U}}^L_{i+\frac{1}{2},j}, \overline{\mathbf{U}}^R_{i+\frac{1}{2},j}\right)$; in this way any dependence on the wave direction is avoided.
Among the possible choices, in WSDGM the FORCE flux [65, 66, 68, 67] is adopted:

$$\begin{aligned}
\mathbf{F}^{force}_{i+\frac{1}{2},j} &= \mathbf{F}^{force}_{i+\frac{1}{2},j}\left(\overline{\mathbf{U}}^L_{i+\frac{1}{2},j}, \overline{\mathbf{U}}^R_{i+\frac{1}{2},j}\right) = \\
&= \frac{1}{2}\left[\mathbf{F}^{LF}_{i+\frac{1}{2},j}\left(\overline{\mathbf{U}}^L_{i+\frac{1}{2},j}, \overline{\mathbf{U}}^R_{i+\frac{1}{2},j}\right) + \mathbf{F}^{RI}_{i+\frac{1}{2},j}\left(\overline{\mathbf{U}}^L_{i+\frac{1}{2},j}, \overline{\mathbf{U}}^R_{i+\frac{1}{2},j}\right)\right], \\
\mathbf{G}^{force}_{i,j+\frac{1}{2}} &= \mathbf{G}^{force}_{i,j+\frac{1}{2}}\left(\overline{\mathbf{U}}^L_{i,j+\frac{1}{2}}, \overline{\mathbf{U}}^R_{i,j+\frac{1}{2}}\right) = \\
&= \frac{1}{2}\left[\mathbf{G}^{LF}_{i,j+\frac{1}{2}}\left(\overline{\mathbf{U}}^L_{i,j+\frac{1}{2}}, \overline{\mathbf{U}}^R_{i,j+\frac{1}{2}}\right) + \mathbf{G}^{RI}_{i,j+\frac{1}{2}}\left(\overline{\mathbf{U}}^L_{i,j+\frac{1}{2}}, \overline{\mathbf{U}}^R_{i,j+\frac{1}{2}}\right)\right].
\end{aligned} \tag{3.37}$$

This method performs an arithmetic average between the first-order centered flux of Lax-Friederichs $\mathbf{F}^{LF}_{i+\frac{1}{2},j}$ [41, 35, 66, 67, 44]:

$$\begin{aligned}
&\mathbf{F}^{LF}_{i+\frac{1}{2},j}\left(\overline{\mathbf{U}}^L_{i+\frac{1}{2},j}, \overline{\mathbf{U}}^R_{i+\frac{1}{2},j}\right) = \\
&= \frac{1}{2}\left[\mathbf{F}_{i+\frac{1}{2},j}\left(\overline{\mathbf{U}}^L_{i+\frac{1}{2},j}\right) + \mathbf{F}_{i+\frac{1}{2},j}\left(\overline{\mathbf{U}}^R_{i+\frac{1}{2},j}\right)\right] + \frac{1}{2}\frac{\Delta x}{\Delta t}\left(\overline{\mathbf{U}}^L_{i+\frac{1}{2},j} - \overline{\mathbf{U}}^R_{i+\frac{1}{2},j}\right), \\
&\mathbf{G}^{LF}_{i,j+\frac{1}{2}}\left(\overline{\mathbf{U}}^L_{i,j+\frac{1}{2}}, \overline{\mathbf{U}}^R_{i,j+\frac{1}{2}}\right) = \\
&= \frac{1}{2}\left[\mathbf{G}_{i,j+\frac{1}{2}}\left(\overline{\mathbf{U}}^L_{i,j+\frac{1}{2}}\right) + \mathbf{G}_{i,j+\frac{1}{2}}\left(\overline{\mathbf{U}}^R_{i,j+\frac{1}{2}}\right)\right] + \frac{1}{2}\frac{\Delta x}{\Delta t}\left(\overline{\mathbf{U}}^L_{i,j+\frac{1}{2}} - \overline{\mathbf{U}}^R_{i,j+\frac{1}{2}}\right)
\end{aligned} \tag{3.38}$$

and the second-order centered flux of Richtmeyer $\mathbf{F}^{RI}_{i+\frac{1}{2},j}$ (also known as two-step Lax-Wendroff flux) [55, 35, 66, 67, 44]:

$$\begin{aligned}
&\mathbf{F}^{RI}_{i+\frac{1}{2},j}\left(\overline{\mathbf{U}}^{L}_{i+\frac{1}{2},j},\overline{\mathbf{U}}^{R}_{i+\frac{1}{2},j}\right)=\mathbf{F}\left(\mathbf{U}^{RI}_{i+\frac{1}{2},j}\right),\\
&\mathbf{U}^{RI}_{i+\frac{1}{2},j}=\frac{1}{2}\left(\overline{\mathbf{U}}^{L}_{i+\frac{1}{2},j}+\overline{\mathbf{U}}^{R}_{i+\frac{1}{2},j}\right)+\frac{1}{2}\frac{\Delta x}{\Delta t}\left[\mathbf{F}\left(\overline{\mathbf{U}}^{L}_{i+\frac{1}{2},j}\right)-\mathbf{F}\left(\overline{\mathbf{U}}^{R}_{i+\frac{1}{2},j}\right)\right],\\
&\mathbf{G}^{RI}_{i,j+\frac{1}{2}}\left(\overline{\mathbf{U}}^{L}_{i,j+\frac{1}{2}},\overline{\mathbf{U}}^{R}_{i,j+\frac{1}{2}}\right)=\mathbf{G}\left(\mathbf{U}^{RI}_{i,j+\frac{1}{2}}\right),\\
&\mathbf{U}^{RI}_{i,j+\frac{1}{2}}=\frac{1}{2}\left(\overline{\mathbf{U}}^{L}_{i,j+\frac{1}{2}}+\overline{\mathbf{U}}^{R}_{i,j+\frac{1}{2}}\right)+\frac{1}{2}\frac{\Delta x}{\Delta t}\left[\mathbf{G}\left(\overline{\mathbf{U}}^{L}_{i,j+\frac{1}{2}}\right)-\mathbf{G}\left(\overline{\mathbf{U}}^{R}_{i,j+\frac{1}{2}}\right)\right].
\end{aligned}\tag{3.39}$$

Step IIIb. Intercell numerical fluxes: the HLLC Riemann solver. To compute numerical solutions by Godunov-type methods, approximate Riemann solvers can be adopted [67]. Applying the HLL Riemann solver of Harten, Lax and VanLeer [31] and the HLLC modification [73, 71] a direct approximation to the fluxes can be obtained.
The HLL approximation consists of just three constant states separated by two waves; intermediate waves, such as shear waves and contact discontinuities, are ignored in this approach.
Starting from a Riemann problem at each cell boundary $\left(i+\frac{1}{2},\, j\right)$ with initial data $\left(\overline{\mathbf{U}}^{L}_{i+\frac{1}{2},j},\overline{\mathbf{U}}^{R}_{i+\frac{1}{2},j}\right)$, the HLL numerical flux is given by:

$$\mathbf{F}^{hll}_{i+\frac{1}{2},j}=\begin{cases}\mathbf{F}_L & \text{if}\quad S_L\geq 0\\ \mathbf{F}^{hll}\equiv\dfrac{S_R\mathbf{F}_L-S_L\mathbf{F}_R+S_RS_L\left(\overline{\mathbf{U}}^{R}_{i+\frac{1}{2},j}-\overline{\mathbf{U}}^{L}_{i+\frac{1}{2},j}\right)}{S_R-S_L} & \text{if}\quad S_L\leq 0\leq S_R\\ \mathbf{F}_R & \text{if}\quad S_R\leq 0,\end{cases}\tag{3.40}$$

with $\mathbf{F}_L=\mathbf{F}\left(\overline{\mathbf{U}}^{L}_{i+\frac{1}{2},j}\right)$ and $\mathbf{F}_R=\mathbf{F}\left(\overline{\mathbf{U}}^{R}_{i+\frac{1}{2},j}\right)$.
In Eq.(3.40) S_L and S_R represent an estimate for the smallest and largest signal velocity in the solution of the Riemann problem and several possible choices can be found in [66, 67] for computing such wave speeds.

In order to account also for the influence of intermediate waves, the HLLC Riemann solver (C stands for *Contact*) can be applied. According to a simpler version of such scheme suitable for SWE [67], the first two components of numerical fluxes can be evaluated as in the HLL approach, while the third component, which is the only one that changes across the middle wave, results:

$$\left[\mathbf{F}^{hllc}_{i+\frac{1}{2},j}\right]_3 = \begin{cases} \left[\mathbf{F}^{hll}_{i+\frac{1}{2},j}\right]_1 \cdot \left(\left[\overline{\mathbf{U}}^{L}_{i+\frac{1}{2},j}\right]_3 / \left[\overline{\mathbf{U}}^{L}_{i+\frac{1}{2},j}\right]_1\right) & \text{if} \quad u_* \geq 0 \\ \left[\mathbf{F}^{hll}_{i+\frac{1}{2},j}\right]_1 \cdot \left(\left[\overline{\mathbf{U}}^{R}_{i+\frac{1}{2},j}\right]_3 / \left[\overline{\mathbf{U}}^{R}_{i+\frac{1}{2},j}\right]_1\right) & \text{if} \quad u_* \leq 0 \end{cases} \tag{3.41}$$

The estimate of numerical fluxes according to Step IIIa or Step IIIb allows of computing the solution $\mathbf{U}^{*}_{i,j}$ expressed in Eq.(3.14). The numerical bed slope source term is a function of the evolute reconstructed variables and, according to the centered approximation of Eq.(3.36), it results:

$$\overline{\mathbf{S}}_{0\,i,j} = \begin{bmatrix} 0 \\ -g\,\dfrac{\overline{h}^{L}_{i+\frac{1}{2},j} + \overline{h}^{R}_{i-\frac{1}{2},j}}{2}\,\dfrac{b_{i+\frac{1}{2},j} - b_{i-\frac{1}{2},j}}{\Delta x} \\ -g\,\dfrac{\overline{h}^{L}_{i,j+\frac{1}{2}} + \overline{h}^{R}_{i,j-\frac{1}{2}}}{2}\,\dfrac{b_{i,j+\frac{1}{2}} - b_{i,j-\frac{1}{2}}}{\Delta x} \end{bmatrix}. \tag{3.42}$$

The mathematical proof that WSDGM exactly satisfies the *C-property* is reported in Appendix A.

3.2.5 The Procedure for Mass-Error Control

The occurrence of very small water depths in numerical simulations can lead to instabilities, such as negative water depths and unphysical velocities; moreover, in problems with frictions, the structure of the Manning equation is such that, when water depth tends to zero, the bed resistance tends to infinite. In order to avoid these difficulties, when water depths deriving from algorithm (3.14) are lower than a threshold value, the computational cell is dried. This common procedure leads to a loss of mass when the updated water depth is positive but smaller than h_ϵ, and to a gain when it is negative. In real case studies in which fronts can be very uneven due to the strong bottom irregularities, the mass error

can grow into unacceptable values.
In order to drastically reduce this mass error, when the water depth $h^*_{i,j}$ deriving from the first step of (3.14) is smaller than h_ϵ, in WSDGM a flux correction is performed to obtain $h^*_{i,j} = 0$.
Defining:

$$C_{i,\,j} = \frac{h^*_{i,\,j}\Delta x \Delta y}{\Delta t \left[\left(c_1 \cdot \mathbf{F}^1_{i-\frac{1}{2},j} + c_2 \cdot \mathbf{F}^1_{i+\frac{1}{2},j}\right)\Delta y + \left(c_3 \cdot \mathbf{G}^1_{i,j-\frac{1}{2}} + c_4 \cdot \mathbf{G}^1_{i,j+\frac{1}{2}}\right)\Delta x\right]}, \tag{3.43}$$

where $\mathbf{F}^1$ and $\mathbf{G}^1$ are the first component of the numerical fluxes in x and y directions and c_k $(k = 1, 2, 3, 4)$ are integer coefficients equal to 0 or 1, three different cases can be distinguished:

- $\left(0 \le h^*_{i,\,j} \le h_\epsilon\right) \cap \left(h^n_{i,\,j} = 0\right)$, as occurs, for example, at the wetting front, when the cell, initially dry, is wetted with a water depth smaller than h_ϵ. If $\mathbf{F}^1 \cdot \mathbf{n} < 0$ or, similarly, $\mathbf{G}^1 \cdot \mathbf{n} < 0$ (flow entering the (i,j)-cell), the correspondent coefficient c_k is set at 1, otherwise at 0. If $c_k = 1$ all the components of the numerical flux vector are reduced by the same factor $\alpha_{i,j} = (1 - C_{i,\,j})$, otherwise the flux vector remains unchanged;

- $\left(0 \le h^*_{i,\,j} \le h_\epsilon\right) \cap \left(h^n_{i,\,j} \ge h_\epsilon\right)$, as occurs, for example, at the drying front, when the cell, initially wet, is not completely dried. If $\mathbf{F}^1 \cdot \mathbf{n} > 0$ or, similarly, $\mathbf{G}^1 \cdot \mathbf{n} > 0$ (flow leaving the (i,j)-cell), the correspondent coefficient c_k is set at 1, otherwise at 0. If $c_k = 1$ all the components of the numerical flux vector are increased by the same factor $\alpha_{i,j} = (1 + C_{i,\,j})$, otherwise the flux vector remains unchanged;

- $\left(h^*_{i,\,j} \le 0\right)$, as occurs, for example, at a drying front, when the cell is overdraft. If $\mathbf{F}^1 \cdot \mathbf{n} > 0$ or, similarly, $\mathbf{G}^1 \cdot \mathbf{n} > 0$ (flow leaving the (i,j)-cell), the correspondent coefficient c_k is set at 1, otherwise at 0. If $c_k = 1$ all the components of the numerical flux vector are reduced by the same factor $\alpha_{i,j} = (1 + C_{i,\,j})$, otherwise the flux vector remains unchanged.

After the flux correction, the first step of (3.14) is recomputed; since this procedure can lead to $h^*_{i,\,j} < h_\epsilon$ in the adjacent cells, it is iteratively performed: in this way the mass error is drastically reduced, without significantly increasing the computational effort, as the cells involved by the algorithm are always a

small percentage of the total number of elements at wet/dry interfaces.

3.2.6 Boundary Conditions

Let's consider a $[0, L_x] \times [0, L_y]$ computational domain discretized into a set of grid cells $I_{i,j}$ with $(i = 1, \ldots, N_x;\ j = 1, \ldots, N_y)$. The application of the conservative formula (3.7) for the updating of the extreme cells $I_{1,j}$, $I_{N_x,j}$, $I_{i,1}$ and I_{i,N_y} with $(i = 1, \ldots, N_x; j = 1, \ldots, N_y)$ requires the computation of the numerical fluxes $\mathbf{F}_{\frac{1}{2},j}$, $\mathbf{F}_{N_x+\frac{1}{2},j}$, $\mathbf{G}_{i,\frac{1}{2}}$ and $\mathbf{G}_{i,N_y+\frac{1}{2}}$. In order to make the information necessary for the estimate of such fluxes available, the computational domain is extended at the extreme boundaries including additional cells (*ghost cells*) [66, 67, 44], whose values are set at the beginning of each time step according to the boundary conditions and independently from the choice of the numerical method applied.
The number of ghost cells n_{gc} to add at each side is related to the wideness of the stencil on which the numerical fluxes depend; for a SLIC-type method $n_{gc} = 2$.
Below the different boundary conditions to assign to the conserved variables, the bottom elevation and the Manning coefficient are listed.

Reflective Conditions. Let's consider the boundary $x = 0$ and suppose it physically consists of a fixed, reflective, impermeable wall. Along a reflective boundary the component of velocity orthogonal to the wall is equal to zero, since no mass can penetrate the solid body; this condition is modeled imposing:

$$\begin{cases} h_{1-i,j} = h_{1,j} \\ u_{1-i,j} = -u_{1,j} \\ v_{1-i,j} = v_{1,j} \\ z_{1-i,j} = z_{1,j} \\ n_{1-i,j} = n_{1,j} \end{cases} \qquad (i = 1, 2;\ j = 1, \ldots, N_y)\,. \tag{3.44}$$

Transmissive Condition. In order to deal with finite, or sufficiently small, computational domains, the imposition of a transmissive (*far-field*) condition [11, 57, 26, 40, 66] is an attempt to produce boundaries that allow the

passage of waves without any effect on them. The following constraints on the variables produce a trivial Riemann problem; no wave of finite strength is produced at the boundary that may affect the flow inside the domain. For a transmissive left boundary placed at $x = 0$, a first-order extrapolation from the interior domain for the bed elevation and a zero-order extrapolation for the other variables are performed as follows:

$$\begin{cases} h_{1-i,j} = h_{1,j} \\ u_{1-i,j} = u_{1,j} \\ v_{1-i,j} = v_{1,j} \\ z_{i-2,j} = 2z_{i-1,j} - z_{i,j} \\ n_{1-i,j} = n_{1,j} \end{cases} \qquad (i = 1, 2;\ j = 1, \ldots, N_y)\,. \tag{3.45}$$

Inflow Condition. From the imposition of a specific discharge $uh\,(0, y, t) = \overline{q}\,(t)$ at the left boundary $x = 0$, it results:

$$\begin{cases} h_{1-i,j} = h_{1,j} \\ uh_{1-i,j} = \overline{q}\,(t) \\ vh_{1-i,j} = 0 \\ z_{i-2,j} = 2z_{i-1,j} - z_{i,j} \\ n_{1-i,j} = n_{1,j} \end{cases} \qquad (i = 1, 2;\ j = 1, \ldots, N_y)\,. \tag{3.46}$$

Fixed Water Depth Condition. From the imposition of a fixed water depth $\overline{h}\,(t)$ in the cells $I_{0,j}$ $(j = 1, \ldots, N_y)$, it results:

$$\begin{cases} h_{1-i,j} = \overline{h}\,(t) \\ u_{1-i,j} = u_{1,j} \\ v_{1-i,j} = v_{1,j} \\ z_{i-2,j} = z_{1,j} \\ n_{1-i,j} = n_{1,j} \end{cases} \qquad (i = 1, 2;\ j = 1, \ldots, N_y)\,. \tag{3.47}$$

3.2.7 Divergence Form of Bed Slope Source Term (DFB)

In this subsection the recent technique proposed by Valiani & Begnudelli [74] for the discretization of the bed slope source term is presented. Since the simplest way towards the numerical closure of physical balances is the divergence form of physical laws [34], the idea is to rewrite the bed slope source term, which contains the product of the flow depth by a spatial derivative of the bed elevation, as the spatial derivative of a physical quantity.
Referring to the 1D case, the authors proved that (see [74] for details):

$$gh\left(-\frac{\partial b}{\partial x}\right) = \frac{\partial}{\partial x}\left(\frac{1}{2}gh^2\right)\Big|_{\eta=\eta^*}, \tag{3.48}$$

namely the source term can be rewritten as the partial derivative with respect to x of the quantity $gh^2/2$ evaluated for a constant value η^* of the free surface elevation over each considered interval.
Extending to the 2D case, the terms defined in Eq.(2.13) become:

$$S_{0x} = -gh\frac{\partial b}{\partial x} = \frac{\partial}{\partial x}\left(\frac{1}{2}gh^2\right)\Big|_{\eta=\eta^*} \quad S_{0y} = -gh\frac{\partial b}{\partial y} = \frac{\partial}{\partial y}\left(\frac{1}{2}gh^2\right)\Big|_{\eta=\eta^*}. \tag{3.49}$$

Introducing the matrix:

$$\mathbf{H}_b = [\mathbf{F}_b, \mathbf{G}_b] = \begin{bmatrix} 0 & 0 \\ \frac{1}{2}gh^2 & 0 \\ 0 & \frac{1}{2}gh^2 \end{bmatrix}, \tag{3.50}$$

the bed slope source term $\mathbf{S}_0$ can be rewritten in divergence form as:

$$\mathbf{S}_0 = \nabla \cdot \mathbf{H}_b|_{\eta=\eta^*} \tag{3.51}$$

and the 2D SWE become:

$$\frac{\partial \mathbf{U}}{\partial t} + \nabla \cdot \mathbf{H} = \nabla \cdot \mathbf{H}_b|_{\eta=\eta^*} + \mathbf{S}_f. \tag{3.52}$$

Adopting the presented approach in a finite volume framework, the discretization of $\mathbf{S}_0$ can be performed with the same procedure adopted for numerical fluxes. Integrating (3.51) over a Cartesian cell, after some mathematical manipulations [74], one obtains:

$$\mathbf{S}_{0\,i,j} = \begin{bmatrix} 0 \\ \frac{1}{2}g\big(\widehat{h}^2_{i+\frac{1}{2},j} - \widehat{h}^2_{i-\frac{1}{2},j}\big)\Delta y \\ \frac{1}{2}g\big(\widehat{h}^2_{i,j+\frac{1}{2}} - \widehat{h}^2_{i,j-\frac{1}{2}}\big)\Delta x \end{bmatrix}, \tag{3.53}$$

where $\widehat{h}$ represents the water depth characteristic of each cell-sides.
The free surface $\eta^*_{i,j}$, constant over each cell, is equal to the sum of the average water depth $h_{i,j}$ and the bed elevation $b_{i,j}$ of the cell; the numerical water depths $\widehat{h}$ are evaluated as the difference between $\eta^*_{i,j}$ and the bed elevation $\widehat{b}$ at the mid point of the different cell sides, taken as the mean between the elevations of the two vertices of each side.
This technique is quite simple to implement and also versatile, since it can be applied independently from the numerical scheme and the domain discretization adopted. Moreover, this approach allows the satisfaction of the condition of quiescent fluid over an irregular topography in case of fully wet cells.
A delicate task in solving shallow water problems concerns the treatment of partially wet cells. Since each vertex has a different elevation, the cell bottom does not lie on a horizontal plane and partially wet cells can occur at wet/dry fronts; in this situation the DFB technique does not ensure of satisfying of the *C-property*.
Referring to this problem, in the Discussion about the paper by Valiani & Begnudelli [74], Greco et al.[28] introduced a simple correction for the evaluation of the numerical water depth $\widehat{h}$, which allows to maintain the static condition of quiescent fluid also in the presence of partially dry cells.
In 1D case it reads:

$$\widehat{h} = \frac{\big(\widehat{h} - \widehat{b}\big) + \big|\widehat{h} - \widehat{b}\big|}{2}. \tag{3.54}$$

However, in two dimensions the handling of partially wet quadrangular elements in dynamic situations remains a challenge. In fact it is not computationally straightforward to find a procedure that takes into account the volume inside a

partially wet cell, especially when the barycenter is dry and at least one of the vertex is submerged. In this situation a new smaller element with a barycenter differently positioned should be defined and the updated conserved variables should be referred to the new barycenter.

Chapter 4

Test Cases with a Reference Solution

In this Chapter the robustness and effectiveness of the proposed WSDGM are assessed applying it to non-flat topography reference test cases. The dynamics of wetting and drying and the occurrence of complex structures in the flow field, such as moving shocks and reflections, mean that the tests are severe.
Among the possible options presented in the literature [35, 44], the *Van Leer limiter* function was adopted.
In all the tests performed the FORCE flux is applied and the *Fractional Step* method is adopted for the time updating of the solution.

4.1 1D Steady Flows over a Steep Bump

These tests concern 1D steady flows in a $[-10\text{ m} \leq x \leq, +10\text{ m}]$ frictionless channel. The bottom profile, characterized by the presence of a steep bump, is described by the following equation:

$$z(x) = \begin{cases} b_c \left(1 - \dfrac{x^2}{4}\right) & -2\text{ m} \leq x \leq 2\text{ m} \\ 0 & \text{elsewhere,} \end{cases} \tag{4.1}$$

where the height of the bump b_c is set at 0.8 [45] instead of the usual value 0.2 (e.g. [82, 74, 12]), in order to make the test more severe. The computational domain is discretized with square cells of 0.1 m.
According to the conditions imposed at the boundaries (Table 4.1), the water can be at rest (Test A, with initial condition $\eta(x) = 1$ m) or the flow can be transcritical with (Test B) or without (Test C) the occurrence of a hydraulic jump, supercritical (Test D) or subcritical (Test E).
The five cases were simulated by means of the WSDGM scheme with different

Table 4.1. Boundary conditions and Fr range for 1D steady flows over a bump.

Test	**Upstream B.C.**	**Downstream B.C.**	**Fr range**
A	$q = 0.0\,\mathrm{m}^2/\mathrm{s}$	$h = 1.0$ m	0
B	$q = 0.4\,\mathrm{m}^2/\mathrm{s}$	$h = 0.75$ m	$0.10 - 4.00$
C	$q = 0.4\,\mathrm{m}^2/\mathrm{s}$	transmissive	$0.10 - 5.03$
D	$q = 1.5\,\mathrm{m}^2/\mathrm{s},\ h = 0.25$ m	transmissive	$2.31 - 3.83$
E	$q = 1.0\,\mathrm{m}^2/\mathrm{s}$	$h = 1.70$ m	$0.14 - 0.41$

values of $\mathrm{Fr}_{\mathrm{lim}}$ ranging from $\mathrm{Fr}_{\mathrm{lim}} = 0$ (pure DGM reconstruction) to $\mathrm{Fr}_{\mathrm{lim}} \to \infty$ (pure SGM reconstruction).
Table 4.2 compares the L_1 errors in h and q as a function of $\mathrm{Fr}_{\mathrm{lim}}$, which are defined as:

$$L_1(h) = \frac{1}{N}\sum_{i=1}^{N}\left|\frac{h_{i,num} - h_{i,ref}}{h_{i,ref}}\right|, \quad L_1(q) = \frac{1}{N}\sum_{i=1}^{N}\left|\frac{q_{i,num} - q_{ref}}{q_{ref}}\right|, \tag{4.2}$$

where N is the total number of computational cells, $h_{i,ref}$ is the reference solution derived from the energy equation (together with the momentum principle if a hydraulic jump is present) and q_{ref} is the constant value of the specific discharge.
Even though in Test E a pure SGM reconstruction ($\mathrm{Fr}_{\mathrm{lim}} \to \infty$) gives a slightly better result, on average the lowest L_1 errors are obtained for values of $\mathrm{Fr}_{\mathrm{lim}}$ in the interval $[1, 2]$. Since in this range the norms are almost the same, the value $\mathrm{Fr}_{\mathrm{lim}} = 2$ is chosen to give insight into the results. Fig.4.1 compares, in the subdomain $[-3\ \mathrm{m} \le x \le 3\ \mathrm{m}]$, reference water level profiles and unit discharges with those computed assuming $\mathrm{Fr}_{\mathrm{lim}} = 0$, $\mathrm{Fr}_{\mathrm{lim}} = 2$ and $\mathrm{Fr}_{\mathrm{lim}} \to \infty$.
As shown by numerical profiles and L_1 norms for Test A, the pure DGM reconstruction ($\mathrm{Fr}_{\mathrm{lim}} = 0$) does not satisfy the *C-property*.
In the subcritical regions of Tests B, C, E, the results obtained adopting $\mathrm{Fr}_{\mathrm{lim}} =$

Table 4.2. L_1 errors for h and q as function of $\mathrm{Fr}_{\mathrm{lim}}$.

	Test A	**Test B**		**Test C**		**Test D**		**Test E**	
$\mathrm{Fr}_{\mathrm{lim}}$	$L_1(h)$	$L_1(h)$	$L_1(q)$	$L_1(h)$	$L_1(q)$	$L_1(h)$	$L_1(q)$	$L_1(h)$	$L_1(q)$
0	2.0E-3	3.2E-3	3.9E-3	4.4E-4	6.2E-4	2.0E-4	8.7E-5	3.2E-4	4.3E-4
0.2	0.0E+0	3.2E-3	3.7E-3	4.4E-4	4.6E-4	2.0E-4	8.7E-5	3.0E-4	4.1E-4
1	0.0E+0	3.1E-3	3.5E-3	4.3E-4	1.9E-4	2.0E-4	8.7E-5	6.3E-5	1.0E-4
2	0.0E+0	3.2E-3	3.5E-3	6.0E-4	1.6E-4	2.0E-4	8.7E-5	2.9E-5	4.0E-5
5	0.0E+0	3.3E-3	3.7E-3	6.5E-4	1.8E-4	1.1E-3	3.3E-4	1.9E-5	2.6E-5
20	0.0E+0	3.9E-3	4.8E-3	6.2E-3	5.4E-3	2.4E-3	9.3E-4	1.7E-5	3.2E-5
$\to \infty$	0.0E+0	4.0E-3	5.3E-3	1.1E-2	9.8E-3	2.6E-3	1.1E-3	1.7E-5	2.3E-5

0 show a dip in the water elevation upstream and downstream of the bump, where the bottom profile is not smooth.
If the flow is supercritical downstream from the bump (Tests C and D), the numerical scheme with $\mathrm{Fr}_{\mathrm{lim}} \to \infty$ badly converges toward the steady solution, as shown by L_1 norms and oscillations in water elevation and unit discharge profiles. It was verified that tests analogous to B, C and D, characterized by boundary conditions giving rise to a thinner nappe over the last part of the bump, cannot be carried out if a pure SGM reconstruction is performed (e.g. Test B with $q = 0.25\,\mathrm{m}^2/\mathrm{s}$ and $h = 0.60\,\mathrm{m}$).
In Test B a deviation of the computed discharges from the reference solution occurs close to the hydraulic jump; a similar behavior can be found in [82, 74] even though $b_c = 0.2$ m. This deviation is the main source of error and gives rise to comparable L_1 norms for all the examined values of $\mathrm{Fr}_{\mathrm{lim}}$.
When $\mathrm{Fr}_{\mathrm{lim}} = 0$ and the flow is completely subcritical (Tests A, E) the bottom discontinuities induce deviations in q at the beginning and end of the bump; the same behavior occurs in Test D for $\mathrm{Fr}_{\mathrm{lim}} \to \infty$.
On the whole, the results obtained for these test cases prove that WSDGM with $\mathrm{Fr}_{\mathrm{lim}} = 2$ performs better than the schemes based on pure DGM or SGM reconstructions. For this reason, the parameter $\mathrm{Fr}_{\mathrm{lim}}$ was also set at 2 in the following tests.

In order to numerically prove that WSDGM is second order accurate and it is capable of reconstructing the theoretical solutions, a convergence analysis on the grid size was performed with reference to Test C. Four different grid spacings were used, starting from $\Delta x = 0.2$ m, and successively halving the value to obtain the remaining grids. Fig.4.2 shows that the L_1 norms in h, q and energy per unit mass E vanish like $\mathcal{O}\left(\Delta x^2\right)$ when the grid is progressively refined.

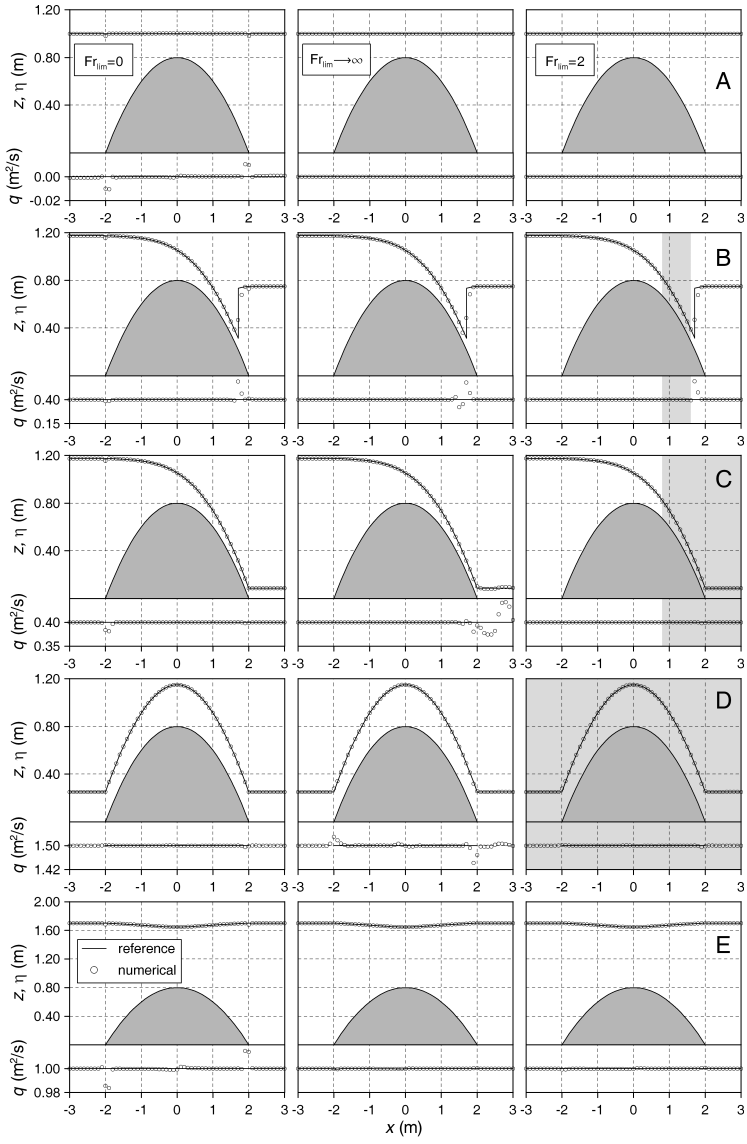

Figure 4.1. 1D steady flows over a steep bump: comparison between reference solution and numerical results. In the shaded region Fr ≥ 2.

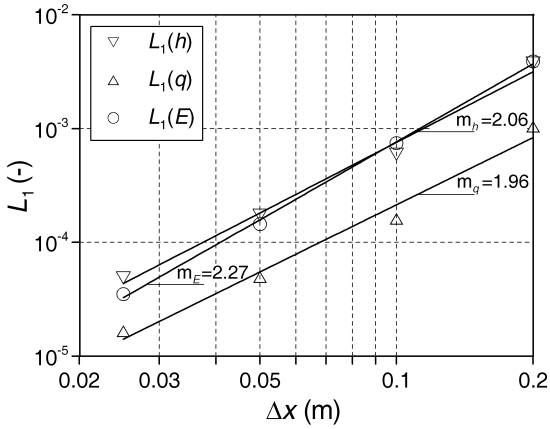

Figure 4.2. TestC: $L_1(h)$, $L_1(q)$ and $L_1(E)$ as function of Δx, computed with WSDGM and $\mathrm{Fr}_{\mathrm{lim}} = 2$.

4.2 1D Steady Flows over a Bottom Step

These tests concern 1D steady flows induced by Riemann problems of SWE with a bottom step, whose exact solutions were provided by Alcrudo & Benkhaldoun in 2001 [1].
If the functions involved are smooth, the mass-momentum form of the 1D SWE:

$$\frac{\partial}{\partial t}\begin{bmatrix} h \\ hu \end{bmatrix} + \frac{\partial}{\partial x}\begin{bmatrix} hu \\ hu^2 + gh^2/2 \end{bmatrix} = \begin{bmatrix} 0 \\ -gh\frac{\mathrm{d}b}{\mathrm{d}x} \end{bmatrix} \tag{4.3}$$

can be manipulated and rewritten in the mass-energy form:

$$\frac{\partial}{\partial t}\begin{bmatrix} h \\ u/g \end{bmatrix} + \frac{\partial}{\partial x}\begin{bmatrix} hu \\ h + u^2/2g + b \end{bmatrix} = 0, \tag{4.4}$$

where the quantity:

$$H_{tot} = h + u^2/2g + b \tag{4.5}$$

is the total available head, representing the total mechanical energy of the flow expressed in terms of potential energy divided by g.
While Eq.(4.3) is the only valid in case the solution contains a hydraulic jump, Eq.(4.4) may still be valid when the bottom surface function $b(x)$ is not continuous.
Dealing with steady state solutions, Eq.(4.4) provides:

$$H_{tot} = h + u^2/2g + b = h + q^2/2gh^2 + b = \text{constant} \tag{4.6}$$

and defining the specific head:

$$H_s = H_{tot} - b = h + q^2/2gh^2, \tag{4.7}$$

Eq.(4.6) can be rewritten in dimensionless form as:

$$\left(\frac{h}{H_s}\right)^3 - \left(\frac{h}{H_s}\right)^2 + \frac{q^2}{2gH_s^3} = 0, \tag{4.8}$$

which is a cubic equation of the form:

$$x^3 - x^2 + \alpha = 0, \tag{4.9}$$

with

$$\alpha = \frac{q^2}{2gH_s^3} \geq 0. \tag{4.10}$$

Let's consider two consecutive section (S1 and S2) in a stream with arbitrary topography and in steady flow condition. If the flow state is known at S1, the flow at S2 can be evaluated with the following procedure, named *Stationary Step Transition* (SST):

1. compute the value of H_{tot} from known variables at S1, as:

$$H_{tot} = h_1 + u_1^2/2g + b_1; \tag{4.11}$$

2. obtain the specific head at S2, H_{S2} as:

$$H_{S2} = H_{tot} - b_2 = H_{S1} + b_1 - b_2; \tag{4.12}$$

3. compute the value of α at S2, α_2, from Eq.(4.10);

4. solve Eq.(4.9) and obtain h_2 as:

$$h_2 = H_{S2}x; \tag{4.13}$$

5. then compute the value of u_2 from:

$$u_2 = q/h_2 = u_1 h_1/h_2; \tag{4.14}$$

Additional considerations about the choice of physically meaningful solutions make the procedure slightly more complicated, see [1] for details.
The Riemann problem with a bottom step is characterized by the presence of a discontinuity not only in the initial conditions:

$$\mathbf{U}(x,0) = \begin{cases} \mathbf{U}_L & \text{if } x < 0 \\ \mathbf{U}_R & \text{if } x > 0, \end{cases} \tag{4.15}$$

but also in the bottom function:

$$b(x) = \begin{cases} 0 & \text{if } x < 0 \\ \Delta z & \text{if } x > 0, \end{cases} \tag{4.16}$$

in $x \in [-\infty, +\infty]$ and for $t > 0$.
To either side but very close to the step ($x = 0^{\pm}$) the solution is a similarity solution, which must be constant in time; immediately to the left and the right of the step one has:

$$\mathbf{U}\left(0^{\pm}, t\right) = \mathbf{f}\left(0^{\pm}, t\right) = \mathbf{f}\left(0^{\pm}\right) \tag{4.17}$$

just like it happens without a step at $x = 0$. Although in this case $\mathbf{U}(0^-, t) \neq \mathbf{U}(0^+, t)$, such states must be connected by a SST.
Calling these constant states $\mathbf{U}_2$ and $\mathbf{U}_3$:

$$\begin{aligned} \mathbf{U}_2 &= \mathbf{U}\left(0^-, t\right) = \mathbf{f}\left(0^-\right) \\ \mathbf{U}_3 &= \mathbf{U}\left(0^+, t\right) = \mathbf{f}\left(0^+\right), \end{aligned} \tag{4.18}$$

the relation

$$\mathbf{U}_3 = \mathrm{SST}\left(\mathbf{U}_2\right) \tag{4.19}$$

must hold.
Since the initial states $\mathbf{U}_L$ and $\mathbf{U}_R$ stand far from the step at any finite time, it is reasonable to think that between the step and the two initial states the solution is made up of simple waves ($W_{L,R}$) connecting $\mathbf{U}_L$ and $\mathbf{U}_2$ and $\mathbf{U}_3$ and $\mathbf{U}_R$, just like it happens in the standard Riemann problem. Hence, the solution can be represented by the following diagram:

$$\mathbf{U}_L \overset{W_L}{\rightarrow} \mathbf{U}_2 \overset{\mathrm{SST}}{\rightarrow} \mathbf{U}_3 \overset{W_R}{\rightarrow} \mathbf{U}_R. \tag{4.20}$$

The numerical results of a set of Riemann problems with a bottom step characterized by different initial conditions will be shown in the following subsections. All the tests are referred to a frictionless $[-10\ \mathrm{m} \leq x \leq +10\ \mathrm{m}]$ channel discretized with a square mesh of size 0.02 m.
Although no special treatment for the bottom step was implemented and the discontinuity was simply described with two grid elements, the treatment of the bottom slope source term performed in WSDGM is suitable to obtain a satisfactory fitting between numerical and analytical results as it will be shown in the following subsections.
In the numerical simulations $\mathrm{Fr}_{\mathrm{lim}}$ was set at 2 and the Courant number Cr at 0.95.

4.2.1 Test Problem A1 (*L*-rar., *R*-shock)

Initial Conditions:

$$\begin{aligned} h(x,0) &= \begin{cases} 4\text{ m} & x<0 \\ 2\text{ m} & x>0 \end{cases} \\ u(x,0) &= \begin{cases} 0\text{ m/s} & x<0 \\ 0\text{ m/s} & x>0 \end{cases} \\ b(x) &= \begin{cases} 0\text{ m} & x<0 \\ 1\text{ m} & x>0. \end{cases} \end{aligned} \tag{4.21}$$

Such conditions produce a L-rarefaction wave spreading to the left and a R-shock traveling right; the flows maintains subcritical everywhere as shown by the Froude number graph. The analytical solution can be computed in the following steps:

1. compute the family of states $R_L(\mathbf{U}_L)$,
2. compute the conjugate across the step transition of the above family, $\mathrm{SST}(R_L(\mathbf{U}_L))$,
3. compute the family of states $S_R(\mathbf{U}_R)$,
4. compute the conjugate across the step transition of the above family $\mathrm{SST}(S_R(\mathbf{U}_R))$,
5. obtain $\mathbf{U}_2$ from the intersection

$$\mathbf{U}_2 = R_L(\mathbf{U}_L) \cap \mathrm{SST}(S_R(\mathbf{U}_R)), \tag{4.22}$$

6. obtain $\mathbf{U}_3$ from the intersection

$$\mathbf{U}_3 = S_R(\mathbf{U}_R) \cap \mathrm{SST}(R_L(\mathbf{U}_L)). \tag{4.23}$$

The state-wave diagram reads:

$$\mathbf{U}_L \overset{R_L}{\rightarrow} \mathbf{U}_2 \overset{\text{SST}}{\rightarrow} \mathbf{U}_3 \overset{S_R}{\rightarrow} \mathbf{U}_R. \tag{4.24}$$

In Fig.4.3 the comparison between numerical and analytical results at $t = 1$ s is shown.

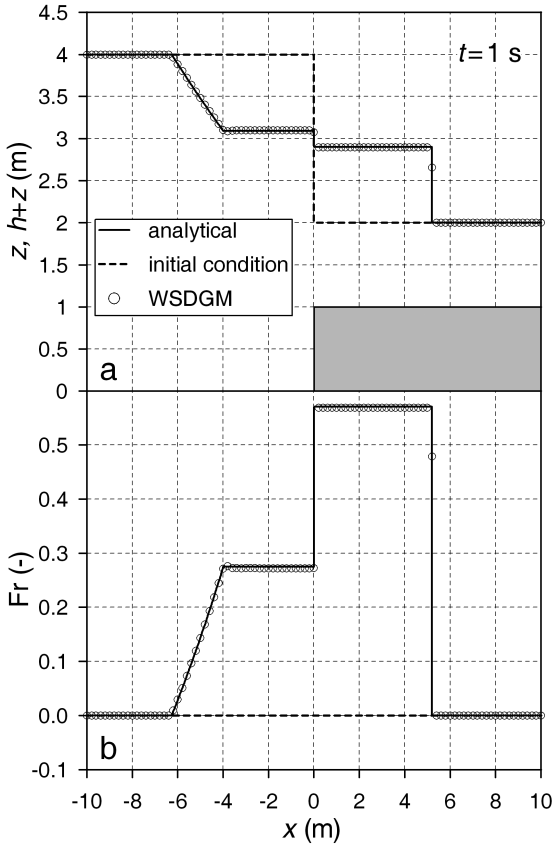

Figure 4.3. Test A1: comparison between analytical and numerical profiles of (a) surface level and (b) Froude number.

4.2.2 Test Problem A2 (*L*-rar., critical SST, *R*-rar., *R*-shock)

Initial Conditions:

$$\begin{aligned} h(x,0) &= \begin{cases} 18\text{ m} & x<0 \\ 2\text{ m} & x>0 \end{cases} \\ u(x,0) &= \begin{cases} 0\text{ m/s} & x<0 \\ 0\text{ m/s} & x>0 \end{cases} \\ b(x) &= \begin{cases} 0\text{ m} & x<0 \\ 1\text{ m} & x>0. \end{cases} \end{aligned} \tag{4.25}$$

The previous initial conditions give rise to the following wave-state diagram:

$$\mathbf{U}_L \overset{R_L}{\rightarrow} \mathbf{U}_2 \overset{\text{SST}}{\rightarrow} \mathbf{U}_3 \overset{R_L}{\rightarrow} \mathbf{U}_* \overset{S_R}{\rightarrow} \mathbf{U}_R, \tag{4.26}$$

where $\mathbf{U}_3$ is the critical state ($\text{Fr}_3 = 1$). The rightmost position of R_L is fixed by the condition that the conjugate of $\mathbf{U}_2$ across the state transition leads to the critical state $\mathbf{U}_3$. $\mathbf{U}_*$ represents the intermediate state separating R_L and S_R. In Fig.4.4 the comparison between numerical and analytical results at $t = 0.5$ s is shown; a little underestimate in the numerical surface level is visible at the beginning of the $\mathbf{U}_2$ state.

4.2.3 Test Problem A3 (*L*-rar., critical SST, *R*-rar., dry bed)

Initial Conditions:

$$\begin{aligned} h(x,0) &= \begin{cases} 4\text{ m} & x<0 \\ 0\text{ m} & x>0 \end{cases} \\ u(x,0) &= \begin{cases} 0\text{ m/s} & x<0 \\ 0\text{ m/s} & x>0 \end{cases} \\ b(x) &= \begin{cases} 0\text{ m} & x<0 \\ 1\text{ m} & x>0. \end{cases} \end{aligned} \tag{4.27}$$

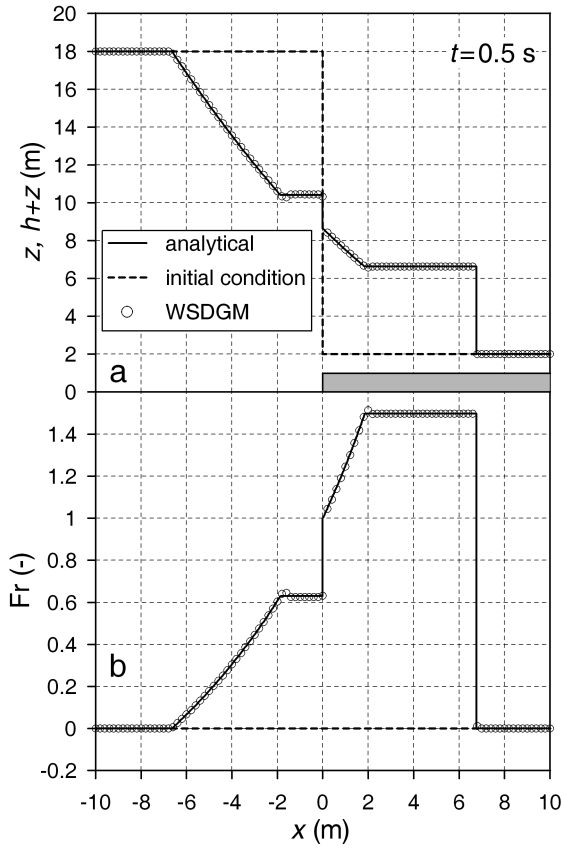

Figure 4.4. Test A2: comparison between analytical and numerical profiles of (a) surface level and (b) Froude number.

The configuration of Test A2 admits also a dry bed solution when $\mathbf{U}_R$ is the vacuum. The state-wave diagram is:

$$\mathbf{U}_L \overset{R_L}{\rightarrow} \mathbf{U}_2 \overset{\text{SST}}{\rightarrow} \mathbf{U}_3 \overset{R_L}{\rightarrow} \mathbf{U}_R = 0 \tag{4.28}$$

and $\mathbf{U}_3$ remains critical. The numerical results are compared with the analytical ones at $t = 0.8$ s in Fig.4.5; this case highlights also the good tracking of the wetting front position.

4.3 1D Steady Flows in Sloping Channels with Friction

In 1996 MacDonald [48, 49] provided analytical benchmark solutions for 1D steady flows in open channels which may have nonprismatic section, nonuniform slope and transition between critical and supercritical state. The solution is based on the construction of an *inverse problem*, which determines the bed slope for a desired water depth and flow rate.
The steady form of the Saint Venant equation [19]:

$$\left(1 - \frac{Q^2 B}{gA^3}\right)\frac{dy}{dt} - \frac{Q^2}{gA^3}\frac{\partial A}{\partial x} - S_0 + Sf = 0, \tag{4.29}$$

in which Q is the flow rate, A and B are the area and the width of the fluid section, can be rewritten as:

$$S_0 = f_1\left[x, h\left(x\right)\right] h'\left(x\right) + f_2\left[x, h\left(x\right)\right], \tag{4.30}$$

where

$$f_1 = 1 - \frac{Q^2 B}{gA^3}, \quad f_2 = \frac{Q^2 n^2 P^{4/3}}{A^{10/3}} - \frac{Q^2}{gA^3}\frac{\partial A}{\partial x}, \tag{4.31}$$

with P the wetted perimeter and n the Manning coefficient.
Considering a reach $0 \leq x \leq L$, once that Q and n are assigned, and B, P and A are known functions of x and h, the functions f_1 and f_2 are completely defined. Finally, choosing arbitrarily a depth profile $\widehat{h}\left(x\right)$ differentiable everywhere, the bed slope S_0 can be derived from Eq.(4.30):

$$S_0 = f_1\left[x, \widehat{h}\left(x\right)\right]\widehat{h}'\left(x\right) + f_2\left[x, \widehat{h}\left(x\right)\right]. \tag{4.32}$$

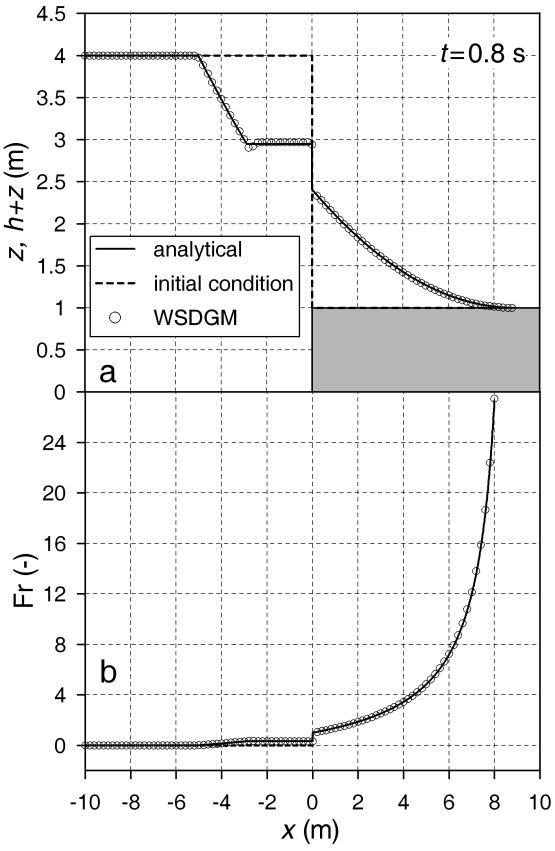

Figure 4.5. Test A3: comparison between analytical and numerical profiles of (a) surface level and (b) Froude number.

When a hydraulic jump occurs at x^* the water depth profile is given by $\widehat{h}_l(x)$ for $(x \leq x^*)$ and $\widehat{h}_r(x)$ for $(x > x^*)$ and, consequently, the bed slope of the channel can be defined as:

$$\begin{aligned} S_{0l} &= f_1\big[x, \widehat{h}_l(x)\big]\widehat{h}_l'(x) + f_2\big[x, \widehat{h}_l(x)\big] \\ S_{0r} &= f_1\big[x, \widehat{h}_r(x)\big]\widehat{h}_r'(x) + f_2\big[x, \widehat{h}_r(x)\big]. \end{aligned} \tag{4.33}$$

In order to let the discontinuity be physically admissible, some constraints have to be imposed on the left and right profiles and on their derivatives:

a. the water depth values $\widehat{h}_l(x^*)$ and $\widehat{h}_r(x^*)$ must satisfy the continuity of the specific force across the jump;

b. even if in many cases the jump is triggered by a bed slope discontinuity, the jump position does not coincide with the discontinuity position; hence, the values of the first derivatives of water depths $\widehat{h}_l'(x^*)$ and $\widehat{h}_r'(x^*)$ must satisfy the relation $S_{0l}(x^*) = S_{0r}(x^*)$;

c. a further relationship between $\widehat{h}_l''(x^*)$ and $\widehat{h}_r''(x^*)$ can be imposed ensuring that the bed slope is differentiable at the jump, i.e. $S_{0l}'(x^*) = S_{0r}'(x^*)$.

The test problem reported below was constructed according to the following steps:

1. the function $\widehat{h}_l$ is chosen arbitrarily;
2. the conditions *a*, *b*, *c* are used to determine the required values of $\widehat{h}_r$, $\widehat{h}_r'$ and $\widehat{h}_r''$ at x^*;
3. the form of the function $\widehat{h}_r(x)$ is chosen with at least three free parameters;
4. values of these parameters are chosen so as to give the required values for $\widehat{h}_r$, $\widehat{h}_r'$ and $\widehat{h}_r''$ at x^*.

4.3.1 Test Problem MD1

A 1500 m-long rectangular channel ($B = 1$ m) has a discharge $Q = B\sqrt{g}$ m^3/s and a roughness coefficient $n = 0.02$ s/m$^{1/3}$. The flow is subcritical at inflow and is subcritical at outflow with a depth $\widehat{h}(1500) = 4$ m.
The bed slope is given by:

$$S_0 = \left(1 - \frac{1}{\widehat{h}^3}\right)\widehat{h}' + \frac{0.0039224}{\widehat{h}^{10/3}}, \tag{4.34}$$

where

$$\widehat{h}(x) = \begin{cases} 1 - \tanh\left(\dfrac{x}{1000} - 0.5\right) & 0 \le x \le 1000 \\ p + \displaystyle\sum_{k=1}^{3} c_k \exp^{\alpha k\left(\frac{x}{1000}-1\right)} + q\exp^{\left(\frac{x}{1500}-1\right)} & 1000 < x \le 1500 \end{cases} \tag{4.35}$$

with $p = 2.5$, $q = 1.5$, $\alpha = -40$ and the coefficients $c_1 = -3.19223$, $c_2 = 1.772244$ and $c_3 = -0.476803$.
Fig.4.6a,b show respectively the analytical surface level and the analytical water depth compared with the numerical results obtained with WSDGM, adopting a grid of size 5 m . The very good agreement proves the effectiveness of the treatments of the bed slope and friction source terms; moreover, the high resolution method allows to catch the hydraulic jump without spreading and oscillation.

4.3.2 Dam-break in a sloping channel

In this subsection, the rapidly varying 1D flow induced by a dam-breaking in a frictionless sloping channel is investigated (Fig.4.7). Among the tests for which an analytical solution of wet/dry fronts is available [56, 64], this is one of the most strongly influenced by the threshold value h_ϵ, because the water body lengthens indefinitely, becoming thinner and thinner. For this reason, the dam-break in a sloping channel was chosen as the reference test for the evaluation of the threshold effects on the front tracking.
Following Hunt [38] and introducing the set of dimensionless variables:

$$\overline{x} = \frac{x}{h_0}, \quad \overline{t} = \frac{t\sqrt{g}}{\sqrt{h_0}} S_0, \quad \overline{h} = \frac{h}{h_0}, \quad \overline{u} = \frac{u}{\sqrt{g h_0}}, \quad \overline{c} = \frac{c}{\sqrt{g h_0}} = \sqrt{\overline{h}}, \tag{4.36}$$

where h_0 is the water depth behind the dam, S_0 is the bed slope and c is the speed of small amplitude waves in still water, it is possible to rewrite the 1D De St. Venant equations in the dimensionless characteristic form:

$$\begin{cases} \dfrac{\mathrm{d}\overline{x}_\pm}{\mathrm{d}\overline{t}} = \overline{u} \pm \overline{c} \\ \dfrac{\mathrm{d}}{\mathrm{d}\overline{t}}\Big(\overline{u}\left(\overline{x}_\pm;\, \overline{t}\right) \pm 2\overline{c}\left(\overline{x}_\pm;\, \overline{t}\right) - \overline{t}\Big) = 0. \end{cases} \tag{4.37}$$

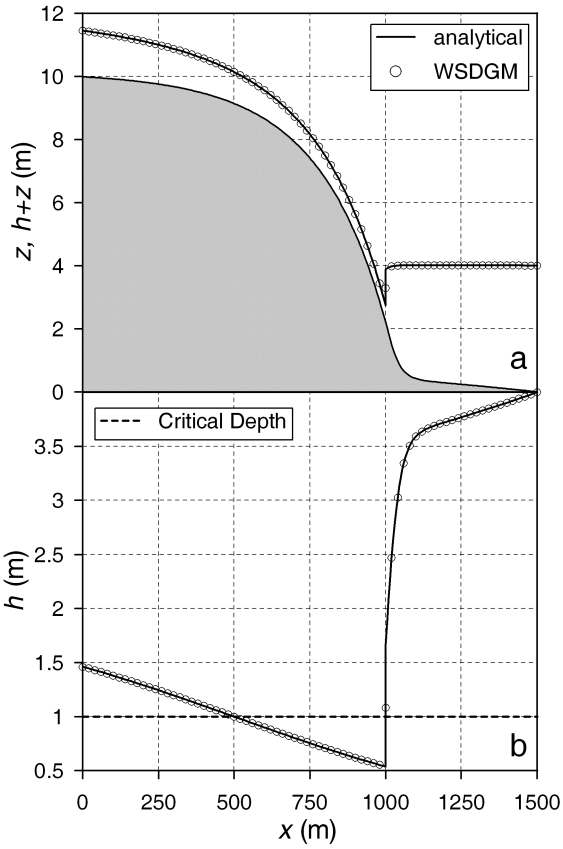

Figure 4.6. Test MD1: comparison between analytical and numerical profiles of (a) surface level profiles and (b) water depths.

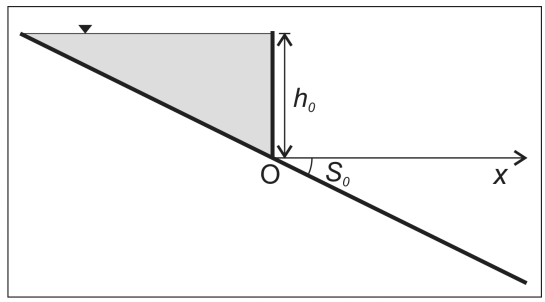

Figure 4.7. Definition sketch for the dam-break problem in a sloping channel.

From (4.37) the dimensionless expression of the drying and wetting front ($\overline{x}_{dry}$, $\overline{x}_{wet}$) can be derived [38]:

$$\overline{x}_{dry} = \frac{1}{2}\left(\overline{t} - 2\right)^2 - 1 \quad \left(\overline{t} \geq 2\right), \tag{4.38}$$

$$\overline{x}_{wet} = \frac{1}{2}\left(\overline{t} + 2\right)^2 - 2. \tag{4.39}$$

In the numerical simulation a $[-10\text{ m} \leq x \leq 150\text{ m}]$ channel of slope $S_0 = 0.1$ was discretized with a mesh of size 0.1 m. The dam section was placed at $x = 0$ and the maximum water depth h_0 was set at the value of 1 m.
The comparison between analytical and numerical fronts is shown in Fig.4.8. The wetting front is not particularly sensitive to the value of the dimensionless threshold $\overline{h}_\epsilon = h_\epsilon/h_0$, but the drying process is more so. In particular, the numerical drying fronts obtained imposing $\overline{h}_\epsilon = 10^{-5}$ and $\overline{h}_\epsilon = 10^{-4}$ are respectively behind and ahead the analytical solution.
The drying front is obviously influenced by the grid dimension too. Table 4.3 compares the L_2 norm of the drying front position as a function of Δx, which are defined as:

$$L_2\left(\overline{x}_{dry}\right) = \sqrt{\frac{1}{N}\sum_{i=1}^{N}\left(\left(\overline{x}_{dry,\,i}\right)_{num.} - \left(\overline{x}_{dry,\,i}\right)_{an.}\right)^2}, \tag{4.40}$$

with N the number of computational time steps in the dimensionless interval $2 \leq \overline{t} \leq 5$. Despite the halving and the doubling of the grid size, it is confirmed that the analytical drying front lies between the numerical fronts obtained assuming

$\overline{h}_\epsilon$ equal to 10^{-5} and 10^{-4}. Thus, it can be stated that a value of $\overline{h}_\epsilon$ lying in the interval $\left[10^{-5},\ 10^{-4}\right]$ is suitable to achieve a satisfactory tracking of wet/dry interfaces.

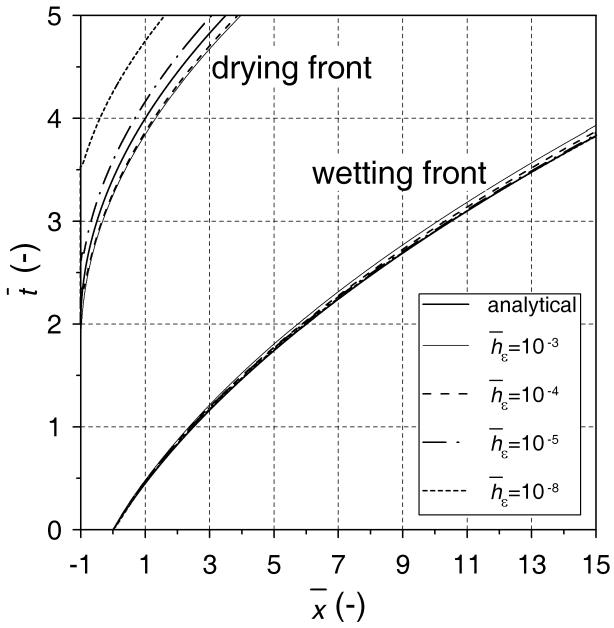

Figure 4.8. Comparison between analytical and numerical solutions of wetting and drying fronts for the dam-break problem in a sloping channel.

Table 4.3. L_2 norms of the drying front positions as function of Δx.

	$L_2\left(\overline{x}_{dry}\right)$		
$\overline{h}_\epsilon$	$\Delta x = 0.05$ m	$\Delta x = 0.1$ m	$\Delta x = 0.2$ m
10^{-5}	0.088 (late)	0.284 (late)	0.584 (late)
10^{-4}	0.135 (advance)	0.256 (advance)	0.176 (advance)

4.3.3 2D periodic motions in a parabolic basin

The capability of the proposed method of providing accurate results in the presence of 2D wetting and drying moving boundaries on non-flat topographies was

verified comparing numerical results with two exact solutions given by Thacker [64], which concern the oscillation of a water volume in a frictionless paraboloidic basin having equation:

$$z = z_0 \left(1 - \frac{x^2 + y^2}{L^2}\right). \tag{4.41}$$

In (4.41) the depth function z is positive below the equilibrium level (Figg.4.9a and 4.11a), z_0 is the depth of the vertex of the paraboloid and L is the radius at $z = 0$.
In the following sections, two cases will be considered, corresponding to particular choices for initial values. In the first (Section 4.3.3) the water body rotates in the basin, maintaining its surface planar and the velocity field uniform, while in the second the water surface is a parabola of revolution which expands and contracts periodically (Section 4.3.3).

Planar water surface

In this case the moving shoreline is a circle of radius L whose center C describes a circle of radius ξ (Fig.4.9a). The equations of this motion are given by [64]:

$$\begin{cases} \eta\,(x, y, t) = 2\xi \dfrac{z_0}{L}\left[\dfrac{x}{L}\cos\omega t - \dfrac{y}{L}\sin\omega t - \dfrac{\xi}{2L}\right] \\ u\,(x, y, t) = -\xi\omega\sin\omega t;\ v\,(x, y, t) = -\xi\omega\cos\omega t, \end{cases} \tag{4.42}$$

where η is the surface elevation, positive above the equilibrium level and $\omega = \sqrt{2gz_0}/L$ is the frequency of the rotation around the centre of the basin. The magnitude of the velocity vectors is constant over time at the value $|\mathbf{V}| = \xi\omega$, whereas the direction rotates over time describing an angle $\alpha = 3\pi/2 - \omega t$ during a period ($0 \le t \le T$). This test is extremely severe for numerical models since a great number of cells is continuously wetted and dried.
The test was performed in a square domain $[-1.6\,\text{m} \le (x, y) \le +1.6\,\text{m}]$ with $z_0 = 0.05$ m, $L = 1$ m and $\xi = 0.5$ m; the basin dimensions are such that the water never reaches the boundaries. The numerical simulation was carried out for four periods with $\Delta x = \Delta y = 0.02$ m and $h_\epsilon = 3 \cdot 10^{-6}$ m. Since the water body remains compact and it intersects sharply the bathymetry, the numerical solution is not particularly sensitive to the threshold value h_ϵ.
Fig.4.9b shows a contour map of the computed results at $t = (15/8)\,T$, when $\alpha = -\pi/4$: the shoreline is still circular, the surface almost perfectly planar and

the velocity field nearly uniform.
Fig.4.10a shows the comparison between numerical and analytical water depths in the last two periods of simulation at points (1.0; 0.0), (0.5; 0.0), (0.4; 0.0). The first point gets wet and dry during the periodic motion, the second gets dry only at $t = (0.5 + n)T$, $(n \in \mathbb{N})$, whereas the third remains wet all the time. An overall quantitative information about the accuracy of the numerical reconstruction is given by L_2 error norms for water depth h, velocity magnitude $|\mathbf{V}|$ and direction α estimated as follows:

$$\begin{aligned} L_2(h) &= \frac{1}{\overline{h}_{an.}(t)} \sqrt{\frac{\sum_{i=1}^{N_{wet}} \left((h_i)_{num.} - (h_i)_{an.}\right)^2}{N_{wet}}}, \\ L_2(|\mathbf{V}|) &= \frac{1}{|\mathbf{V}|_{an.}} \sqrt{\frac{\sum_{i=1}^{N_{wet}} \left((|\mathbf{V}|_i)_{num.} - |\mathbf{V}|_{an.}\right)^2}{N_{wet}}}, \\ L_2(\alpha) &= \frac{1}{\pi} \sqrt{\frac{\sum_{i=1}^{N_{wet}} \left((\alpha_i)_{num.} - \alpha_{an.}\right)^2}{N_{wet}}}, \end{aligned} \tag{4.43}$$

where N_{wet} is the total number of wet cells and $\overline{h}_{an}(t)$ is the average water depth, in this case not depending on time and equal to $z_0/2$. The trend of the norms during the last two simulation periods is shown in Fig.4.10b. The error on the velocity norm and on the direction α are mainly due to the cells close to the shoreline: here water depths become very small and the derived variables u and v, obtained by dividing unit discharges by water depth, can assume slightly incorrect values. At the end of four simulation periods, the volume error (relative to the volume at $t = 0$) is about $5 \cdot 10^{-7}$. This residual error is due to a few cells on the shoreline in which the water depth remains less than h_ϵ after the iterative procedure and then is set at zero. If a pure SGM reconstruction is performed, spurious oscillations caused by unreliable extrapolations at wet-dry interfaces grow in time and the simulation crashes.

Curved water surface

The second exact solution analyzed concerns the periodic motion of a circular paraboloidic water volume initially at rest and subject to gravity (Fig.4.11a).

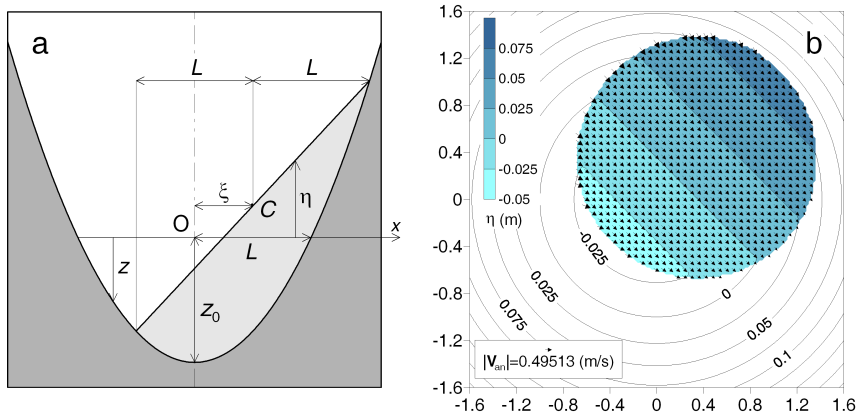

Figure 4.9. (a) Definition sketch for the Thacker test with planar water surface [64]; (b) contour map of the numerical results at $t = 15/8\,T$.

The equations of the motion are [64]:

$$\begin{cases} \eta\left(x,y,t\right) = z_0 \left\{ \dfrac{\sqrt{1-A^2}}{1-A\cos\omega t} - 1 - \dfrac{x^2+y^2}{L^2}\left[\dfrac{1-A^2}{\left(1-A\cos\omega t\right)^2} - 1\right]\right\} \\ u\left(x,y,t\right) = \dfrac{1}{1-A\cos\omega t}\left(\dfrac{1}{2}\omega x A\sin\omega t\right) \\ v\left(x,y,t\right) = \dfrac{1}{1-A\cos\omega t}\left(\dfrac{1}{2}\omega y A\sin\omega t\right), \end{cases} \tag{4.44}$$

where the frequency ω and the parameter A are:

$$\omega = \frac{\sqrt{8gz_0}}{L}, \quad A = \frac{\left(z_0+\eta_0\right)^2 - \left(z_0\right)^2}{\left(z_0+\eta_0\right)^2 + \left(z_0\right)^2}. \tag{4.45}$$

According to (4.44), the surface remains a parabola of revolution during the motion and the water body moves away from the center in the first half of the period T and then converges towards in the second half. Moreover, at times:

$$t^* = nT \pm \frac{1}{\omega}\arccos\left(\frac{1-\sqrt{1-A^2}}{A}\right), \quad n \in \mathbb{N} \tag{4.46}$$

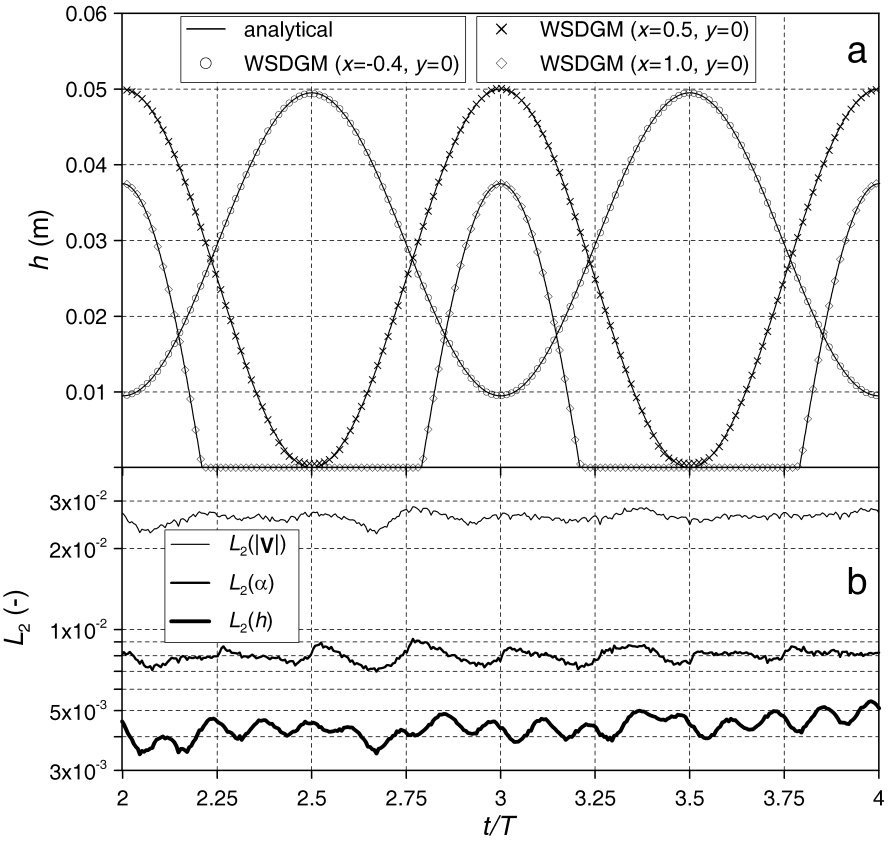

Figure 4.10. Thacker test with planar surface: (a) comparison between analytical and numerical results for water depth h; (b) L_2 norms for h, $|\mathbf{V}|$ and α.

all the terms between curly brackets in (4.44) vanish, so the paraboloidic water surface degenerates in a planar surface with $\eta(x, y, t^*) = 0$.
Due to the large variation over time of the number of wet cells, this problem is extremely severe for numerical models, too. The test was performed in a square domain $[-1.75\,\text{m} \leq (x, y) \leq +1.75\,\text{m}]$ with $z_0 = 0.05$ m, $L = 1$ m and $\eta_0 = 0.10$ m; with the assumed parameters the radius of the shoreline at the maximum expansion ($t = (0.5 + n)\,T,\ n \in \mathbb{N}$) is $R_{max} = \sqrt{3}$ m and the boundaries of the domain are never reached by the water body. The numerical simulation was carried out for four periods with $\Delta x = \Delta y = 0.02$ m and $h_\epsilon = 5 \cdot 10^{-6}$ m.
Fig.4.11b shows slices along the x axis of numerical results and analytical solution at some selected times. A moderate underestimation of the water depth occurs near the center after four periods.
Fig.4.12a,b shows the comparison between numerical and analytical solution for water depth h and velocity component u at points (0.0; 0.0), (0.5; 0.0), (0.7; 0.7). The first two points remain wet all the time, whereas the third gets wet and dry during the periodic motion. Small local differences with the analytical solution are shown more clearly in the insets, where all the computational points are reported.
The L_2 norm of h (Fig.4.12c) was evaluated according to (4.43), where the average water depth $\overline{h}_{an}(t)$ is equal to $(h(0, 0, t) - z_0)/2$. Since the velocity field vanishes at $t = n/2\,T,\ n \in \mathbb{N}$, $L_2(|\mathbf{V}|)$ was normalized by the analytical velocity magnitude at the shoreline at $t = t^*$.
Although the mass error (with respect to the mass at $t = 0$) slightly increases over time for the reason explained in Sec. 4.3.3, after four simulation periods the introduction of the flux correction procedure yields to obtain a relative mass error of about $6 \cdot 10^{-8}$ without corrupting the tracking of wet/dry fronts; if the flux correction is not applied the error is about 0.01. Like in the previous case, if pure SGM extrapolations are performed, the numerical simulation crashes due to spurious oscillations close to the shoreline.

4.3.4 Circular dam-break on a non-flat bottom

This test was developed by the authors themselves in order to study the flow consequent to the sudden collapse of an idealized circular dam placed on a non horizontal bottom. A cylindrical water volume of radius $R_0 = 10$ m is initially placed in a circular domain of radius $R = 25$ m centered in $(x = 0, y = 0)$. The

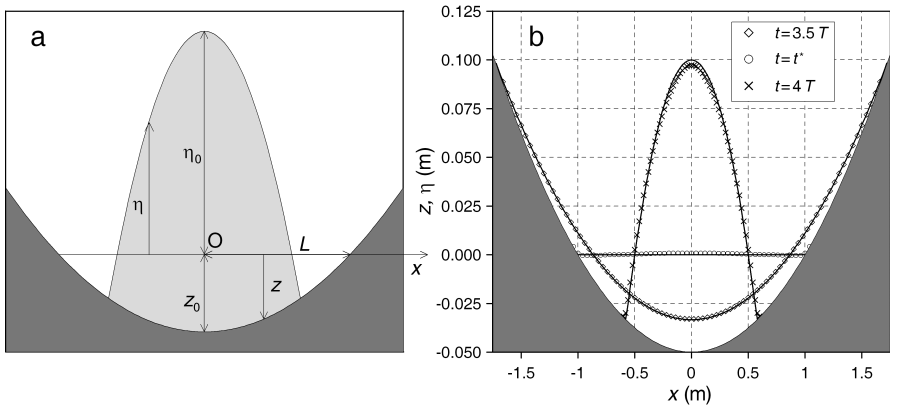

Figure 4.11. (a) Definition sketch for the Thacker test with curved water surface [64]; (b) slices of numerical results and analytical solution at some selected times.

bottom profile is described by the following equation:

$$z\left(r\right)=0.5\left[1+\cos\left(\frac{2\pi}{5}r\right)\right], \tag{4.47}$$

where $r=\sqrt{x^2+y^2}$ is the radius.
As initial conditions it is assumed:

$$\begin{array}{ll}\eta\left(r,0\right)=10\,\mathrm{m} & \text{if } 0\leq r\leq R_0\\ h\left(r,0\right)=0\,\mathrm{m} & \text{if } R_0<r\leq R\\ u_r\left(r,0\right)=0\,\mathrm{m/s} & \text{everywhere.}\end{array} \tag{4.48}$$

At the circular boundary a reflective condition is imposed.
Since the problem has a cylindrical symmetry, an inhomogeneous set of 1D differential equations can be derived along r [67]:

$$\frac{\partial\mathbf{U}}{\partial t}+\frac{\partial\mathbf{F}\left(\mathbf{U}\right)}{\partial r}=\mathbf{S}_r\left(\mathbf{U}\right)+\mathbf{S}_0\left(\mathbf{U}\right), \tag{4.49}$$

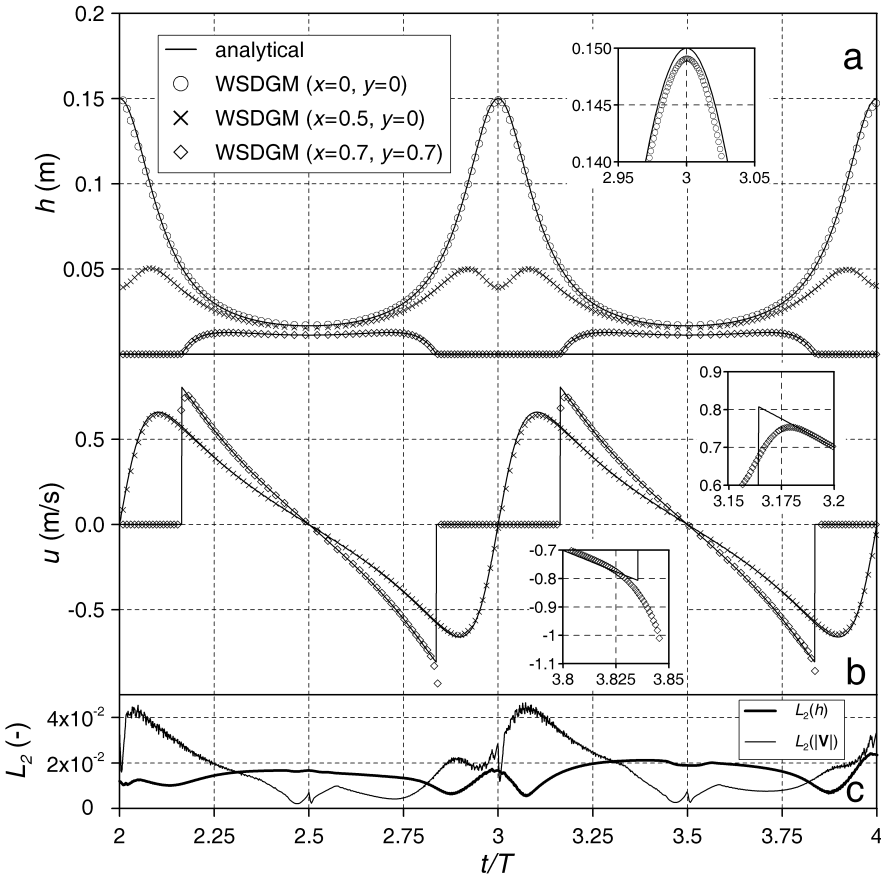

Figure 4.12. Thacker test with curved water surface: comparison between analytical and numerical results for (a) water depth h and (b) velocity component u. (c) L_2 error norm for water depth h.

where

$$\begin{aligned} &\mathbf{U} = [h,\ u_r h]^T, && \mathbf{F}(\mathbf{U}) = \left[hu_r,\ hu_r^2 + \frac{1}{2}gh^2\right]^T, \\ &\mathbf{S}_r(\mathbf{U}) = -\frac{1}{r}\left[hu_r,\ hu_r^2\right]^T, && \mathbf{S}_0(\mathbf{U}) = -gh\left[0,\ \frac{\partial z(r)}{\partial r}\right]^T. \end{aligned} \tag{4.50}$$

In (4.50) $u_r = u_r(r,t)$ is the radial velocity, $\mathbf{S}_r(\mathbf{U})$ is the source term induced by the metrics and $\mathbf{S}_0(\mathbf{U})$ is the source term due to the non-flat bottom. A reliable approximation of the exact solution was obtained numerically solving the 1D problem (4.49) on a very fine mesh ($\Delta r = 0.005$ m). The reference solution was computed by means of the same WSDGM in which the unsplit centered discretization of $\mathbf{S}_0$ allows the satisfaction of the *C-property*, while the splitting of $\mathbf{S}_r$, discretized with a pointwise approach, completes the updating of the conserved variables. In the 2D simulation the computational domain was discretized through a square grid of 0.25 m; the wet/dry tolerance h_ϵ was set at 10^{-4} m.
Fig.4.13 shows 2D numerical solutions profiles of water level and velocity along $\theta = 0$ ($y = 0$) and $\theta = \frac{\pi}{4}$ ($y = x$) at some selected times compared to the 1D profiles computed on the finer mesh.
At $t = 0.6$ s the ability of WSDGM to preserve the static condition can be appreciated. At $t = 2$ s and $t = 6$ s the shock wave coming from the boundary is moving toward the center, whereas at $t = 8$ s the same shock has already passed through the focusing point at $r = 0$ and it is now expanding outwards.
The 2D numerical solution is able to reproduce the complex structures induced by the non flat bottom and by the reflection against the lateral circular wall. The radial symmetry is well maintained as can be appreciated from Fig.4.13 and Fig.4.14, which shows the contour map of the numerical water surface level at $t = 2$ s.
In Fig.4.15 the numerical results obtained adopting $\mathrm{Fr}_{\mathrm{lim}} = 0$ confirms that a pure DGM reconstruction can not maintain the static condition of flow at rest if a centered discretization for the bed slope source term is applied.
If a pure SGM reconstruction is adopted ($\mathrm{Fr}_{\mathrm{lim}} \to \infty$) the scheme does not work at all, due to bad extrapolations at wet/dry interfaces.

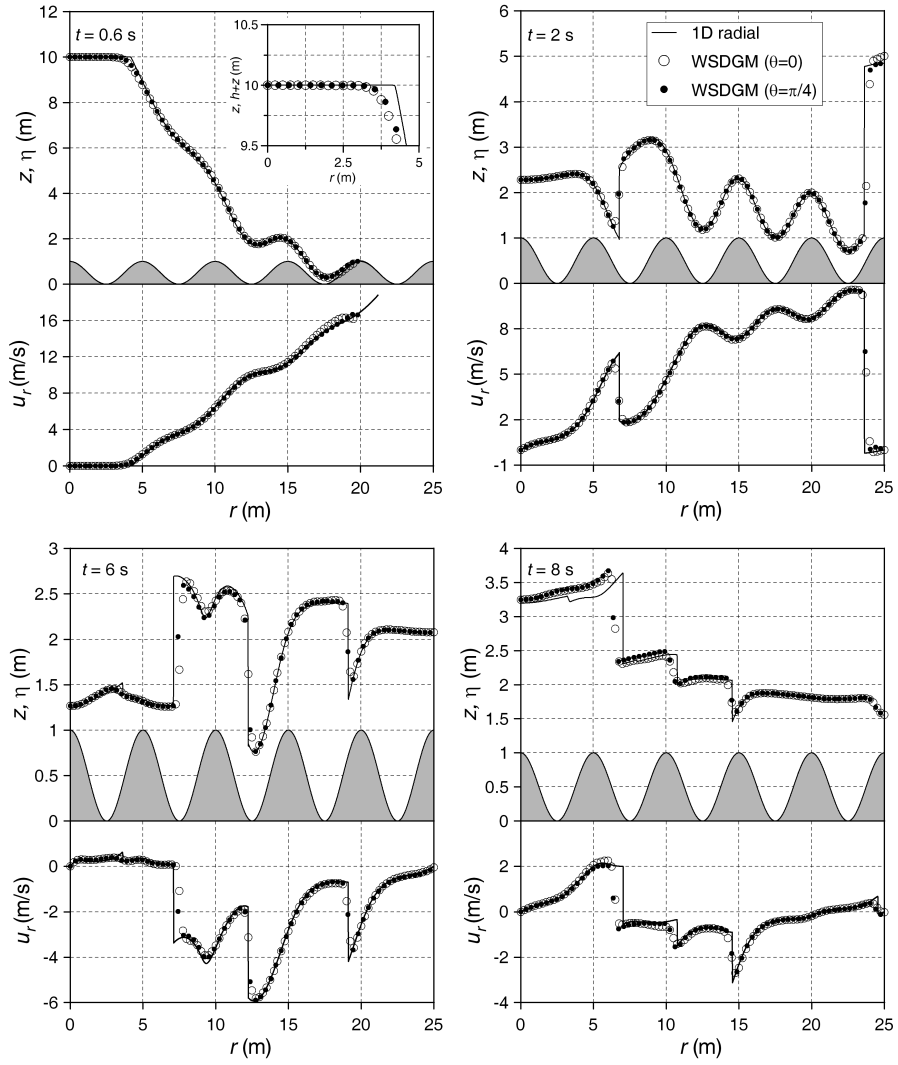

Figure 4.13. Circular dam-break on non flat bottom: comparison between 2D WSDGM ($\mathrm{Fr}_{\mathrm{lim}} = 2$) results and 1D radial reference solution for water surface level and velocity along axial and diagonal directions.

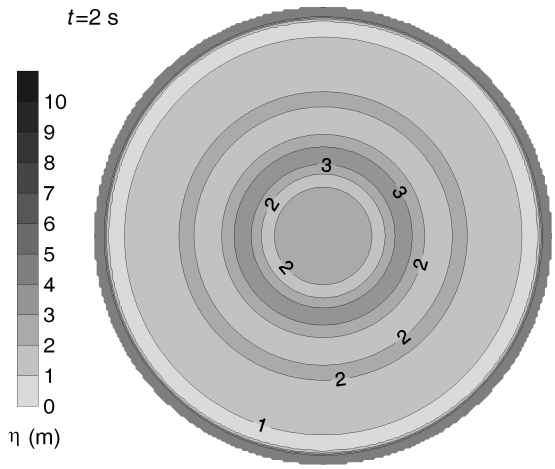

Figure 4.14. Circular dam-break on non flat bottom: contour map of numerical water surface level at $t = 2$ s.

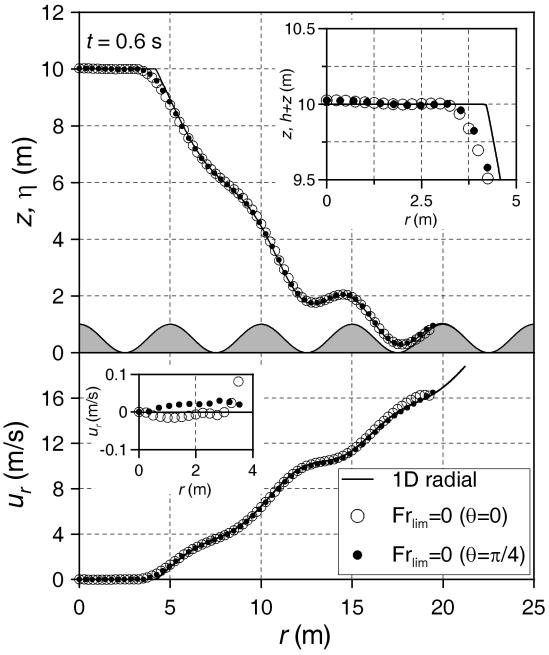

Figure 4.15. Circular dam-break on non flat bottom: comparison between 1D radial reference solution and 2D numerical profiles of water surface level and velocity at $t = 0.6$ s applying a pure DGM recontruction.

Chapter 5

Case Studies

SWE are frequently adopted as the mathematical model for the description of rapidly varying flow phenomena, like catastrophic events due to dam or levee breaking. Numerical modeling is an effective tool for the estimate of the main flood characteristics (area extent, maximum water depth and velocity, arrival time of the wetting front) required for the hydraulic hazard assessment.
With the purpose of testing the applicability of the proposed WSDGM scheme on real case studies, in this Chapter the numerical results concerning the hypothetical collapse of two dams placed in the Northern Italy are presented.
Although experimental data are not available to perform a comparison with WSDGM results, these field-scale applications are severe numerical tests, in which the treatment of both bed slope and friction source terms must be suitable to deal with strongly irregular topographies and non-zero bed resistance.
Although the Froude number at wet/dry interfaces is reduced by friction and finite volume discretization, it was verified that the choice of the parameter $\mathrm{Fr}_{\mathrm{lim}} = 2$ guarantees an essentially DGM-behavior at moving fronts also in these practical applications.

5.1 Hypothetical collapse of the dam on Parma river

The dam (Fig.5.1), built in 2005 for flood protection, is located about 10 km upstream from the city of Parma. The reservoir has a storage capacity of about $12 \cdot 10^6$ m^3 and the maximum water depth with reference to the bottom of the stilling basin is 16.4 m.

The DEM of the whole area of interest was reconstructed on a square mesh

Figure 5.1. Picture of the dam on Parma river taken in 2006.

of size 10 m through an interpolation of data acquired from the available cartography. Figure 5.2 illustrates the contour map of the area together with the different conditions imposed at the boundaries. The reflective condition in the north-eastern limit simulates the presence of a road embankment; it was verified *a posteriori* that the condition to impose on the western and southern boundaries is not important, since the flooding does not reach these areas.
As initial condition, the water surface level corresponding to the maximum retaining depth (105.6 m u.s.l.) was imposed in the reservoir. The Manning roughness coefficient was set at 0.03 $\mathrm{s} \cdot \mathrm{m}^{-1/3}$ in the river and 0.05 $\mathrm{s} \cdot \mathrm{m}^{-1/3}$ elsewhere, the wet/dry tolerance h_ϵ was set at 10^{-3} m and the FORCE method was used to compute numerical fluxes.

As can be seen from the flow field at two minutes after breaking (Fig.5.3), WSDGM is able to preserve the static condition in the region not yet reached by the rarefaction wave. In Fig.5.4 water stage contour maps resulting from the numerical modeling at four selected times are shown as an example.

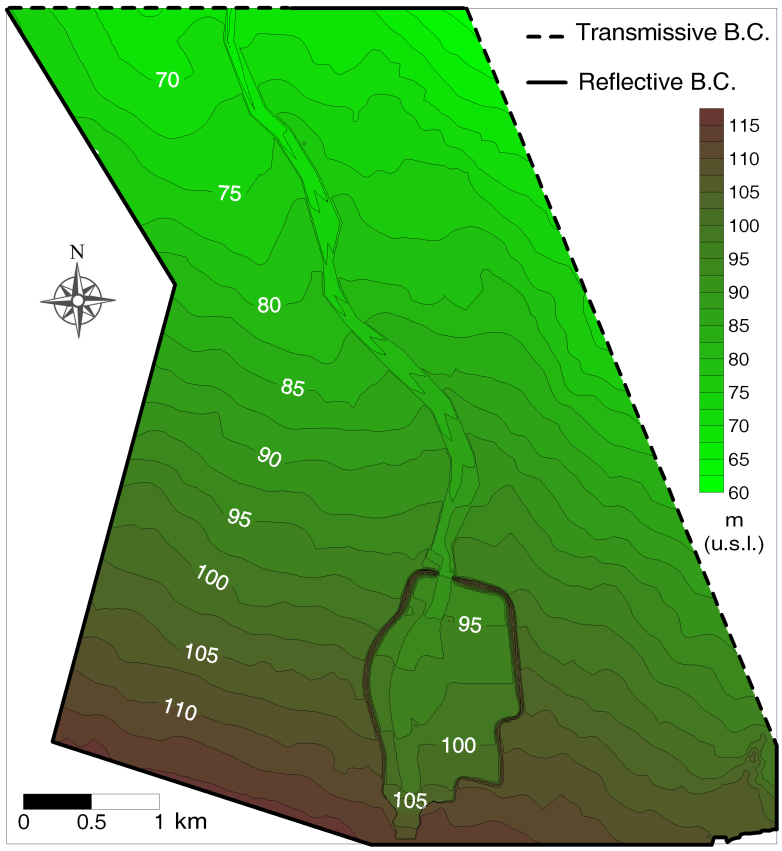

Figure 5.2. Hypothetical collapse of the dam on Parma river: contour map of the area under investigation.

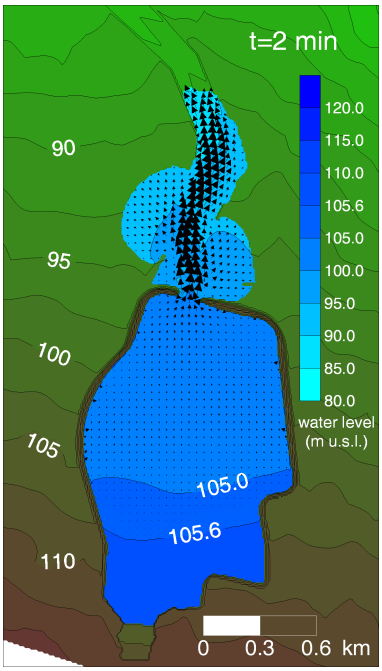

Figure 5.3. Hypothetical collapse of the dam on Parma river: flow field 2 minutes after the breaking.

Thanks to the flux correction introduced in Section 3.2.5, 30 minutes after the breaking the relative mass error is limited to the negligible value of $3 \cdot 10^{-4}$.

5.2 Hypothetical collapse of the Mignano dam

The Mignano dam (Fig.5.5) is a gravity concrete structure built in 1926-1933 for irrigation purposes [2]; it is placed in the Northern Italy in the upper reach of the Arda river, a right tributary of the Po river. The dam is characterized by a maximum retaining depth of about 45 m and a total storage capacity of $16 \cdot 10^6$ m^3; in Table 5.1 the main geometric features of the barrage and the reservoir are summarized.

The topographic information necessary to describe the potentially floodable

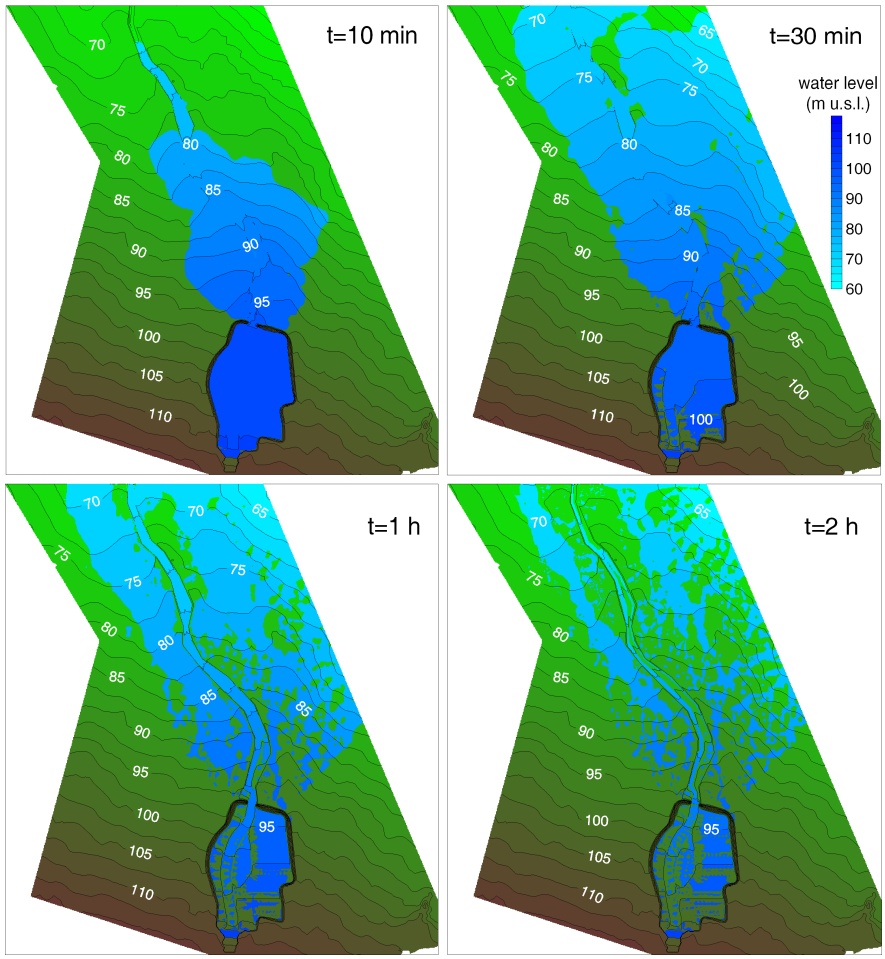

Figure 5.4. Hypothetical collapse of the dam on Parma river: water stage contour maps at different times after the breaking.

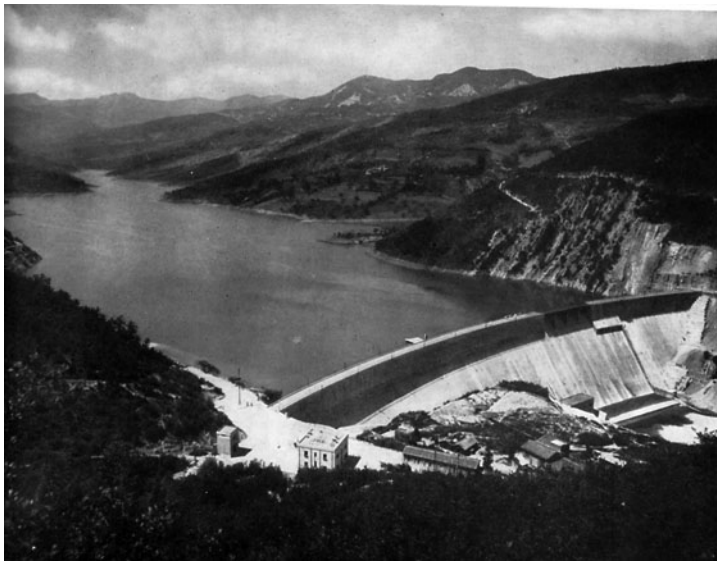

Figure 5.5. Picture of the Mignano dam taken in 1953 (in [2]).

Table 5.1. Main features of the Mignano Dam.

Crest lenght	341 m
Height (above ground)	51 m
Dam crest elevation	342 m u.s.l.
Storage capacity	$16 \cdot 10^6$ m^3
Reservoir surface area	0.80 km^2
Maximum storage level	340.5 m u.s.l.
Spillway crest elevation	337.8 m u.s.l.
River basin extension	0.80 km^2

area was obtained joining the aero-photogrammetric data of the reservoir and the adjacent zones (data collected on 2003 during the emptying of the lake) and the data extracted from the available topographical maps. Trough a suitable interpolation of this information a uniform DTM (Fig.5.6) with square elements of side 25 m was obtained; this grid size is a reasonable compromise between a fair computational efficiency and a satisfactory modeling of topographic peculiarities of the region under investigation.
The boundaries of the studied area were assumed as solid and insuperable, since the Arda valley border is 75 m higher than the river thalweg and the plain is bounded by a road and a rail embankment. Both these assumptions were validated and confirmed *a posteriori* after the simulation of the flooding dynamics.

In order to evaluate the effects of the grid size especially on the discharge hydrographs at the dam site, a finer grid of 5 m was interpolated from the reference one, covering only the reservoir and the area immediately downstream the dam.
The roughness coefficient is another factor of influence for the flood dynamics, so it must be properly estimated for the area of interests. The absence of historical documentation did not allow to perform any calibration for the value of the Manning coefficient n; for this reason values derived from previous studies on neighboring similar regions were adopted, namely $n = 0.06\ \mathrm{s \cdot m^{-1/3}}$ for the valley and $n = 0.04\ \mathrm{s \cdot m^{-1/3}}$ for the alluvional fan and the plain. A sensitivity analysis for testing the influence of this parameter was performed halving the Manning coefficient values.
Further aspects influencing the inundation, at least on initial stages, are the typology and the dynamics of the collapse. Technical rules concerning masonry dams enforces to consider the break as total and sudden: therefore, in the scenario assumed as the reference one, such a collapse was hypothesized. Moreover, in order to point out the role played by the breach dimension, a partial failure of more than one third of the structure length was modeled, according to the Italian rules about concrete gravity dams.
Considering all the parameters mentioned above, five different scenarios, whose features are summarized in Table 5.3, can be distinguished. For all the scenarios, the initial conditions of water at rest at the maximum storage level in the reservoir and zero water depth and velocity elsewhere were imposed. The numerical simulations were extended in time till four hours after the breaking, when the flooding exhausted its catastrophic effect; the parameters $\mathrm{Cr} = 0.8$ and $h_\epsilon = 2 \cdot 10^{-3}$ m were adopted. The numerical fluxes were computed by HLLC approximate Riemann solver; the second order *Strang Splitting* algorithm for the updating of the solution in time was applied.

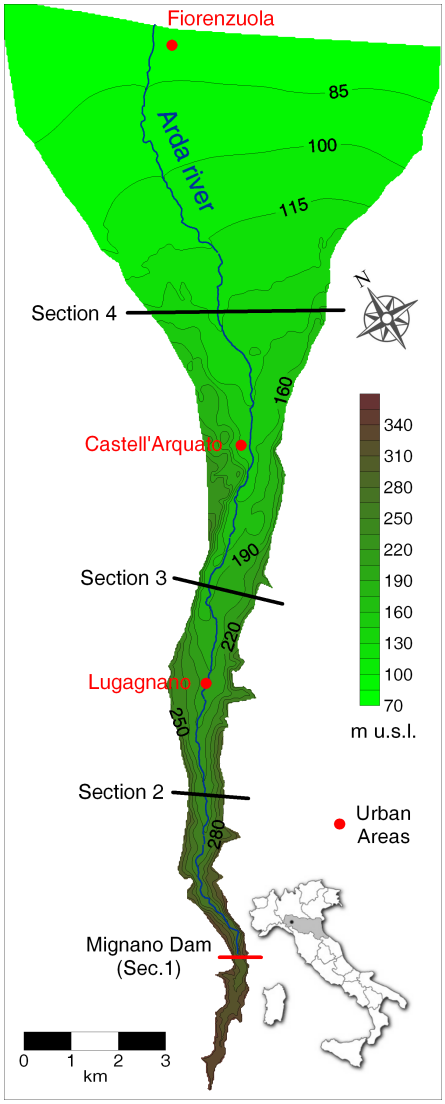

Figure 5.6. Hypothetical collapse of the Mignano dam: contour map of the area under investigation.

Table 5.2. Main features of the considered scenarios.

Scenario Nr.	Break Type	Grid Size (m)	Manning Coeff. ($s \cdot m^{-1/3}$)
1	total	25	$0.06 - 0.04$
2	total	5	$0.06 - 0.04$
3	total	25	$0.03 - 0.02$
4	partial	25	$0.06 - 0.04$
5	partial	5	$0.06 - 0.04$

The attribution of a hydraulic hazard level to the areas potentially floodable is a fundamental requirement for the river basin management and the development of emergency action plans; at this purpose the total depth D is adopted as the global risk index. This quantity is expressed by:

$$D^2 = h^2 + 2\frac{q^2}{gh}, \tag{5.1}$$

where q is the unit-width discharge; after some mathematical manipulations one obtains:

$$D = h\sqrt{1 + 2\mathrm{Fr}^2}. \tag{5.2}$$

In (5.2) D represents the equivalent water depth at rest producing a static force equal to the total force of the flow and summarizes the contribution of static force and momentum flux of the flow. This index is particularly significant for rapidly varying phenomena, in which the arrival time of the wetting front is so fast to be an information not as relevant as maximum water depths and velocities.
In order to give an effective and concise information about the spatial distribution of D for Scenarios 1, 3 and 4, flooded areas against total depths are represented in Fig.5.7. The total extension of the flooded area after four hours of simulation is about 12.5 km^2 almost independently from the scenario considered. The 85% of the region involved by the flooding is characterized by a total depth greater than 2 m, that could be considered as the threshold level of danger for human life. As shown by the good agreement between curves referred to Scenarios 1 and 3 for $D > 4$ m, the roughness coefficient does not sensibly influence the extension of the areas characterized by high values of D. Even though the partial failure preserves from inundation some zones located in the upper reach of the Arda valley immediately downstream the dam, the total flooding extension is not significantly influenced by a reduced breach width.

The contour map of the maximum total head D computed for Scenario 1 (Fig.5.8) gives a more detailed information of the hydraulic hazard spatial distribution. All the Arda valley is characterized by a very high hazard factor ($D > 5$ m) and just in a small portion located in the plain the total depth is less than 2 m.

In Fig.5.9 the discharge hydrographs at the four sections reported in Fig.5.6

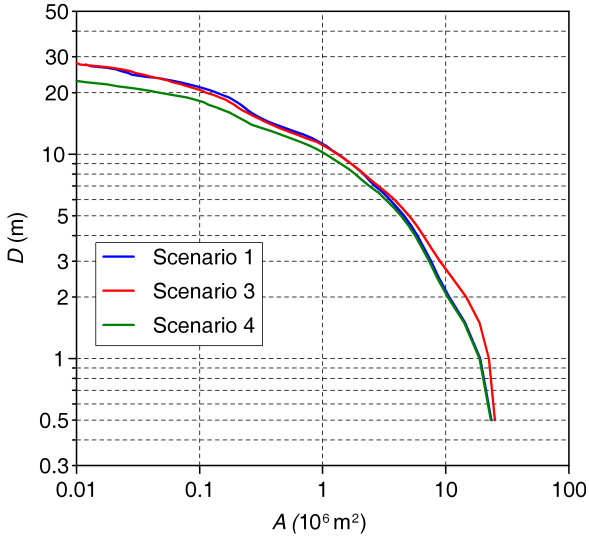

Figure 5.7. Hypothetical collapse of the Mignano dam: total depth against flooded area.

are shown. At the dam section, the maximum discharge referred to Scenario 1 is about $47 \cdot 10^3$ m^3/s and the reservoir empties in about 20 minutes. The results obtained refining the grid spacing (Scenario 2) are not sensibly different from those obtained with the coarser grid (Scenario 1); the peak values, the oscillations immediately after the collapse and the exhaustion times are in good agreement. Hence, the reference grid size of 25 m is suitable to describe the total dam-break phenomenon. As expected, a halved bed roughness coefficient (Scenario 3) does not influence the dynamics immediately after the breaking, but at 30 s $< t <$ 5 min it produces higher discharge values than reference ones. The peak value of the hydrograph referred to a partial failure (Scenario 4) is

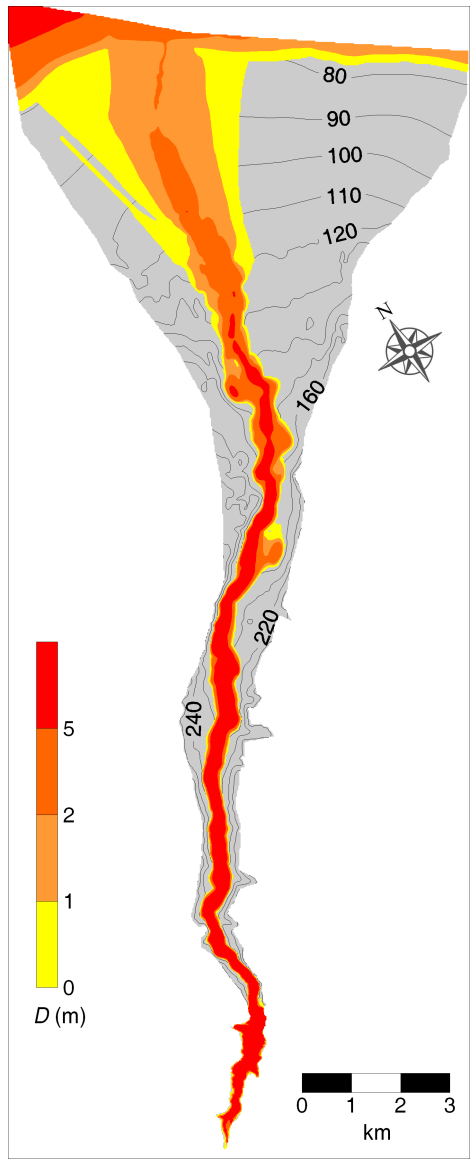

Figure 5.8. Hypothetical collapse of the Mignano dam: contour map of the maximum total depth D for Scenario 1.

reduced of about 30% with respect to the total break and, a consequence, the emptying time of the reservoir is longer. The differences between the results obtained adopting a 5 m (Scenario 5) and a 25 m (Scenario 4) mesh show how the coarser value is not suitable to descibe a partial break.
Looking at the hydrographs at Sections 2, 3 and 4 and referring to Scenario 1, a progressive reduction in the maximum discharge value can be seen. This routing effect is reduced if a lower bed roughness coefficient is adopted (Scenario 3): moving downstream the peak values are increasingly high and anticipated than those obtained with the reference value of n (Scenarios 1 and 2). The hydrographs referred to a partial breach width (Scenario 4) show lower and delayed maximum discharge values in the upper and medium part of the Arda valley (Section 2 and 3), but in the plain (Section 4) peak values and times are comparable with those obtained in Scenario 1.

The water level hydrographs, evaluated at the urban areas indicated in Fig.5.6, are reported in Fig.5.10. The maximum water depth is very high at Lugagnano and Castell'Arquato (about 7 m), while it is less than 1 m at Fiorenzuola, in the plain. The partial breach width (Scen.4), which greatly influences the flooding dynamics in the areas immediately downstream the dam, does not cause great variations in water depths with respect to those obtained considering a total failure (Scen.1). The results referred to Scenario 3 show that a smaller Manning coefficient anticipates the maximum of water depth and, in the lower part of the valley (Castell'Arquato and Fiorenzuola), the peak value is slightly smaller than the reference one (Scen.1).

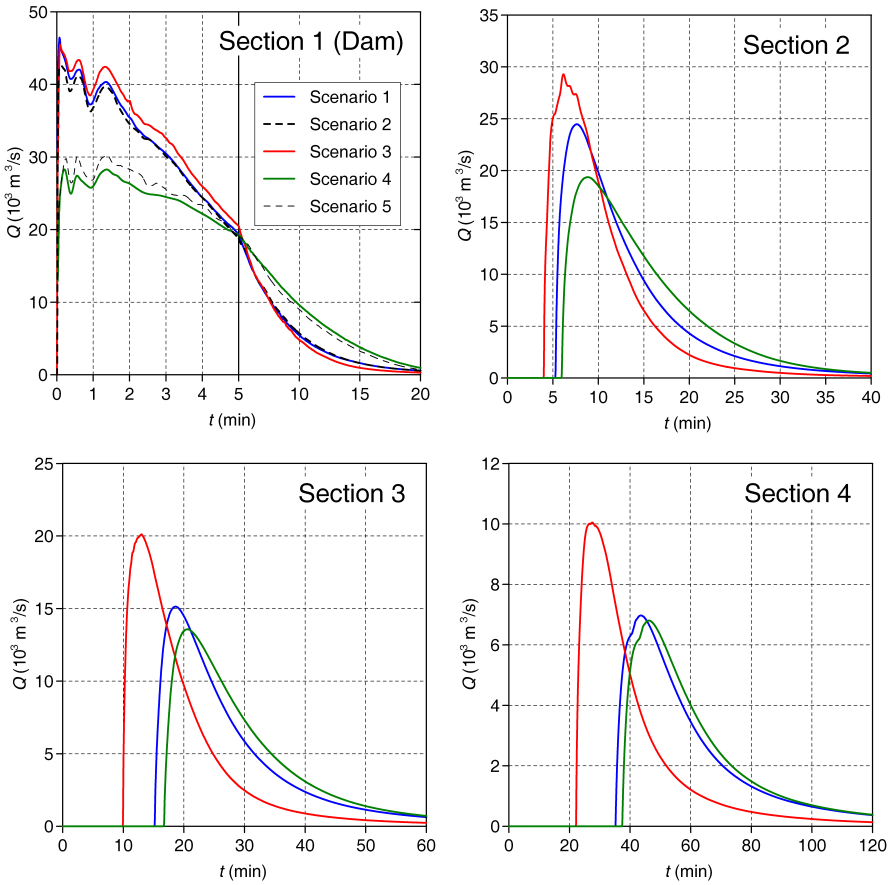

Figure 5.9. Hypothetical collapse of the Mignano dam: discharge hydrographs at the studied sections.

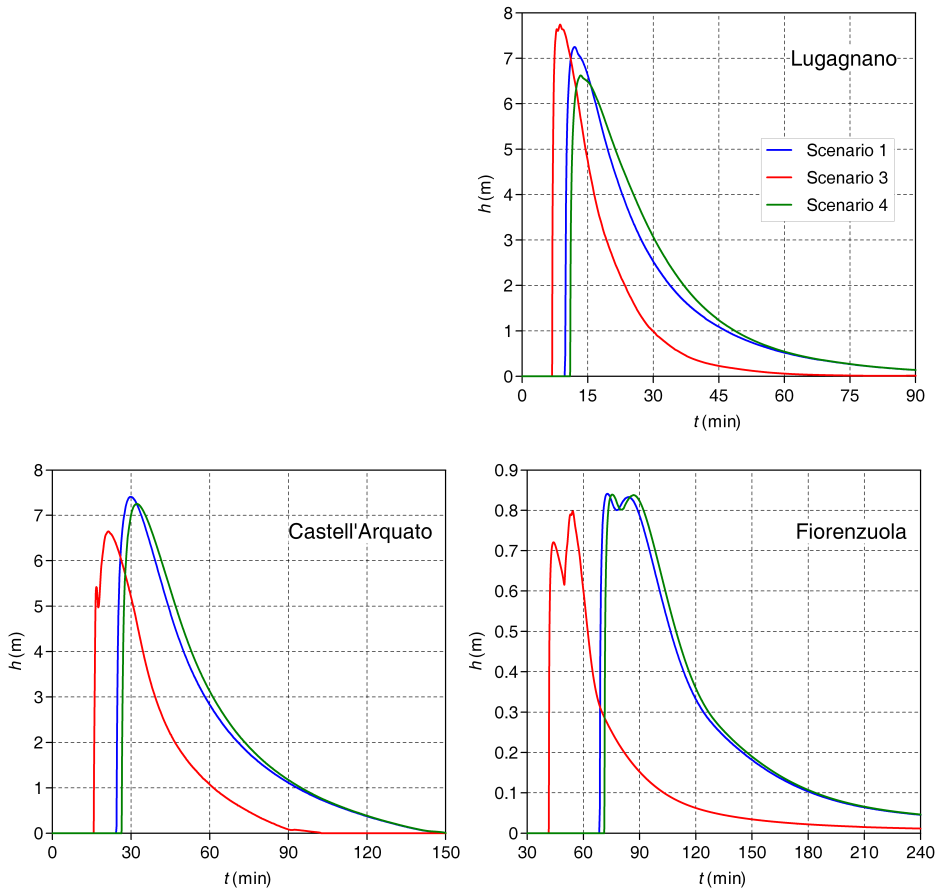

Figure 5.10. Hypothetical collapse of the Mignano dam: water level hydrographs at the studied urban areas.

Chapter 6

Conclusions

In this thesis a finite volume MUSCL-type scheme for the numerical solution of 2D shallow water equations was presented. The *Weighted Surface-Depth Gradient Method* (WSDGM) computes water depth at the cell boundaries through a weighted average, based on the local Froude number, of the extrapolated values deriving from DGM and SGM reconstructions. In particular the scheme applies a pure SGM reconstruction in static conditions when $\mathrm{Fr} = 0$, and a pure DGM reconstruction when Fr is greater than an upper limit $\mathrm{Fr}_{\mathrm{lim}}$. This value was set at 2 after a sensitivity analysis performed in Section 4.1. The WSDGM reconstruction enables the scheme to perform a robust tracking of wet/dry fronts and, together with an unsplit centered discretization of the bed slope source term, to maintain the static condition on non-flat topographies (*C-property*).
A flux correction applied to shoreline cells with water depth lower than a threshold value drastically reduces the mass error without corrupting the wet/dry front tracking.
WSDGM was validated through its application to a set of severe reference tests involving high bed slopes, 1D and 2D wet/dry fronts. The comparison between reference and numerical results proved that WSDGM provides more accurate solutions than those obtained applying pure SGM or DGM reconstructions. Moreover, the simulation of two dam-break events confirmed the applicability of WSDGM also for practical purposes. Thanks to the flux correction procedure the mass error is limited to very small values, despite the presence of wide fronts induced by a jagged terrain. The scheme allows the evaluation of some characteristic quantities, like maximum water depths and velocities, necessary to attribute a hydraulic hazard to regions potentially floodable. Thus, WSDGM is an effective tool that can be adopted for planning ahead in the case of catastrophic events.

The treatment of bed slope source term and wet/dry fronts is still a challenge in shallow water modeling through Godunov-type methods [69]. My research activity will go on trying to deep these aspects, which are of great interest in field-scale applications.
According to the recent technique proposed by Valiani and Begnudelli [74], the contribution due to bottom slope can be expressed in divergence form, similarly to numerical fluxes. This method is attractive both for its simplicity and the capability of satisfying the *C-property* on non-Cartesian grids, too.
The source term discretization proposed in [74] was preliminary implemented in WSDGM and showed accurate and promising results; nevertheless, the static condition of water at rest cannot be maintained in partially wet cells. The treatment of partially wet elements in two dimension is not trivial, but the possibility of considering a grid element as partially filled (and not completely wet or completely dry) would avoid many numerical instabilities close to dry fronts. A further improvement would be the adoption of an unstructured mesh which allows a more versatile and accurate discretization of the computational domain.

Appendix A

Conservation property

According to the static problem

$$\eta\left(x,t\right)=\overline{\eta},\quad u\left(x,t\right)=0,\quad v\left(x,t\right)=0, \tag{A.1}$$

it results:

$$\left.\begin{array}{l}\mathrm{Fr}_i=0\\ \vartheta_i\left(\mathrm{Fr}\right)=0\end{array}\right\}\ \forall\, i \tag{A.2}$$

and, as a consequence, a pure SGM reconstruction is performed on every cell. The mathematical proof that WSDGM exactly satisfies the *C-property* is carried out considering that FORCE flux is applied. Without loss of generality, only the one dimensional situation is here considered.

1. Data reconstruction.

$$\begin{array}{ll}\eta^L_{i-\frac{1}{2}}=\eta^R_{i-\frac{1}{2}}=\overline{\eta}, & \eta^L_{i+\frac{1}{2}}=\eta^R_{i+\frac{1}{2}}=\overline{\eta},\\ uh^L_{i-\frac{1}{2}}=uh^R_{i-\frac{1}{2}}=0, & uh^L_{i+\frac{1}{2}}=uh^R_{i+\frac{1}{2}}=0.\end{array} \tag{A.3}$$

   Being

$$\begin{array}{ll}h^L_{i-\frac{1}{2}}=\overline{\eta}-z_{i-\frac{1}{2}}, & h^R_{i-\frac{1}{2}}=\overline{\eta}-z_{i-\frac{1}{2}},\\ h^L_{i+\frac{1}{2}}=\overline{\eta}-z_{i+\frac{1}{2}}, & h^R_{i+\frac{1}{2}}=\overline{\eta}-z_{i+\frac{1}{2}},\end{array} \tag{A.4}$$

with

$$z_{i-\frac{1}{2}} = \frac{z_{i-1} + z_i}{2}, \qquad z_{i+\frac{1}{2}} = \frac{z_i + z_{i+1}}{2}, \tag{A.5}$$

it results

$$h^L_{i-\frac{1}{2}} = h^R_{i-\frac{1}{2}}, \qquad h^L_{i+\frac{1}{2}} = h^R_{i+\frac{1}{2}}. \tag{A.6}$$

2. Evolution of extrapolated values over time.

$$\overline{\mathbf{U}}^R_{i-\frac{1}{2}} = \mathbf{U}^R_{i-\frac{1}{2}} - \frac{1}{2}\frac{\Delta t}{\Delta x}\left(\mathbf{F}^L_{i+\frac{1}{2}} - \mathbf{F}^R_{i-\frac{1}{2}}\right) + \frac{\Delta t}{2}\mathbf{S}_{0,\,i} \tag{A.7}$$

Considering the first component of $\overline{\mathbf{U}}^R_{i-\frac{1}{2},j}$:

$$\overline{h}^R_{i-\frac{1}{2}} = h^R_{i-\frac{1}{2}} - \frac{1}{2}\frac{\Delta t}{\Delta x}\left(uh^L_{i+\frac{1}{2}} - uh^R_{i-\frac{1}{2}}\right) \tag{A.8}$$

from Eq.(A.3) results:

$$\overline{h}^R_{i-\frac{1}{2}} = h^R_{i-\frac{1}{2}}. \tag{A.9}$$

For the second component of $\overline{\mathbf{U}}^R_{i-\frac{1}{2}}$:

$$\begin{aligned}
\overline{uh}^R_{i-\frac{1}{2}} &= uh^R_{i-\frac{1}{2},j} - \frac{1}{2}\frac{\Delta t}{\Delta x}\left[\frac{1}{2}g\left(h^L_{i+\frac{1}{2}}\right)^2 - \frac{1}{2}g\left(h^R_{i-\frac{1}{2}}\right)^2\right] - \\
&- \frac{g}{4}\frac{\Delta t}{\Delta x}\left(h^L_{i+\frac{1}{2}} + h^R_{i-\frac{1}{2}}\right)\left(z_{i+\frac{1}{2}} - z_{i-\frac{1}{2}}\right) = \\
&= -\frac{g}{4}\frac{\Delta t}{\Delta x}\left(h^L_{i+\frac{1}{2}} + h^R_{i-\frac{1}{2}}\right)\left[\left(h^L_{i+\frac{1}{2}} - h^R_{i-\frac{1}{2}}\right) + \left(z_{i+\frac{1}{2}} - z_{i-\frac{1}{2}}\right)\right] = \\
&= -\frac{g}{4}\frac{\Delta t}{\Delta x}\left(h^L_{i+\frac{1}{2}} + h^R_{i-\frac{1}{2}}\right)\left(\eta^L_{i+\frac{1}{2}} - \eta^R_{i-\frac{1}{2}}\right) = 0
\end{aligned} \tag{A.10}$$

Similarly for the other extrapolated variables:

$$\overline{h}^L_{i-\frac{1}{2}} = h^L_{i-\frac{1}{2}}, \;\; \overline{uh}^L_{i-\frac{1}{2}} = 0 \tag{A.11}$$

$$\overline{h}^R_{i+\frac{1}{2}} = h^R_{i+\frac{1}{2}}, \;\; \overline{\overline{uh}}^R_{i+\frac{1}{2}} = 0 \tag{A.12}$$

$$\overline{h}^L_{i+\frac{1}{2}} = h^L_{i+\frac{1}{2}}, \;\; \overline{\overline{uh}}^L_{i+\frac{1}{2}} = 0 \tag{A.13}$$

3. Updating of the solution.

$$\mathbf{U}^{n+1}_i = \mathbf{U}^n_i - \frac{\Delta t}{\Delta x}\left(\mathbf{F}_{i+\frac{1}{2}} - \mathbf{F}_{i-\frac{1}{2}}\right) + \Delta t \overline{\mathbf{S}}_{0\,i} \tag{A.14}$$

The updating of the first component h_i is:

$$h^{n+1}_i = h^n_i - \frac{\Delta t}{\Delta x}\left(\mathbf{F}'^{\,force}_{i+\frac{1}{2}} - \mathbf{F}'^{\,force}_{i-\frac{1}{2}}\right). \tag{A.15}$$

where $\mathbf{F}'^{\,force}$ is the first component of the FORCE flux defined as:

$$\mathbf{F}'^{\,force} = \frac{1}{2}\left(\mathbf{F}'^{\,LF} + \mathbf{F}'^{\,RI}\right). \tag{A.16}$$

The first component of the Lax-Friederichs $\mathbf{F}'^{\,LF}_{i+\frac{1}{2},j}$ flux becomes:

$$\begin{aligned} \mathbf{F}'^{\,LF}_{i+\frac{1}{2}} &= \frac{1}{2}\left(\overline{\overline{uh}}^L_{i+\frac{1}{2}} + \overline{\overline{uh}}^R_{i+\frac{1}{2}}\right) + \frac{1}{4}\frac{\Delta x}{\Delta t}\left(\overline{h}^L_{i+\frac{1}{2}} - \overline{h}^R_{i+\frac{1}{2}}\right) = \\ &= \frac{1}{4}\frac{\Delta x}{\Delta t}\left(h^L_{i+\frac{1}{2}} - h^R_{i+\frac{1}{2}}\right) = 0. \end{aligned} \tag{A.17}$$

Defining:

$$\widetilde{uh}_{i+\frac{1}{2}} = \frac{1}{2}\left(\overline{\overline{uh}}^L_{i+\frac{1}{2}} + \overline{\overline{uh}}^R_{i+\frac{1}{2}}\right) + \frac{1}{2}\frac{\Delta t}{\Delta x}\left[\frac{1}{2}g\left(\overline{h}^L_{i+\frac{1}{2}}\right)^2 - \frac{1}{2}g\left(\overline{h}^R_{i+\frac{1}{2}}\right)^2\right], \tag{A.18}$$

it results:

$$\widetilde{uh}_{i+\frac{1}{2}} = \frac{g}{4}\frac{\Delta t}{\Delta x}\left[\left(h^L_{i+\frac{1}{2}}\right)^2 - \left(h^R_{i+\frac{1}{2}}\right)^2\right] = 0. \tag{A.19}$$

The first component of the Richtmeyer flux $\mathbf{F}'^{\,RI}_{i+\frac{1}{2},j}$ flux becomes:

$$\mathbf{F}'^{\,RI}_{i+\frac{1}{2}} = \widetilde{uh}_{i+\frac{1}{2}} = 0; \tag{A.20}$$

then

$$\mathbf{F}^{'\,force}_{i+\frac{1}{2}} = 0. \tag{A.21}$$

Similarly, it results:

$$\mathbf{F}^{'\,force}_{i-\frac{1}{2}} = 0 \tag{A.22}$$

and from (A.15)

$$h_i^{n+1} = h_i^n \tag{A.23}$$

so water depth does not change in time.
The updating of the second component uh_i is:

$$uh_i^{n+1} = uh_i^n - \frac{\Delta t}{\Delta x}\left(\mathbf{F}^{''\,force}_{i+\frac{1}{2}} - \mathbf{F}^{''\,force}_{i-\frac{1}{2}}\right) + \Delta t \overline{\mathbf{S}}^{''}_{0\,i} \tag{A.24}$$

where $\mathbf{F}^{''\,force}$ is the second component of the FORCE flux defined as:

$$\mathbf{F}^{''\,force} = \frac{1}{2}\left(\mathbf{F}^{''\,LF} + \mathbf{F}^{''\,RI}\right). \tag{A.25}$$

The second component of the Lax-Friederichs $\mathbf{F}^{''\,LF}_{i+\frac{1}{2}}$ flux becomes:

$$\begin{aligned}\mathbf{F}^{''\,LF}_{i+\frac{1}{2}} &= \frac{1}{2}\left[\overline{u^2h}^L_{i+\frac{1}{2}} + \frac{1}{2}g\left(\overline{h}^L_{i+\frac{1}{2}}\right)^2 + \overline{u^2h}^R_{i+\frac{1}{2}} + \frac{1}{2}g\left(\overline{h}^R_{i+\frac{1}{2}}\right)^2\right] + \\ &+ \frac{1}{4}\frac{\Delta t}{\Delta x}\left(\overline{uh}^L_{i+\frac{1}{2}} - \overline{uh}^R_{i+\frac{1}{2}}\right) = \\ &= \frac{g}{4}\left[\left(h^L_{i+\frac{1}{2}}\right)^2 + \left(h^R_{i+\frac{1}{2}}\right)^2\right].\end{aligned} \tag{A.26}$$

Defining:

$$\widetilde{h}_{i+\frac{1}{2}} = \frac{1}{2}\left(\overline{h}^L_{i+\frac{1}{2}} + \overline{h}^R_{i+\frac{1}{2}}\right) + \frac{1}{2}\frac{\Delta t}{\Delta x}\left(\overline{uh}^L_{i+\frac{1}{2}} - \overline{uh}^R_{i+\frac{1}{2}}\right) \tag{A.27}$$

it results:

$$\widetilde{h}_{i+\frac{1}{2}} = \frac{1}{2}\left(h^L_{i+\frac{1}{2}} + h^R_{i+\frac{1}{2}}\right). \tag{A.28}$$

The second component of the Richtmeyer flux $\mathbf{F}''^{\,RI}_{i+\frac{1}{2}}$ flux becomes:

$$\begin{aligned}\mathbf{F}''^{\,RI}_{i+\frac{1}{2}} &= \widetilde{u^2 h}_{i+\frac{1}{2}} + \frac{1}{2} g \left(\widetilde{h}^2_{i+\frac{1}{2}}\right) = \\ &= \frac{g}{8}\left(h^L_{i+\frac{1}{2}} + h^R_{i+\frac{1}{2}}\right)^2\end{aligned} \tag{A.29}$$

and then:

$$\begin{aligned}\mathbf{F}''^{\,force}_{i+\frac{1}{2}} &= \frac{g}{2}\left\{\frac{1}{8}\left(h^L_{i+\frac{1}{2}} + h^R_{i+\frac{1}{2}}\right)^2 + \frac{1}{4}\left[\left(h^L_{i+\frac{1}{2}}\right)^2 + \left(h^R_{i+\frac{1}{2}}\right)^2\right]\right\} = \\ &= \frac{g}{2}\left\{\frac{1}{8}\left(\eta_i - z_{i+\frac{1}{2}} + \eta_{i+1} - z_{i+\frac{1}{2}}\right)^2 + \right. \\ &+ \left.\frac{1}{4}\left[\left(\eta_i - z_{i+\frac{1}{2}}\right)^2 + \left(\eta_i - z_{i+\frac{1}{2}}\right)^2\right]\right\} = \\ &= \frac{g}{2}\left(\eta_i - z_{i+\frac{1}{2}}\right)^2 = \frac{g}{2}\left(h^L_{i+\frac{1}{2}}\right)^2.\end{aligned} \tag{A.30}$$

Similarly, it results:

$$\mathbf{F}''^{\,force}_{i-\frac{1}{2}} = \frac{g}{2}\left(\eta_i - z_{i-\frac{1}{2}}\right)^2 = \frac{g}{2}\left(h^R_{i-\frac{1}{2}}\right)^2. \tag{A.31}$$

According to a centered approximation, the second component of bottom slope source term is:

$$\overline{\mathbf{S}}''_{0\,i} = -g\frac{\left(h^L_{i+\frac{1}{2}} + h^R_{i-\frac{1}{2}}\right)}{2}\frac{\left(z_{i+\frac{1}{2}} - z_{i-\frac{1}{2}}\right)}{\Delta x}, \tag{A.32}$$

and from (A.24) it results:

$$\begin{aligned}uh_i^{n+1} &= -\frac{\Delta t}{\Delta x}\frac{g}{2}\left\{\left[\left(h^L_{i+\frac{1}{2}}\right)^2 - \left(h^R_{i-\frac{1}{2}}\right)^2\right] + \left(h^L_{i+\frac{1}{2}} + h^R_{i-\frac{1}{2}}\right)\left(z_{i+\frac{1}{2}} - z_{i-\frac{1}{2}}\right)\right\} = \\ &= -\frac{\Delta t}{\Delta x}\frac{g}{2}\left(h^L_{i+\frac{1}{2}} + h^R_{i-\frac{1}{2}}\right)\left[\left(h^L_{i+\frac{1}{2}} - h^R_{i-\frac{1}{2}}\right) + \left(z_{i+\frac{1}{2}} - z_{i-\frac{1}{2}}\right)\right] = \\ &= -\frac{\Delta t}{\Delta x}\frac{g}{2}\left(h^L_{i+\frac{1}{2}} + h^R_{i-\frac{1}{2}}\right)(\eta_i - \eta_i) = 0,\end{aligned} \tag{A.33}$$

so the updated specific discharge remains zero.

It is proved that WSDGM satisfies exactly the *C-property*; in particular, if a centered discretization of the bottom slope source term is adopted, the scheme satisfies the exact *Z-property* [82].
The proof for 2D case can be easily derived.

Bibliography

[1] F. Alcrudo and F. Benkhaldoun. Exact solutions to the riemann problem of the shallow water equations with a bottom step. *Computers & Fluids*, 30:643–671, 2001.

[2] ANIDEL. *Le dighe di ritenuta degli impianti idroelettrici italiani.* Milano, 1953. In Italian.

[3] F. Aureli, A. Maranzoni, and P. Mignosa. Two dimensional modeling of rapidly varying flows by finite volume schemes. In *Proceedings of River Flow 2004*, Naples, Italy, 2004.

[4] F. Aureli, A. Maranzoni, P. Mignosa, and C. Ziveri. Flood hazard mapping by means of fully-2d and quasi-2d numerical modeling: a case study. In *Proceedings of the 3rd International Symposium on Flood Defense*, Nijmegen, The Netherlands, 2005.

[5] F. Aureli, A. Maranzoni, P. Mignosa, and C. Ziveri. Fully-2d and quasi-2d modeling of flooding scenarios due to embankment failure. In *Proceedings of River Flow 2006*, Lisbon, Portugal, 2006.

[6] F. Aureli, P. Mignosa, and M. Tomirotti. Numerical simulation and experimental verification of dam-break flows with shocks. *J. Hydr. Res.*, 38:197–206, 2000.

[7] A. Balzano. Evaluation of methods for numerical simulation of wetting and drying in shallow water flow models. *Coastal Eng.*, 34:83–107, 1998.

[8] G.K. Batchelor. *An Introduction to Fluid Dynamics.* Cambridge University Press, 1967.

[9] P.D. Bates and J.M. Hervouet. A new method for moving boundary hydrodynamic problems in shallow water. *Proc. R. Soc. Lond. A*, 455:3107–3128, 1999.

[10] P.D. Bates and M.S. Horritt. Modelling wetting and drying processes in hydraulic models. In S.N. Lane P.D. Bates and R.I. Ferguson, editors, *Computational Fluid Dynamics: Applications in Environmental Hydraulics*, chapter 6, pages 121–146. John Wiley & Sons, 2005.

[11] A. Bayliss and E. Turkel. Radiation-boundary conditions for wave-like equations. *Comm. Pure and Appl. Math.*, 33:708–725, 1980.

[12] L. Begnudelli and B.F. Sanders. Unstructured grid finite-volume algorithm for shallow-water flow and scalar transport with wetting and drying. *ASCE J. Hydr. Eng.*, 132:371–384, 2006.

[13] A. Bermúdez, A. Dervieux, J.A. Desideri, and M.E. Vázquez. Upwind schemes for the two-dimensional shallow water equations with variable depth using unstructured meshes. *Comput. Meth. Appl. Mech. Eng.*, 155:49–72, 1998.

[14] A. Bermúdez and M.E. Vázquez. Upwind methods for hyperbolic conservation laws with source terms. *Comput. Fluids*, 23:1049–1071, 1994.

[15] J.P. Boris and D.L. Book. Flux corrected transport: I.SHASTA, a fluid transport algorithm that works. *J. Comp. Phys.*, 11:38–69, 1973.

[16] S.F. Bradford and B.F. Sanders. Finite-volume model for shallow water flooding of arbitrary topography. *ASCE J. Hydr. Eng.*, 128:289–298, 2002.

[17] P. Brufau, P. García-Navarro, and M.E. Vázquez-Cendón. Zero mass error using unsteady wetting-drying conditions in shallow flows over dry irregular topography. *Int. J. Num. Meth. Fluids*, 45:1047–1082, 2004.

[18] V. Caleffi, A. Valiani, and A. Zanni. Finite volume method for simulating extreme flood events in natural channels. *J. Hydr. Res.*, 41(2):167–177, 2003.

[19] V.T. Chow. *Open Channel Hydraulics*. MacGraw-Hill, Inc., 1959.

[20] D. Citrini and G. Noseda. *Idraulica*. Casa Editrice Ambrosiana, 1975. In Italian.

[21] B. Cockburn and C.W. Shu. TVB Runge Kutta local projection discontinuous Galerkin method for conservation laws II: general framework. *Math. Comp.*, 52:411–435, 1989.

[22] R. Courant, K.O. Friedrichs, and H. Lewy. Uber die partiellen Differenzengleichungen der mathematischen Physik. *Math. Ann.*, 100:32–74, 1928.

[23] R. Courant, K.O. Friedrichs, and H. Lewy. On the partial difference equations of mathematical physics. *IBM J.*, 11:215–234, 1967.

[24] A. Defina. Two dimensional shallow flows equations for partially dry areas. *Water Resour. Res.*, 36:3251–3264, 2000.

[25] P. García-Navarro and M.E. Vázquez. On numerical treatment of the source terms in shallow water equations. *Comput. Fluids*, 29:951–979, 2000.

[26] R. B. Giles. Non reflective boundary conditions for Euler equation calculation. *AIAA J.*, 28:2050–2058, 1990.

[27] S.K. Godunov. A difference scheme for numerical computation of discontinuous solution of hydrodynamic equations. *Math. Sbornik*, 47:271–306, 1959.

[28] M. Greco, M. Iervolino, and A. Leopardi. Discussion on "Divergence Form for Bed Slope Source Term in Shallow Water Equations" by Alessandro Valiani and Lorenzo Begnudelli. *ASCE J. Hydr. Eng.*, in press.

[29] A. Harten. High resolutions schemes for hyperbolic conservation laws. *J. Comp. Phys.*, 49:357–393, 1983.

[30] A. Harten. On a class of high resolution total variation stable finite difference schemes. *J. Numer. Anal.*, 21:1–23, 1984.

[31] A. Harten, P.D. Lax, and B. VanLeer. On upstream differencing and Godunov-type schemes for hyperbolic conservation laws. *SIAM Review*, 25:35–61, 1983.

[32] A. Harten and S. Osher. Uniformly high−order accurate non oscillatory schemes. *SIAM J. Num. Anal.*, 24:279–309, 1987.

[33] J.M. Hervouet and J.M. Janin. Finite element algorithms for modelling flood propagation. In *Proceedings of International Conference on Modelling of Flood Propagation over Initially Dry Areas*, Milan, Italy, 1994. ENEL-DRS-CRIS.

[34] C. Hirsch. *Numerical Computation of Internal and External Flows, Vol.1.* John Wiley & Sons, LTD, 1988.

[35] C. Hirsch. *Numerical Computation of Internal and External Flows, Vol.2.* John Wiley & Sons, LTD, 1988.

[36] T.Y. Hou and P. LeFloche. Why non-conservative schemes converge to the wrong solutions. Error analysis. *Math. of Comp.*, 62(206):497–530, 1994.

[37] M.F. Hubbard and P. García-Navarro. Flux difference splitting and the balancing of source terms and flux gradients. *J. Comp. Phys.*, 165:89–125, 2000.

[38] B. Hunt. An inviscid dam-break solution. *J. Hyd. Res.*, 25:313–327, 1987.

[39] R. Iacono. Analytic solutions to the shallow water equations. *Physical Review E*, 72:017302, 2005.

[40] S. Karni. Accelerated convergence to steady state by gradual far-field damping. *AIAA J.*, 30:1220–1228, 1992.

[41] P.D. Lax. Weak solutions of non linear hyperbolic equations and their numerical computation. *Comm. Pure Appl. Math.*, 7:159–193, 1954.

[42] P.D. Lax and B. Wendroff. Systems of conservation laws. *Comm. Pure Appl. Math.*, 13:217–237, 1960.

[43] R.J. LeVeque. Balancing source terms and flux gradients in high-resolution methods: The quasi-steady wave-propagation algorithms. *J. Comp. Phys.*, 146:346–365, 1998.

[44] R.J. LeVeque. *Finite Volume Methods for Hyperbolic Problems.* Cambridge University Press, 2002.

[45] R. Liska and B. Wendroff. Composite schemes for conservation laws. *SIAM J. Num. Anal.*, 35:2250–2271, 1998.

[46] X.D. Liu, S. Osher, and T. Chan. Weighted essentially non-oscillatory schemes. *J. Comput. Phys.*, 115:200–212, 1994.

[47] R.W. MacCormak and A.J. Paullay. Computational efficiency achieved by time splitting of finite difference operators. *AIAA paper*, 72.

[48] I. MacDonald. *Analysis and computation of steady open channel flow*. PhD thesis, University of Reading, Department of Mathematics, 1996.

[49] I. MacDonald, M.J. Baines, N.K. Nichols, and P.G. Samuels. Analytic benchmark solutions for open-channel flows. *ASCE J. Hydr. Eng.*, 123:1041–1044, 1997.

[50] P.W. McDonald. The computation of transonic flow through two dimensional gas turbine cascades. *ASME paper*, 71.

[51] J.J. Monaghan. Why particle methods work. *SIAM J. Scientific and Statistical Computing*, 3:422–433, 1982.

[52] J. Murillo, P. García-Navarro, J. Burguete, and P. Brufau. A conservative 2d model of inundation flow with solute transport over dry bed. *Int. J. Num. Meth. Fluids*, 52:1059–1092, 2006.

[53] S. Osher. Riemann solvers, the entropy condition and difference approximations. *SIAM J. Numer. Anal.*, 21:217–235, 1984.

[54] S. Osher and S.R. Chakravarty. High resolution schemes and the entropy condition. *SIAM J. Numer. Anal.*, 21:955–984, 1984.

[55] R.D. Richtmeyer and K.W. Morton. *Difference Methods for Initial Value Problems*. John Wiley & Sons, 2nd edition, 1967.

[56] A. Ritter. Die fortplanzung der wasserwellen. *Zeitschrift des Vereines Deutscher Ingenieure*, 36:947–954, 1892.

[57] P.L. Roe. Remote boundary conditions for unsteady multidimensional aerodynamic computations. *Computers & Fluids*, 17:221–231, 1989.

[58] A. Shapiro. Nonlinear shallow-water oscillations in a parabolic channel: exact solutions and trajectory analysis. *J. Fluid Mech.*, 318:49–76, 1996.

[59] C.W. Shu and S. Osher. Efficient implementation of essentially non-oscillatory shock capturing schemes. *J. Comput. Phys.*, 24:439–471, 1988.

[60] S. Soares-Frazão, V. Guinot, J. Lhomme, and Y. Zech. Conservative discretization of bed slope source terms on irregular topographies. In *Proceedings of* 32^{nd} *Congress of IAHR*, Venice, Italy, 2007.

[61] J.J. Stoker. The formation of breakers and bores. *Comm. Pure Appl. Math.*, 1:1–87, 1948.

[62] G. Strang. On the construction and comparison of difference schemes. *SIAM J. Numer. Anal.*, 5:506–517, 2001.

[63] P.K. Sweby. High-resolution schemes using flux limiters for hyperbolic conservation laws. *SIAM J. Numer. Anal.*, 21:995–1011, 1984.

[64] W.C. Thacker. Some exact solutions to the nonlinear shallow-water wave equations. *J. Fluid Mech.*, 107:499–508, 1981.

[65] E.F. Toro. On Glimm-related schemes for conservation laws. Technical report MMU-9602, Department of Mathematic and Physics, Manchester Metropolitan University, 1996.

[66] E.F. Toro. *Riemann Solvers and Numerical Methods for Fluid Dynamics.* Springer, 1999.

[67] E.F. Toro. *Shock-Capturing Methods for Shallow Water Flows.* John Wiley & Sons, LTD, 2001.

[68] E.F. Toro and S.J. Billett. Centred TVD schemes for hyperbolic conservation laws. *IMA J. Numer. Anal.*, 20:47–79, 2000.

[69] E.F. Toro and P. Garcia-Navarro. Godunov-type methods for free-surface flows: a review. *J. Hydr. Res.*, 45:736–751, 2007.

[70] E.F. Toro, R.C. Millington, and L.A.M. Nejad. Towards very high order Godunov schemes. In E.F. Toro, editor, *Godunov Methods: Theory and Applications*, chapter 6, pages 905–937. Kluwer/Plenum Academic Publishers, 2001.

[71] E.F. Toro, M. Spruce, and W. Spears. Restoration of the contact surface in the HLL-Riemann solvers. *Shock Waves*, 4:25–34, 1994.

[72] E.F. Toro and V.A. Titarev. Derivative Riemann solvers for systems of conservation laws and ADER methods. *J. Comput. Phys.*, 212:150–165, 2006.

[73] R. Toro E.F. and A. Chakraborty. Development of an approximate Riemann solver for the steady supersonic Euler equations. *The Aeronautical Journal*, 98:325–339, 1994.

[74] A. Valiani and L. Begnudelli. Divergence form for the bed slope source term in shallow water equations. *ASCE J. Hydr. Eng.*, 146:652–665, 2006.

[75] B. van Leer. MUSCL, a new approach to numerical gas dynamics. In *Computing in plasma physics and astrophysics*, Garchung, Germany, 1976.

[76] G.D. VanAlbada, B. VanLeer, and W.W. Roberts. A comparative study of computational methods in cosmic gas dynamics. *Astronom. Astrophys.*, 108:76–84, 1982.

[77] B. VanLeer. Towards the ultimate conservative difference scheme I. The quest of monotonicity. *Lecture Notes in Physics*, 18:163–168, 1973.

[78] B. VanLeer. Towards the ultimate conservative difference scheme II. Monotonicity and conservation combined in a second order scheme. *J. Comp. Phys.*, 14:361–370, 1974.

[79] B. VanLeer. Towards the ultimate conservative difference scheme V. A second order sequel to Godunov's methods. *J. Comp. Phys.*, 32:101–136, 1979.

[80] B. VanLeer. On the relation between the upwind differencing schemes of Godunov, Enquist-Osher and Roe. *SIAM J. Sci. Stat. Comput.*, 5:1–20, 1985.

[81] M.E. Vázquez. Improved treatment of source terms in upwind schemes for the shallow water equations in channels with irregular geometry. *J. Comp. Phys.*, 32:101–136, 1999.

[82] J.G. Zhou, D.M. Causon, C.G. Mingham, and D.M. Ingram. The surface gradient method for the treatment of source terms in the shallow water equations. *J. Comp. Phys.*, 168:1–25, 2001.